Astronomy Letters, Vol. 26, No. 11, 2000, pp. 691–698. Translated from Pis'ma v Astronomicheskiĭ Zhurnal, Vol. 26, No. 11, 2000, pp. 803–812.

Spectral Variability of the X-ray Pulsar Hercules X-1

A. A. Lutovinov[1]*, S. A. Grebenev[1], M. N. Pavlinsky[1], and R. A. Sunyaev[1, 2]

[1] *Space Research Institute, Russian Academy of Sciences, Profsoyuznaya ul. 84/32, Moscow, 117810 Russia*
[2] *Max-Planck-Institut fuer Astrophysik, Karl-Schwarzschild-Strasse 1, 86740 Garching bei Muenchen, Germany*

Received April 26, 2000

Abstract—We present the results of our comparative timing and spectral analysis of the high and low (off) states in the X-ray pulsar Her X-1 based on data from the ART-P telescope onboard the Granat observatory. A statistically significant (several mCrab) persistent flux with a simple power-law spectrum was detected during the low state. The spectral slope changed from observation to observation by almost a factor of 2. Pulsations were detected only during the high state of the source, when its flux was a factor of ~25 larger than the low-state flux. The spectral shape of Her X-1 in its high state was complex, with the parameters depending on pulse phase. © *2000 MAIK "Nauka/Interperiodica".*

Key words: *pulsars, neutron stars, X-ray sources, scattering*

INTRODUCTION

The X-ray pulsar Her X-1 forms a low-mass binary with the star HZ Her whose parameters are $M_1 = 2.0M_\odot$, $R_1 = 3.9R_\odot$, $a = 8.6R_\odot$, and $i = 80°$, where a is the separation between the binary components, and i is the orbital inclination (Nagase 1989). Today, thirty years after its discovery (Tananbaum *et al.* 1972), it remains one of the most commonly observed X-ray sources. The main reason for this attention is the existence of three periodicities in the binary. Apart from a neutron-star spin period of ~1.24 s and an orbital period of ~1.7 days, observations suggest the existence of a 35-day "on–off" cycle in the binary: the pulsar is in a high-intensity state during ~12 days, while its flux during the remaining ~23 days drops to a level of a few percent of the on-state flux. In the middle between the high states, the X-ray flux rises to ~1/3 of its peak value (the low on state; Jones and Forman 1976) in ~5 days. The 35-day cycle cannot be called periodic in the strict sense of the word. Since the source is assumed by some authors (Tananbaum *et al.* 1972; Crosa and Boynton 1980; Shakura *et al.* 1998) to be turned on near orbital phases 0.2 and 0.7, the turn-on phase "floats" from one 35-day cycle to another. Having analyzed long-term observations of Her X-1, Bochkarev *et al.* (1988) concluded that the turn-on phase of the pulsar is also related to changes in its period. Boynton *et al.* (1980), Staubert *et al.* (1983), and Ögelman (1987) discussed the various statistical models that accounted for the observed variations in the source's turn-on phase.

Despite a wealth of observational data, the nature of the 35-day cycle is not yet completely understood. The most widely discussed models that account for this behavior are as follows: a tilted or warped precessing accretion disk that periodically eclipses the X-ray generation regions on the neutron-star surface (Katz 1973; Boynton *et al.* 1980; Shakura *et al.* 1999) and free neutron-star precession (Lamb *et al.* 1975; Trümper *et al.* 1986). However, based on EXOSAT satellite data, Sheffer (1987) pointed out that such neutron-star precession could not take place in the system Her X-1/HZ Her.

Here, we present the results of our timing and spectral analysis of observational data from the ART-P telescope onboard the Granat Orbiting Observatory at various phases of the orbital (ϕ_{17}) and 35-day (ψ_{35}) cycles of the pulsar Her X-1.

OBSERVATIONS

The observations were performed in 1990–1991 with the ART-P telescope, which is one of the two main instruments onboard the Granat orbiting astrophysical observatory. The telescope consists of four coaxial, completely independent modules; each module includes a position-sensitive detector with a geometric area of 625 cm^2 and a coded mask constructed on the basis of URA sequences. The instrument maps a selected region in the sky within a $3\overset{\circ}{.}4 \times 3\overset{\circ}{.}6$ field of view (FWZR) with a nominal resolution of ~5 arcmin (the angular size of the mask element). Because of the higher spatial resolution (~1.25 arcmin) of the detector, the accuracy of localizing discrete sources is several-fold higher. The telescope is sensitive to photons in the energy range 3–60 keV and has an energy resolution of ~22% in the 5.9 keV iron line [see Sunyaev *et al.* (1990) for a more detailed description of the telescope]. The observations were carried out in the "photon-by-photon"

* E-mail address for contacts: aal@hea.iki.rssi.ru

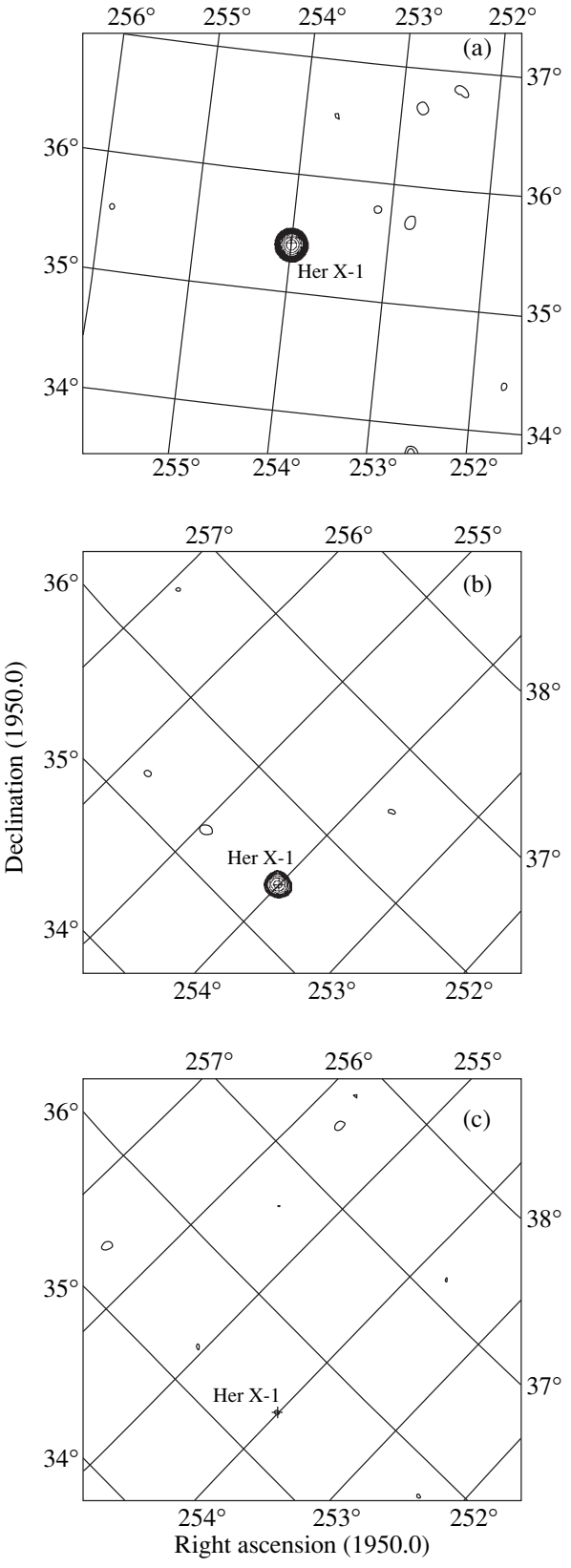

Fig. 1. ART-P 3–20 keV images of the sky region with Her X-1 during its (a) high, (b) low, and (c) eclipse states. The 3, 4, 5, or more σ confidence regions of the source are indicated by contours.

mode, in which, for each photon, its coordinates on the detector, energy (1024 channels), and arrival time were written into buffer memory. This mode allows both timing and spectral analyses of the emission from each X-ray source within the ART-P field of view. The photon arrival time is accurate to within 3.9 ms (1/256 of the onboard second), and the ART-P dead time is 580 μs. The spacecraft is stabilized to within ±30 arcmic. Its wobbling within this range results in the flux from the source being modulated with a characteristic time of 900–1100 s with the collimator transmission function. When constructing the light curves, phase curves, and spectra of the pulsar Her X-1, we applied corrections for this effect.

Of the four individual observing sessions during which the pulsar Her X-1 fell within the ART-P field of view (on March 3 and 6, July 21, 1990, and on August 22, 1991), the source was detected in the high state only on March 6, 1990; the remaining three sessions corresponded to different phases of the low state. The observations on July 21, 1990, partly coincided in time with an X-ray eclipse at $\phi_{17} \simeq 0.93$–0.07 (Bochkarev *et al.* 1988). It should be noted that, since the energy resolution of the ART-P module used for the observations on August 22, 1991, was considerably lower, the data obtained on this day were used only for imaging and for a timing analysis.

As was already pointed out above, there is a spread in the source's turn-on times and, accordingly, in the phase of the 35-day cycle determined by different authors. Here, we used the dependence from Soong *et al.* (1987).

RESULTS

Table 1 gives the dates and durations of our observations, the mean 3–20 keV photon fluxes measured during the sessions, and the corresponding phases of the orbital period and the 35-day cycle (the mean fluxes from the source in its pre-eclipse and eclipse states are given separately for the session of July 21, 1990). Figure 1 shows the $3\overset{\circ}{.}0 \times 3\overset{\circ}{.}0$ X-ray sky maps with Her X-1 obtained during two different observing sessions. The image in Fig. 1a was obtained on March 6, 1990, when the source was in its high state; Figs. 1b and 1c present the sky maps on July 21, 1990, during the pre-eclipse low and eclipse states. As discussed below, no X-ray pulsations are observed during the low state. The maps indicate that the detected emission does come precisely from the pulsar Her X-1 rather than from any accidental faint source within the field of view. The X-ray flux variations attributable to eclipse ingress of the source during this session are shown in Fig. 2 (the background count rate was subtracted). The eclipse onset time is in good agreement with that suggested by the binary's known orbital parameters (Deeter *et al.* 1991).

TIMING ANALYSIS

X-ray pulsations were detected by the ART-P telescope only on March 6, 1990, when Her X-1 was in its high state. The period determined by the epoch-folding technique after the photon arrival times were corrected for the motion of the neutron star in the binary and for the Earth's and spacecraft motion was 1.23775454 ± 0.00000048 s (Lutovinov *et al.* 1994); the pulse fraction in the 3–30 keV energy band, defined as $P = (I_{max} - I_{min})/(I_{max} + I_{min})$, where I_{max} and I_{min} are the count rates at maximum and minimum of the pulse profile, was ≃65.5%. Note that, in the 3–18 keV energy band, P was essentially constant at a 67–68% level, and only at higher energies did it decrease to ~58%. The upper limits on the low-state pulse fraction during the March 3 and July 21 sessions were 2.9 and 18% (3σ), respectively.

Figure 3 shows the pulsar phase light curves in four energy bands (3–6, 6–12, 12–18, and 18–30 keV) averaged over this entire observing session. The ratio of the instantaneous flux to the flux averaged over the pulsation period is plotted along the vertical axis. The constructed pulse profile of Her X-1 has a shape typical of the on state: a relatively broad (~0.5 of the period) double-peaked pulse with a clear dominance of the first peak and a sharp drop in intensity to a minimum after the second peak. An analysis of the energy dependence of the pulse profile indicates that the amplitude of the second peak decreases with increasing energy, and it virtually disappears in the hardest energy band. The first peak becomes considerably narrower, the position of the minimum remains unchanged, and the intensity maximum displaces rightward by ~0.1 into the phase range 0.70–0.75. This behavior of the phase curves is shown more clearly in the lower panel of Fig. 3, which presents the phase dependence of the pulsar hardness (the ratio of the pulse profiles in the 18–30 and 6–12 keV energy bands).

THE SPECTRA IN DIFFERENT STATES

When X-ray pulsars are investigated, the main spectral model is a simple power law with a high-energy cutoff (White *et al.* 1983). Depending on a specific object, this model is generally modified by absorption in the soft energy band and by emission lines. The spectra of some pulsars exhibit cyclotron absorption lines (Trümper *et al.* 1978; Mihara *et al.* 1995). Since the cyclotron line in Her X-1 lies outside the ART-P operating range, the model that we used in our spectral analysis appears as follows:

$$I(E) = I_{10}\left(\frac{E}{10\ \mathrm{keV}}\right)^{-\alpha}\exp(-\sigma_A N_H) \times \begin{cases} 1, & \text{if } E < E_c \\ \exp[-(E-E_c)/E_f], & \text{if } E \geq E_c, \end{cases} \quad (1)$$

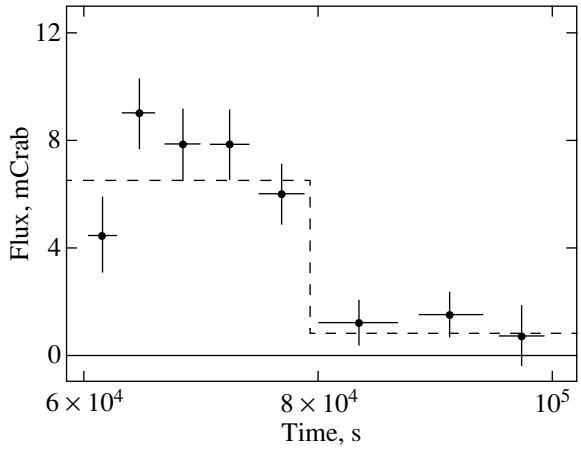

Fig. 2. The pulsar light curve including an eclipse during the observations on July 21, 1990. The presumed eclipse onset time is indicated by dashes.

where E is the photon energy in keV, I_{10} is the normalization of the power-law component at 10 keV, α is the photon spectral index, N_H is the hydrogen column density, $\sigma_A(E)$ is the interstellar absorption cross section (Morrisson and McCammon 1983), E_c is the cutoff energy, and E_f is the e-folding energy of an exponential cutoff in the source's spectrum.

A preliminary analysis (Lutovinov *et al.* 1997) shows that the pulsar high-state spectrum is well described by model 1, with the interstellar absorption column density being $N_H \leq 4.5 \times 10^{21}$ cm^{-2}. A more detailed investigation reveals an additional emission feature at energy ~7.6 keV. In order to take this feature into account, we modified model 1 by adding a Gaussian with a central energy E_K and a total flux A_K (model 2). Since the line was assumed to be narrow, its width was fixed at 0.1 keV, which is below the ART-P spectral resolution. Best-fit parameters for the spectrum are given in Table 2 (all errors correspond to 1σ). The line equivalent width is $W \simeq 280$ eV. In order to test how significant the decrease in χ^2 was when passing from model 1 to model 2 (see Table 2), we estimated the probability that this decrease in χ^2 occurred by chance. Our probability calculations based on $\Delta\chi^2$ statistics yielded 3.4×10^{-5}, which is 4.2σ in standard deviations of the normal distribution. Figure 4a shows the pulsar high-state spectrum.

Table 1. ART-P observations of the pulsar Her X-1

Date	Duration, s	Flux, mCrab*	ϕ_{17}	ψ_{35}
March 3, 1990	14620	6.3 ± 0.4	0.41–0.55	0.98
March 6, 1990	10920	150.4 ± 1.0	0.20–0.29	0.07
July 21, 1990	15250	6.5 ± 0.6	0.80–0.93	0.99
	15760	0.8 ± 0.5	0.93–0.07	0.00
August 22, 1991	23000	10.9 ± 1.8	0.30–0.51	0.38

* In the 3–20 keV energy band.

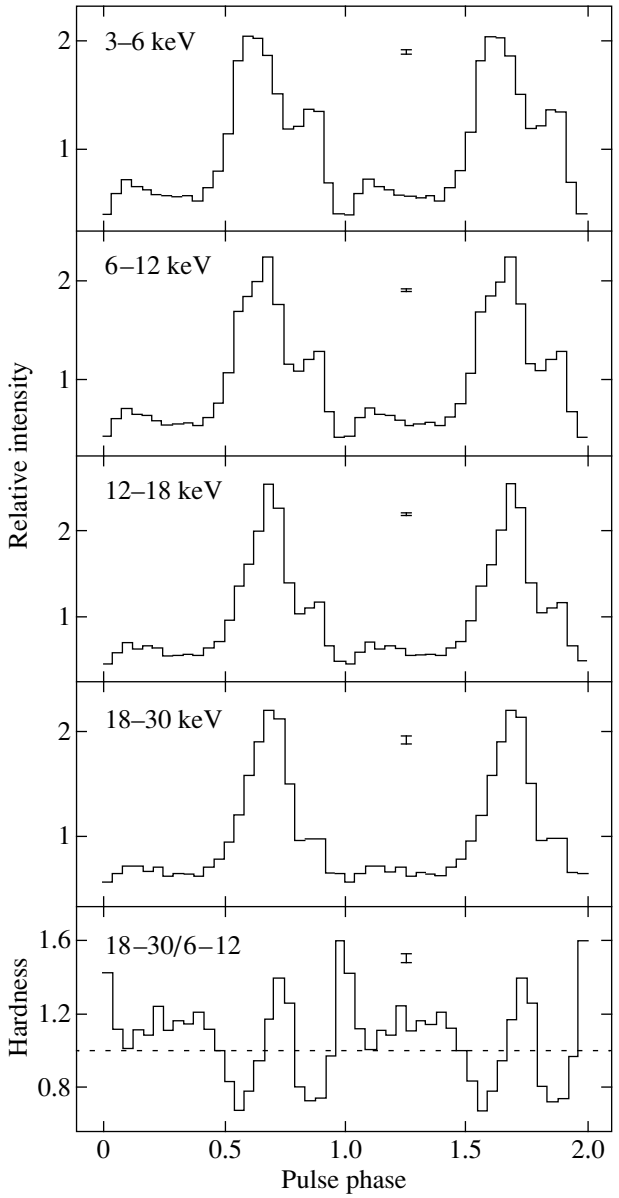

Fig. 3. The pulse profiles of the pulsar Her X-1 in various energy bands on March 6, 1990, during its high state. The ratio of the instantaneous photon flux to the period-averaged flux is along the vertical axis. The evolution of the source's hardness during one period is shown in the lower panel. The errors correspond to one standard deviation.

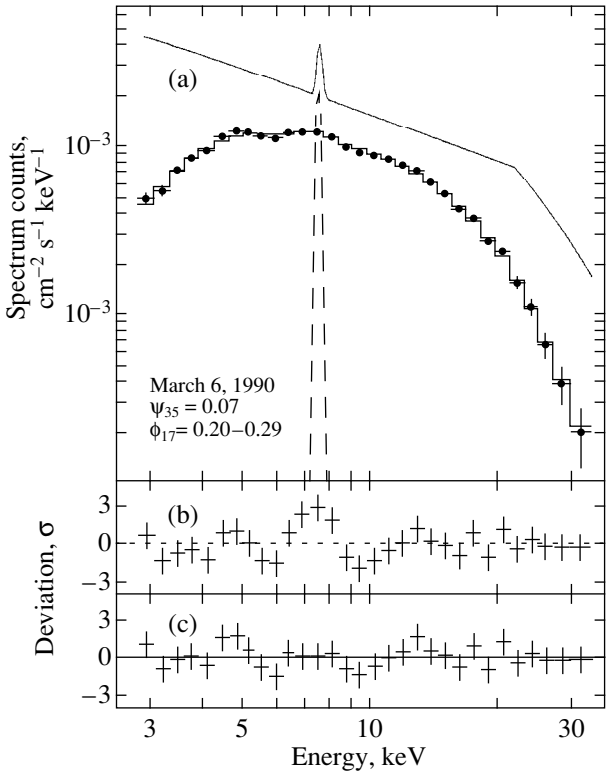

Fig. 4. (a) The high-state spectrum of the pulsar Her X-1 as constructed from the ART-P data obtained on March 6, 1990. The measured (pulse-height) spectrum is indicated by dots, and the histogram represents its best fit by model 2 (see Table 2). The model (photon) spectrum is represented by the solid line. The dashed line indicates the contribution of the emission line at 7.6 keV. Panels (b) and (c) show deviations of the experimental data (in σ) from the best fits by models 1 and 2, respectively. The errors correspond to one standard deviation.

The pulse-height spectrum (in counts s^{-1} cm^{-2} keV^{-1}) is indicated by dots, and the solid line represents the corresponding model photon spectrum (in phot. s^{-1} cm^{-2} keV^{-1}) with the feature at ~7.6 keV, whose contribution is indicated separately by the dashed line. Deviations (in σ) of the measured spectrum from the model spectra convolved with the instrumental response matrix are shown in Figs. 4b (without the feature) and 4c (with the feature).

According to ART-P data, the low state of the pulsar Her X-1 is characterized by an X-ray flux of several percent of its high-state flux and by the absence of X-ray pulsations. The source's spectra measured on March 3 and July 21, 1990, are shown in Figs. 5a and 5b, respectively. As in Fig. 4, the pulse-height spectra and the corresponding model spectra are represented by dots and solid lines, respectively. A visual difference between the pulse-height spectra is attributable to a difference between the response matrices for the ART-P modules used during these observations. Both spectra are well described by a simple power law without evidence of a cutoff in the hard energy band or of emission lines. Best-fit spectral parameters are given in Table 3. We see that the spectral slopes differ by a factor of ~2, with the photon flux at 10 keV (and the total 3–20 keV flux; see Table 1) being virtually the same.

Her X-1 is observed in its low state if the compact source is hidden behind the outer edge of a warped (or tilted to the orbital plane) accretion disk. The emission greatly attenuated by absorption and scattering in cold matter on the disk periphery or the emission scattered in a hot corona above the disk reaches us. A number of observational facts (Bochkarev 1989) point to the existence of such a corona in the binary. To a first approxi-

mation, the spectrum observed in this state must differ from the initial one merely by a normalization (because of scattering) and a stronger low-energy cutoff (because of photoabsorption). Using the source's high-state spectrum as the original one in this model, we attempted to fit the spectra measured during its low state. The results in Table 3 (model 3) suggest that the described pattern is completely confirmed by the March 3 observations, but is in conflict (an appreciable increase in χ^2_N and no evidence of absorption) with the July 21, 1990 observations. The source's spectrum proper most likely changed appreciably in the five months elapsed between the observations. To some extent, this conflict can be associated with an increase in the fraction of the photons scattered in the hot corona compared to those which arrived from the disk edge. Unfortunately, the quality of the spectra measured during the source's low state does not allow this question to be answered unequivocally.

PHASE-RESOLVED SPECTROSCOPY

The energy dependence of the pulsar pulse profile is directly related to the evolution of its spectrum on a scale of one pulsation period. In order to investigate this relationship, we performed phase-resolved spectroscopy of the source in the on state. The data of the March 6 session were folded with the pulsar period and divided into eight bins (this number, which is a factor of 3 smaller than that used to construct the pulse profile in Fig. 3, was chosen to improve the statistics). The arrival time of each photon was corrected for the Doppler effect caused by motion of the satellite and the Earth around the Sun and by motion of the neutron star in the binary. The total integration time for each of the eight bins corrected for the dead time of the instrument was ~1060 s. An analysis indicates that, in general, all our spectra are satisfactorily described by a simple power law in the 3–20 keV energy band, although the photon index varies greatly (by more than a factor of 2) on a scale of one pulsation period (Fig. 6b). For clarity, Fig. 6a shows the source's pulse profile in the 3–20 keV energy band. The pulsar spectrum near the maximum of the main peak is seen to become considerably harder than the measured spectrum at other phases. We obtained a similar result when analyzing the source's pulse profile (see the lower panel in Fig. 3). Such a dependence was previously noted by Pravdo *et al.* (1977b) when analyzing OSO-8 satellite data.

A more detailed study of the phase-resolved spectra indicates that many of them exhibit features which cannot be described by a power law. Figure 7 shows deviations of the measured spectra (in σ) from the best power-law fit. In the subsequent analysis, we used models representing various combinations of the components of models 1 and 2. As in our analysis of the pulsar phase-averaged spectrum, we compared the fits by these models with simple power-law fits using the $\Delta\chi^2$ test. A model was considered acceptable if the probability that the improvement in χ^2 for a more complex model did not occur by chance exceeded 95%. Best-fit parameters for the phase-resolved spectra are listed in Table 4. For comparison, power-law fits to the spectra are also given in this table. A comparison of the phase-resolved spectra indicates that the line at ~7.6 keV in the integrated spectrum appears to result from a superposition of hydrogen- and helium-like iron emission features at energies 6.7–6.9 keV in some spectra and of absorption features beyond the *K* edge of strongly ionized iron at 8.6–9.3 keV in other spectra.

Noteworthy is the detection of substantial absorption in spectra IV and V corresponding to the pulse rise,

Table 2. Best-fit parameters for the high-state spectrum of Her X-1 as inferred from the observations on March 6, 1990

Parameter	Model 1	Model 2
I_{10} [a]	1.572 ± 0.015	1.540 ± 0.017
α	0.945 ± 0.020	0.918 ± 0.021
N_H, 10^{22} cm^{-2}	0.45	0.45
E_c, keV	21.7 ± 1.3	21.9 ± 1.3
E_f, keV	11.0 ± 3.2	10.2 ± 3.0
E_K, keV	…	7.58 ± 0.19
A_K [b]	…	5.5 ± 1.6
$\chi^2_N(N)$ [c]	1.49(29)	0.84(27)

[a] The flux at 10 keV (10^{-2} phot. cm^{-2} s^{-1} keV^{-1}).
[b] The total line flux (10^{-3} phot. cm^{-2} s^{-1}).
[c] The χ^2 value normalized to the number of degrees of freedom *N*.

Table 3. Best-fit parameters for the low-state spectrum of Her X-1

Date	Parameter	Model 1	Model 3
March 3, 1990	I_{10} [a]	6.23 ± 0.43	7.94 ± 0.9
	α	0.72 ± 0.15	0.945
	E_c, keV	…	21.7
	E_f, keV	…	11.0
	N_H, 10^{22} cm^{-2}	0.45	10.9 ± 6.6
	$\chi^2_N(N)$ [b]	0.59(11)	0.50(11)
July 21, 1990	I_{10} [a]	6.12 ± 0.57	6.45 ± 0.61
	α	1.30 ± 0.21	0.945
	E_c, keV	…	21.7
	E_f, keV	…	11.0
	N_H, 10^{22} cm^{-2}	0.45	≤ 20(3σ)
	$\chi^2_N(N)$ [b]	0.66(13)	0.87(13)

[a] The flux at 10 keV (10^{-4} phot. cm^{-2} s^{-1} keV^{-1}) without absorption.
[b] The χ^2 value normalized to the number *N* of degrees of freedom.

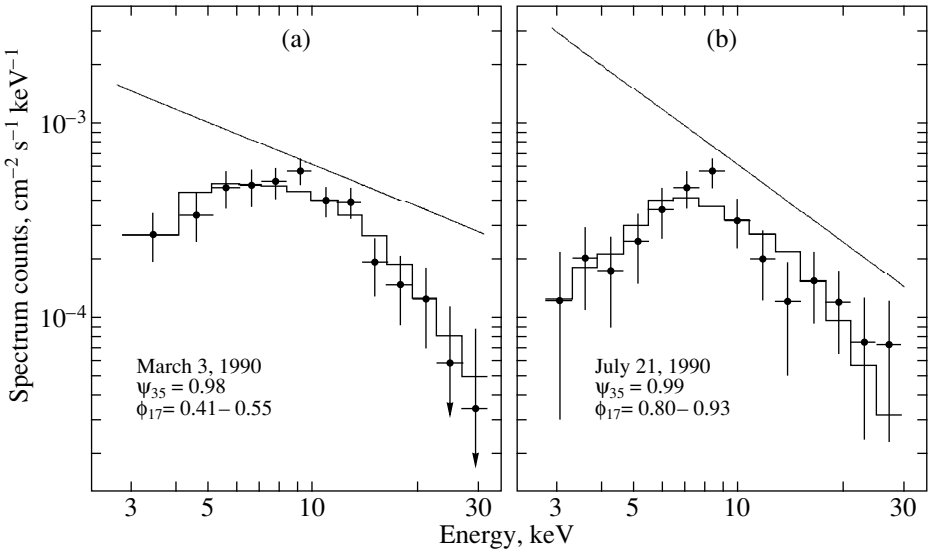

Fig. 5. The low-state spectra of Her X-1 on (a) March 3 and (b) July 21, 1990 (outside eclipse). The histograms indicate the best power-law fits, and the solid lines represent the model (photon) spectra. The errors correspond to one standard deviation.

suggesting the possible presence of fairly cold matter on the line of sight at this time. The absorption has virtually no effect on the shape of the source's average spectrum, most likely because the spectra measured near the maximum of the pulse profile (VI and VII) mainly contribute to it.

DISCUSSION

Bochkarev (1989) proposed a model of a hot ($T_c \simeq 2.5 \times 10^6$ K) corona above the outer ($R_d \gtrsim 1.7 \times 10^{11}$ cm) parts of the accretion disk to explain the flickering in Her X-1 during X-ray dips. The gas density in the corona is n $n_e \simeq (5–7) \times 10^{11}$ cm^{-3}, and its height above the disk plane is $H \gtrsim 10^{11}$ cm. The scattering of emission from the compact source by coronal electrons can account for the existence of an X-ray flux in the low state. Indeed, the corona optical depth for Thomson scattering along the disk is $\tau_T = 2H\sigma_T n_e \simeq 0.1$; thus, the scattered flux must be $F_s \simeq \tau_T F_0 \Omega / 4\pi \simeq 0.02 F_0$, where F_0 is the flux from the compact source, and $\Omega \simeq 4\pi(1 - \mu) \sim 2\pi(H/R)^2$ is the solid angle at which the corona is seen. In general, the ART-P data are consistent with this pattern, although they suggest a stronger X-ray emission in the low state (with an intensity that is a factor of ~25 lower than that during the high state). The photons multiply scattered in the cold and fairly dense matter at the accretion-disk edge and, hence, having a spectrum

Table 4. Best-fit parameters for the phase-resolved spectra of the pulsar Her X-1

Phase	Model[a]	I_{10}, 10^{-3} [b]	α	E_c, keV	E_f, keV	N_H, 10^{22}	A_K, 10^{-2}	E_K, keV	$\chi^2_N(N)$
I	PL	8.51 ± 0.27	1.002 ± 0.069						1.22(24)
	PL + HEC	11.55 ± 2.61	0.430 ± 0.380	7.8 ± 3.3	15.4 ± 6.5				0.81(22)
II	PL	8.84 ± 0.27	0.957 ± 0.067						1.72(24)
III	PL	8.20 ± 0.27	1.121 ± 0.070						1.35(24)
IV	PL	9.82 ± 0.26	1.038 ± 0.063						2.05(23)
	PL + ABS	11.53 ± 0.88	1.343 ± 0.151			10 ± 5			1.89(22)
V	PL	22.99 ± 0.37	1.131 ± 0.035						1.59(24)
	PL + ABS + GAU	23.94 ± 1.22	1.222 ± 0.090			4.3 ± 2.7	1.15 ± 0.48	7.37 ± 0.33	1.15(21)
VI	PL	28.27 ± 0.42	0.830 ± 0.031						2.68(25)
	PL + HEC	31.68 ± 0.61	0.670 ± 0.039	22.1 ± 1.9	8.1 ± 4.6				1.20(23)
VII	PL	16.75 ± 0.33	1.048 ± 0.044						1.65(24)
VIII	PL	10.35 ± 0.27	1.154 ± 0.060						1.01(24)

[a] PL for a power-law spectrum, HEC for a high-energy cutoff, ABS for absorption in the soft energy band, and GAU for a line with a Gaussian profile.

[b] I_{10} is the measured flux at 10 keV (in phot. cm^{-2} s^{-1} keV^{-1}).

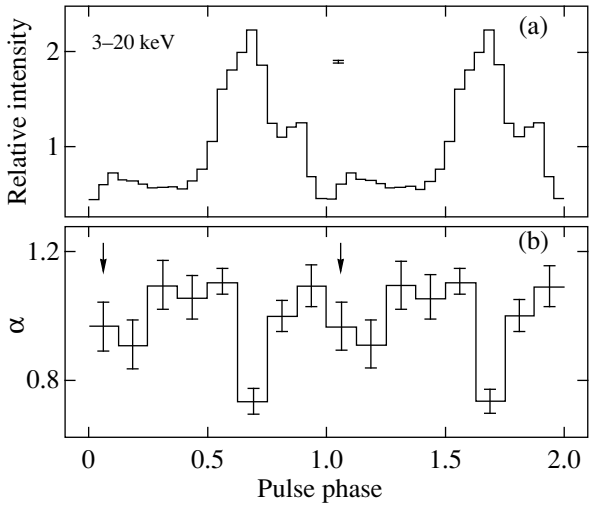

Fig. 6. (a) The pulsar integrated 3–20 keV pulse profile obtained during the observations on March 6, 1990. The ratio of the instantaneous photon flux to the period-averaged flux is along the vertical axis. The photon index measured in this energy band is plotted against phase in panel (b). The arrows mark the first (I) bin used for phase-resolved spectroscopy. The errors correspond to one standard deviation.

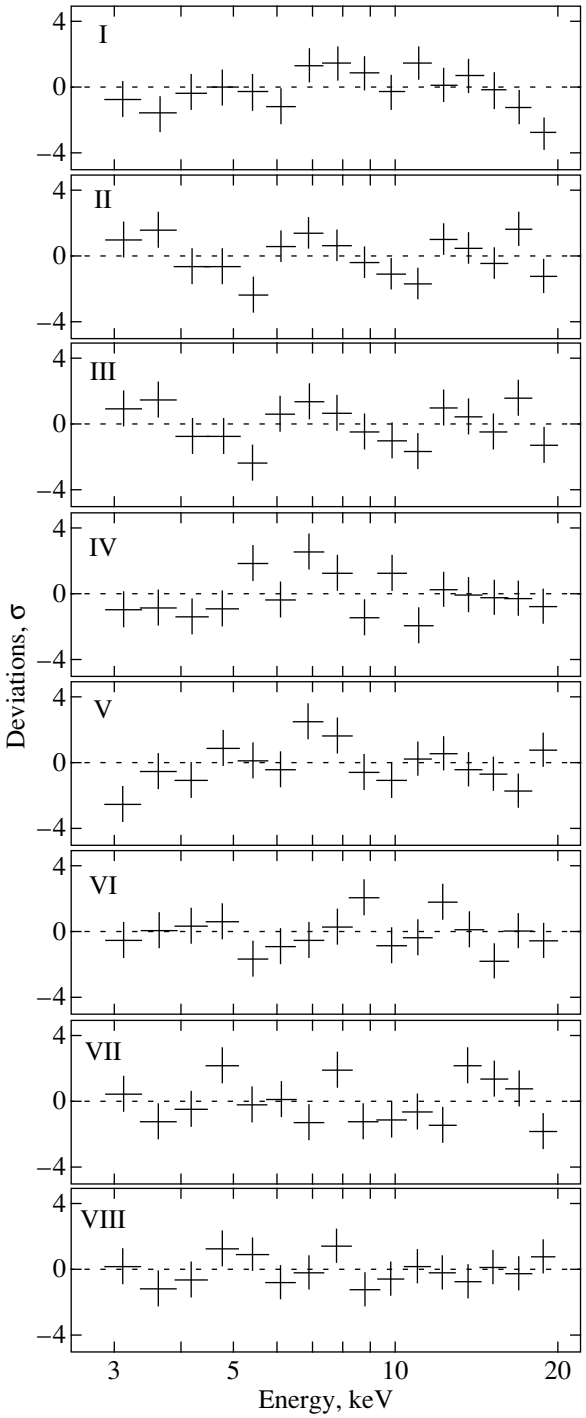

Fig. 7. The deviations of the experimental data (in σ) measured for the phase-resolved spectra of Her X-1 from their best power-law fit in the 3–20 keV energy band.

severely distorted by photoabsorption (compared to the spectrum of the photons scattered in the hot corona) may contribute to this emission. In this case, the optical depth for scattering and absorption must be large to account for the observed dramatic decline in flux. On the other hand, the estimated low scattered photon flux may be associated with uncertainty in the estimated parameters of the corona.

Curiously enough, a positive flux was detected during the ART-P observations of an X-ray eclipse of Her X-1, though at a low confidence level. A similar result was previously obtained during EXOSAT and GINGA observations of this source (Parmar *et al.* 1985; Choi *et al.* 1994). The X-ray flux during the eclipse dropped at least by a factor of ~6 relative to the low-state flux. This implies that the scattering region (corona) is not completely obscured by the optical star, and its sizes must be comparable to the star sizes, $R_1 \simeq 3.9R_\odot \simeq 2.7 \times 10^{11}$ cm; i.e., they must exceed the assumed disk size R_d and the corona height H. On the other hand, having estimated the duration of the source's eclipse ingress from Fig. 2, $\Delta t \lesssim 4000$ s, and knowing the relative orbital velocity of the neutron and normal stars, $K \simeq 300$ km s^{-1}, we obtain $R \sim \Delta t K \simeq 1.2 \times 10^{11}$ cm for the size of the emitting region, in agreement with our estimates of R_d and H.

During scattering in the corona, any information about variability on a time scale shorter than $H/c \sim 3$ s, where c is the speed of light, must be obscured. This allows the absence of pulsations in the source's low state to be explained. Such an effect also takes place during scattering at the disk edge; since the photons scattered in geometrically distant parts of the disk edge are observed in this case, the delay in the photon arrival of the same pulse can reach $R_d/c \sim 6$ s.

The emission line at ~7.6 keV detected by ART-P in the pulsar spectrum appears to result from a superposition of emission and absorption features observed at energies 6.4–9.3 keV in individual phase-resolved

spectra. Pravdo *et al.* (1977a), who detected emission features in the spectrum of Her X-1 at energies ~5.5 and ~7.3 keV using the OSO-8 satellite, suggested Doppler shifts of the 6.4-keV fluorescence iron line as a possible explanation of their origin. The unshifted 6.4-keV line was observed from this source during many experiments. The plasma flowing over the neutron-star magnetosphere may be responsible for the emission in this line. In the case of ART-P, the emitting plasma must have a high velocity, $v \sim 0.15$ c, to produce an observable shift of the line center. The radius corresponding to such a rotation velocity is R $R_K = v(P/2\pi) \simeq 8.6 \times 10^8$ cm, which is comparable to the size of the Alfven surface $R_A \simeq (2–7) \times 10^8$ cm (McCray and Lamb 1976; Pravdo *et al.* 1977a). Using R_K and taking the pulsar luminosity to be $\simeq 1.3 \times 10^{37}$ erg s^{-1}, in accordance with its observations in the high state and assuming the distance to be d = 5 kpc, we estimate the surface magnetic-field strength of the star to be $B \sim 1.3 \times 10^{13}$ G. This slightly exceeds the values obtained from observations of cyclotron lines in the pulsar spectrum, $B \simeq (3.5–5.3) \times 10^{12}$ G (Trümper *et al.* 1978; Dal Fiume *et al.* 1998).

The model described above was proposed by McCray and Lamb (1976) to account for the soft X-ray emission from Her X-1. The envelope thickness proves to be at a maximum on the magnetic equator, gradually decreasing toward higher latitudes and again becoming large at the magnetic poles. By varying the ratios of the angles between the star's rotation axis, the magnetic-dipole axis, and the observer's direction, we can choose a law of variation in the optical depth of the matter through which the X-ray emission from hot spots at the neutron-star poles passes that allows the observed shape of the pulse profile to be described. The detected variation in the source's hardness can also be naturally explained in terms of this model (Pravdo *et al.* 1977b).

ACKNOWLEDGMENTS

This study was supported by the Russian Foundation for Basic Research (projects nos. 98-02-17 056, 99-02-18178, and 00-15-99297). We wish to thank K.G. Sukhanov, flight director, the staffs of the Lavochkin Research and Production Center, RNIIKP, and the Deep Space Communications Center in Evpatoria, the Evpatoria team of the Space Research Institute (Russian Academy of Sciences), the team of I.D. Tserenin, and B.S. Novikov, S.V. Blagii, A.N. Bogomolov, V.I. Evgenov, N.G. Khavenson, and A.V. D'yachkov from the Space Research Institute who operated the Granat observatory, provided the scientific planning of the mission, and performed a preliminary processing of telemetry data. We also wish to thank the team of M.N. Pavlinsky (Space Research Institute) and the staff of the former Research and Development Center of the Space Research Institute in Bishkek who designed and manufactured the ART-P telescope.

REFERENCES

1. N. G. Bochkarev, Astron. Zh. **66**, 1239 (1989) [Sov. Astron. **33**, 638 (1989)].
2. N. G. Bochkarev, V. M. Lyuty, E. K. Sheffer, and I. B. Voloshina, Pis'ma Astron. Zh. **14**, 992 (1988) [Sov. Astron. Lett. **14**, 421 (1988)].
3. P. E. Boynton, L. M. Crosa, and J. E. Deeter, Astrophys. J. **237**, 169 (1980).
4. C. S. Choi, T. Dotani, F. Nagase, *et al.*, Astrophys. J. **427**, 400 (1994).
5. L. Crosa and P. Boynton, Astrophys. J. **235**, 999 (1980).
6. D. Dal Fiume, M. Orlandini, G. Cusumano, *et al.*, Astron. Astrophys. **329**, L41 (1998).
7. J. E. Deeter, P. E. Boynton, S. Miyamoto, *et al.*, Astrophys. J. **383**, 324 (1991).
8. C. Jones and W. Forman, Astrophys. J. Lett. **209**, L131 (1976).
9. J. I. Katz, Nature (London), Phys. Sci. **246**, 87 (1973).
10. D. Q. Lamb, F. K. Lamb, D. Pines, *et al.*, Astrophys. J. Lett. **198**, L21 (1975).
11. A. A. Lutovinov, S. A. Grebenev, R. A. Sunyaev, and M. N. Pavlinsky, Pis'ma Astron. Zh. **20**, 631 (1994) [Astron. Lett. **20**, 538 (1994)].
12. A. Lutovinov, S. Grebenev, and R. Sunyaev, in *The Transparent Universe*, Ed. by C. Winkler *et al.* (ESA, 1997), SP-382, p. 295.
13. R. McCray and F. Lamb, Astrophys. J. Lett. **204**, L115 (1976).
14. T. Mihara, PhD Thesis (RIKEN, 1995).
15. R. Morrisson and D. McCammon, Astrophys. J. **270**, 119 (1983).
16. F. Nagase, Publ. Astron. Soc. Jpn. **41**, 1 (1989).
17. H. Ögelman, Astron. Astrophys. **172**, 79 (1987).
18. A. N. Parmar, W. Pietsch, S. McKechnie, *et al.*, Nature **313**, 119 (1985).
19. S. Pravdo, R. Becker, E. Boldt, *et al.*, Astrophys. J. Lett. **215**, L61 (1977a).
20. S. Pravdo, E. Boldt, S. Holt, *et al.*, Astrophys. J. Lett. **216**, L23 (1977b).
21. N. I. Shakura, N. A. Ketsaris, M. E. Prokhorov, and K. A. Postnov, Mon. Not. R. Astron. Soc. **300**, 992 (1998).
22. N. I. Shakura, M. E. Prokhorov, K. A. Postnov, and N. A. Ketsaris, Astron. Astrophys. **348**, 917 (1999).
23. E. K. Sheffer, Pis'ma Astron. Zh. **13**, 204 (1987) [Sov. Astron. Lett. **13**, 82 (1987)].
24. Y. Soong, D. E. Gruber, and R. E. Rothschild, Astrophys. J. Lett. **319**, L77 (1987).
25. R. Staubert, M. Bezler, and E. Kendziorra, Astron. Astrophys. **117**, 215 (1983).
26. R. A. Sunyaev, S. I. Babichenko, D. A. Goganov, *et al.*, Adv. Space Res. **10** (2), 233 (1990).
27. H. Tananbaum, H. Gursky, E. Kellog, *et al.*, Astrophys. J. Lett. **174**, L143 (1972).
28. J. Trümper, W. Pietsch, *et al.*, Astrophys. J. Lett. **219**, L105 (1978).
29. J. Trümper, P. Kahabka, H. Ögelman, *et al.*, Astrophys. J. Lett. **300**, L63 (1986).
30. N. White, J. Swank, and S. Holt, Astrophys. J. **270**, 771 (1983).

Translated by V. Astakhov

Astronomy Letters, Vol. 26, No. 11, 2000, pp. 699–724. Translated from Pis'ma v Astronomicheskiĭ Zhurnal, Vol. 26, No. 11, 2000, pp. 813–841.

Energy Release During Disk Accretion onto a Rapidly Rotating Neutron Star

N. R. Sibgatullin[1, 2]* and R. A. Sunyaev[2, 3]

[1] *Moscow State University, Vorob'evy gory, Moscow, 119899 Russia*
[2] *Max-Planck-Institut fuer Astrophysik, Karl-Schwarzschild-Strasse 1, 86740 Garching bei Muenchen, Germany*
[3] *Space Research Institute, Russian Academy of Sciences, Profsoyuznaya ul. 84/32, Moscow, 117810 Russia*

Received February 28, 2000

Abstract—The energy release L_s on the surface of a neutron star (NS) with a weak magnetic field and the energy release L_d in the surrounding accretion disk depend on two independent parameters that determine its state (for example, mass M and cyclic rotation frequency f) and is proportional to the accretion rate. We derive simple approximation formulas illustrating the dependence of the efficiency of energy release in an extended disk and in a boundary layer near the NS surface on the frequency and sense of rotation for various NS equations of state. Such formulas are obtained for the quadrupole moment of a NS, for a gap between its surface and a marginally stable orbit, for the rotation frequency in an equatorial Keplerian orbit and in the marginally stable circular orbit, and for the rate of NS spinup via disk accretion. In the case of NS and disk counterrotation, the energy release during accretion can reach $0.67\dot{M}c^2$. The sense of NS rotation is a factor that strongly affects the observed ratio of nuclear energy release during bursts to gravitational energy release between bursts in X-ray bursters. The possible existence of binary systems with NS and disk counterrotation in the Galaxy is discussed. Based on the static criterion for stability, we present a method of constructing the dependence of gravitational mass M on Kerr rotation parameter j and on total baryon mass (rest mass) m for a rigidly rotating neutron star. We show that all global NS characteristics can be expressed in terms of the function $M(j, m)$ and its derivatives. We determine parameters of the equatorial circular orbit and the marginally stable orbit by using $M(j, m)$ and an exact solution of the Einstein equations in a vacuum, which includes the following three parameters: gravitational mass M, angular momentum J, and quadrupole moment Φ_2. Depending on Φ_2, this solution can also be interpreted as a solution that describes the field of either two Kerr black holes or two Kerr disks.

Key words: *neutron stars, luminosity, disk accretion, X-ray bursters*

INTRODUCTION

Observational Facts. Three independent observational facts have prompted us to revert to the problem of disk accretion onto neutron stars (NSs) with weak magnetic fields, which have virtually no effect on the accretion dynamics.

(1) The discovery of an accreting X-ray pulsar/burster with rotation period $p = 2.5$ ms (cyclic frequency $f = 1/p = \Omega/2\pi = 401$ Hz) in a binary system with an orbital period of 2 h, SAX J1808.4–3658 (Van der Klis *et al.* 2000; Chakrabarty and Morgan 1998; Gilfanov *et al.* 1998).

(2) The detection of quasi-periodic oscillations in X-ray bursters during X-ray bursts with frequencies of ~300–600 Hz from the RXTE satellite (Stromayer *et al.* 1998; Van der Klis *et al.* 2000). In the pattern of slow (in seconds!) motion of the nuclear helium burning front over the stellar surface, these flux oscillations can be naturally interpreted as evidence of rapid NS rotation with the oscillation frequency of the X-ray flux. The rotation frequencies of the X-ray bursters KS 1731–260, Aql X-1, and 4U 1636–53 are 523.9, 548.9, and 581.8 Hz, respectively (Van der Klis *et al.* 2000). The rotation periods of these neutron stars are close to 1.607 ms, the rotation period of the millisecond radio pulsar B1957+20, the shortest one among those found to date (Thorsett and Chacrabarty 1998). Recall that B1957+20 is a member of a binary system with a 0.362-day period.

(3) The discovery of twenty millisecond radio pulsars in the globular cluster 47 Tuc. Most of these pulsars have periods from 2 to 8 ms and are members of close low-mass binaries. The total number of millisecond pulsars in 47 Tuc is estimated to be several hundred (Camilo *et al.* 1999).

Measurements of the spindown rate for millisecond pulsars attest to magnetic fields of 10^8–10^9 G. Neutron stars with appreciable magnetic fields may manifest themselves as millisecond radio pulsars; NSs with weaker fields are simply unobservable at the current

* E-mail address for contacts: sibgat@mech.math.msu.su

sensitivity level of radio telescopes, but nothing forbids their existence.

Disk accretion onto a NS with a weak magnetic field, $H \le 10^8$ G, proceeds in 80 low-mass binaries of our Galaxy. Strong fields could affect the accretion dynamics and could give rise to periodic X-ray pulsations, which is not observed in these systems.

Accretion Pattern. Accreting matter with a large angular momentum spins up a neutron star (Pringle and Rees 1972; Bisnovatyĭ-Kogan and Komberg 1974; Alpar *et al.* 1982; Lipunov and Postnov 1984) and causes appreciable energy release in the accretion disk in a boundary layer near the NS surface (Shakura and Sunyaev 1988; Popham and Sunyaev 2000). Inogamov and Sunyaev (1999) considered the formation of a layer of accreting matter spreading over the surface of a neutron star without a magnetic field. The surface radiation was found to concentrate toward two bright rings equidistant from the stellar equator and the disk plane. The distance of the bright rings from the equator depends on the accretion rate alone.

In the course of accretion, the baryon and gravitational masses of the NS grow, its rotation velocity and moment of inertia change, a quadrupole component appears in its mass distribution, and its external gravitational field changes. For several standard equations of state of matter, the NS equatorial radius proves to be smaller than the equatorial radius of a marginally stable orbit over a wide range of rotation frequencies. This significantly affects the ratio of energy release in an extended disk and the stellar surface. The X-ray spectra of the accretion disk and the spread layer can differ greatly, which opens up a possibility for experimentally testing the theoretical results presented below.

Energy Release in the Disk and on the NS Surface. Here, we calculate the total energy release during accretion onto a rapidly rotating NS and determine the ratio of disk luminosity L_d to luminosity L_s of the spread layer on the stellar surface at a given accretion rate $\dot{M}$. Multiplying the efficiency of energy release ϵ_{grav} by $\dot{M}$ yields the sought-for luminosities. Clearly, allowance for radiation-pressure forces and for the detailed boundary-layer physics can slightly modify the derived formulas (Marcovic and Lamb 2000; Popham and Sunyaev 2000).

For the most important case of a NS with fixed gravitational mass $M = 1.4M_\odot$, we present the results of our calculations in Fig. 1. The calculations were performed for a moderately hard equation of state (EOS FPS). Below, we use the notation of Arnett and Bowers (1977) for EOS A (Pandharipande 1971), L, and M; EOS AU from Wiringa *et al.* (1988); and EOS FPS from Lorenz *et al.* (1993). EOS FPS is a modern version of the equation of state proposed by Friedman and Pandharipande (1981).

The approximation formula (derived in section 5) for the total NS luminosity as a function of cyclic rotation frequency (see Fig. 1) is

$$L_s + L_d \approx (0.213 - 0.153(f/1\ \text{kHz}) + 0.02(f/1\ \text{kHz}))\dot{M}c^2. \quad (1)$$

Here, f varies in the range from –1 to +1 kHz, with positive and negative f corresponding to NS and accretion-disk corotation and counterrotation, respectively. In this paper, a large proportion of the results in graphical form and in the form of approximation formulas are given for a NS gravitational mass of 1 $M_\odot$ or for normal sequences with a zero rest mass whose gravitational mass is $1.4M_\odot$ in the static limit for various equations of state of the matter in the NS interior. Amazingly, the measured mass M of an absolute majority of the millisecond pulsars in binaries lies, with high reliability, in a narrow range $1.35 \pm 0.04M_\odot$ (Thorsett and Chakrabarty 1998). Note, however, that the mass of the X-ray pulsar VELA X-1 is close to $1.8M_\odot$.

When observational data are interpreted, it is useful to have an approximation formula (EOS FPS) for the ratio of the NS surface and total luminosities,

$$L_s/(L_s + L_d) \approx 0.737 - 0.312(f/1\ \text{kHz}) - 0.19(f/1\ \text{kHz})^2. \quad (2)$$

We define the efficiency of energy release in the disk as the binding energy of a particle in a Keplerian orbit at the inner disk boundary. This orbit coincides with the marginally stable orbit or with the orbit at the NS equator.

For a NS of mass $M = 1.8M_\odot$ with EOS FPS, the calculated total luminosity and L_d/L_s are shown in Fig. 2. The corresponding approximation formulas are given in section 5.

We see from Figs. 1 and 2 that the surface luminosity L_s dominates over the disk luminosity for a slowly rotating star and in the case of counterrotation. Note that the effective energy release during accretion onto a NS of gravitational mass $M = 1.8M_\odot$ reaches $0.62\dot{M}c^2$ (at a cyclic frequency of NS rotation in the sense opposite to disk rotation equal to 1.41 kHz). For a normal sequence with a maximum mass losing stability in the static limit, the total energy release even reaches $0.67\dot{M}c^2$ (see Fig. 3). Note that the above values exceed appreciably the disk energy release $E_d = 0.422\dot{M}c^2$ during accretion onto a Kerr black hole with the largest possible rotation parameter $j = 1$. Clearly, such a high energy release is also associated with the loss of kinetic energy of stellar rotation during accretion of matter with an oppositely directed angular momentum.

The accretion-disk luminosity at $f \ge 600$ Hz exceeds the surface luminosity if the star rapidly rotates in the same sense as does the disk. We see from Fig. 1 that $L_s \approx L_d \approx 0.064\dot{M}c^2$ at $f = 600$ Hz.

This tendency is seen from simple Newtonian formulas (Kluzniak 1987; Kley 1991, Sibgatullin and Sunyaev 1998, below referred to as SS 98):

$$L_s = \frac{1}{2}\dot{M}GM/R(1 - f/f_K)^2, \quad (1a)$$

$$L_d = \frac{1}{2}\dot{M}GM/R.$$

Here, R is the equatorial stellar radius, and $f_K = \sqrt{GM/R^3}/(2\pi)$ is the Keplerian rotation frequency at the inner disk boundary. This formula is valid at low angular velocities, when, to a first approximation, NS oblateness can be disregarded. The exact formulas for L_s and L_d when the disk lies in the NS equatorial plane are (Sibgatullin and Sunyaev 2000; below referred to as SS 00)

$$L_s = 2\pi^2\dot{M}R^2(f_K - f)^2, \quad L_d = \dot{M}\frac{1}{2R}\frac{d\phi(r)r^2}{dr}\bigg|_{r=R}. \quad (1b)$$

Here, $\phi(r)$ is the gravitational potential in the disk plane as a function of distance from the NS. In particular, it follows from formula (1a) that, at $|f| = 0.5f_K$, the surface energy release for counterrotation is a factor of 9 greater than that for NS and disk corotation!

In Fig. 4, we present similar results of our calculations for stars of fixed rest mass (total baryon mass) m corresponding to $M = 1.4M_\odot$ in the static limit for the NS EOS FPS. The difference between this figure and Fig. 1 is not large, because the increase in gravitational mass through rapid rotation is relatively small [but appreciable; see formulas (18)].

For the fixed gravitational mass $M = 1.4M_\odot$, we derived a simple approximation formula for the gap between the equator of a rotating star with radius R and a marginally stable orbit for EOS FPS with radius R_*:

$$(R_* - R)/1\ \text{km} \approx 1.44 - 3.061(f/1\ \text{kHz}) + 0.843(f/1\ \text{kHz})^2 + 0.6(f/1\ \text{kHz})^3 - 0.22(f/1\ \text{kHz})^4. \quad (3)$$

Here, a considerable fraction of our results presented in graphical form or in the form of approximation formulas are given for a gravitational NS mass of $1.4M_\odot$. Amazingly, the measured masses M of most millisecond pulsars in binary systems lie with high reliability in a narrow range $1.35 \pm 0.04M_\odot$ (Thorsett and Chakrabarty 1998).

Using the Static Criterion for Stability. Here, we attempt to derive an approximation formula for the dependence of NS gravitational mass $M(j, m)$ on Kerr rotation parameter $j \equiv cJ/GM^2$ (where J is the NS angular momentum) and on its rest mass m.

We derive the function $M(j, m)$ (which is given below for two NS equations of state) by using the static criterion for the loss of stability and data obtained using the numerical code of Stergioulas (1998). Knowledge of $M(j, m)$ allowed us to derive formulas for the NS angular velocity and equatorial radius as functions of j and m.

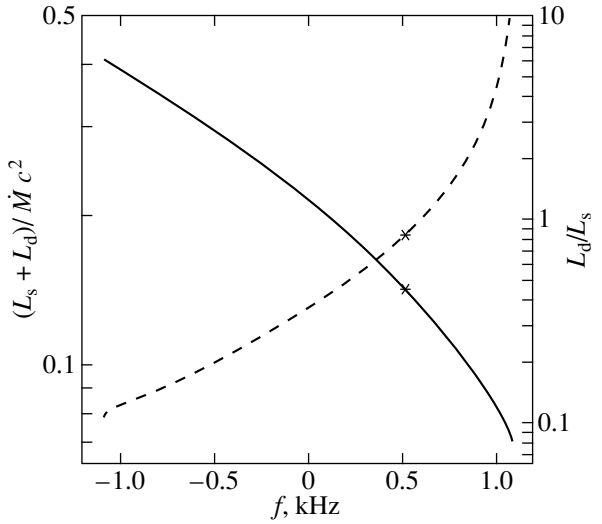

Fig. 1. Total energy release $L_s + L_d$ on the NS surface and in the accretion disk (solid line) and ratio of energy releases in the disk L_d and on the surface L_s (dashed line) versus NS rotation frequency f at the fixed gravitational mass $M = 1.4M_\odot$ for the moderately hard EOS FPS. The asterisks in Figs. 1–4 correspond to the frequency f at which the NS radius is equal to the radius of the marginally stable orbit. At $f \le f_*$, there is a gap between the accretion disk and the NS surface [see formula (3)].

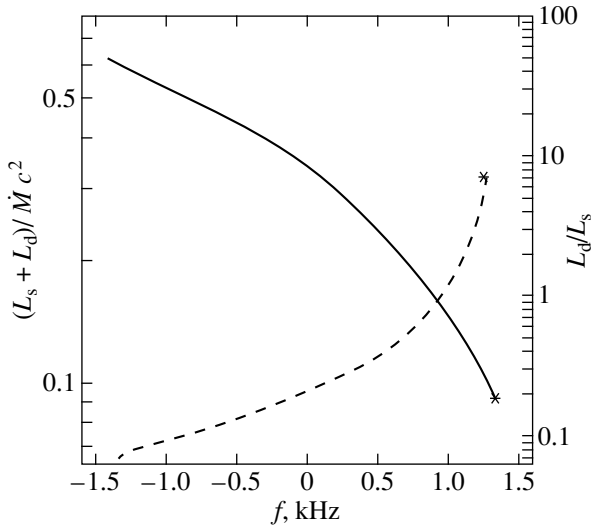

Fig. 2. Total energy release on the NS surface and in the accretion disk (solid line) and ratio of the disk and surface energy releases (dashed line) versus NS rotation frequency for the fixed gravitational mass $M = 1.8M_\odot$ (EOS FPS). The NS is stable to gravitational collapse only in the presence of rotation.

Metric Properties of a Rotating Neutron Star. Remarkably, the external field of a rapidly rotating NS with a mass larger than the solar one can be satisfacto-

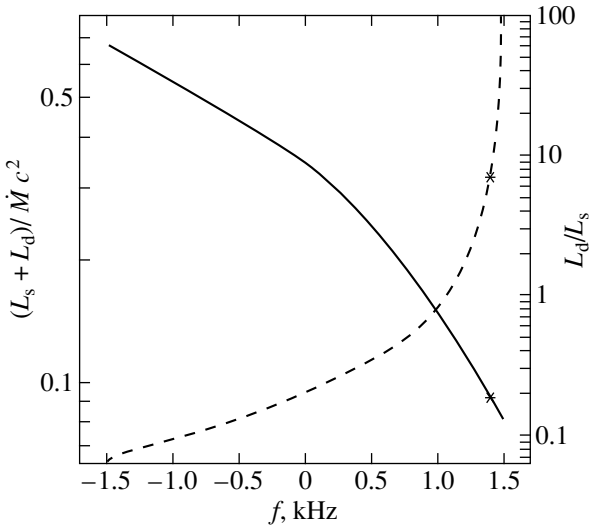

Fig. 3. Total energy release on the NS surface and in the accretion disk (solid line) and ratio of the disk and surface energy releases (dashed line) versus NS rotation frequency for the EOS FPS normal sequence with $m = 2.1M_\odot$ ($1.8M_\odot$ in the static limit).

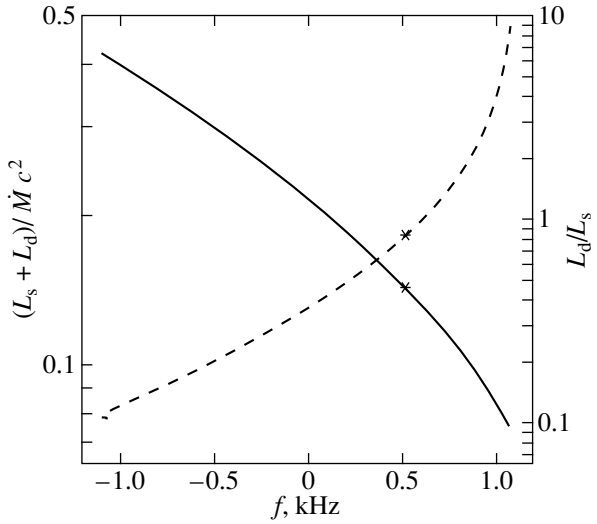

Fig. 4. Total energy release on the NS surface and in the accretion disk (solid line) and ratio of the disk and surface energy releases (dashed line) versus NS rotation frequency for the EOS FPS normal sequence with $m = 1.56M_\odot$ ($1.4M_\odot$ in the static limit). The asterisks correspond to the rotation frequency at which $R = R_*$.

rily described in terms of general relativity by introducing only one additional parameter compared to the Kerr metric—quadrupole moment of the mass distribution (SS 98). In sections 2 and 3, we discuss exact solutions that take into account higher multipole moments for low masses.

Analogous to $M(j, m)$, we managed to construct approximation dependences of the additional (to the Kerr one) dimensionless quadrupole coefficient b for the external gravitational field on j and m. Using these approximations in an exact solution for the metric outside rigidly rotating NSs enabled us to analytically calculate parameters of the marginally stable orbit in the accretion disk, energy release in the disk and on the NS surface, and the rate of NS spinup via disk accretion. In order to relate the derived approximation dependences to the observed NS parameters, we passed from the Kerr parameter j to the observed parameter f (cyclic rotation frequency) for $1.4M_\odot$ stars in the final formulas. In section 1, we give approximation formulas for the relationship of j to f and M.

The Content of the Paper. Below (in section 1), we present a method for global construction of the NS gravitational mass as a function of its Kerr rotation parameter j and rest mass m. The static criterion for stability underlies the method. The results of our calculations using the numerical code of Stergioulas (1998) are approximated by this method with a very small error.

The NS angular velocity and its equatorial radius are determined by using $M(j, m)$. We propose a new formula for the equatorial radius, which matches the exact one at $j = 0$.

In section 2, we present a method of constructing the quadrupole coefficient via $M(j, m)$ using an exact solution of the Einstein equations for the metric of the external gravitational field.

The exact solutions that describe the external fields of rigidly rotating stars with arbitrary multipole structure are discussed in section 3.

Global properties of the exact quadrupole solution are described in section 4. We note that the corresponding gravitational field in some region on the b, j plane (where b is the quadrupole coefficient) including low values of the quadrupole moment and the Kerr rotation parameter behaves as the field of two rotating black holes, with the NS pressure acting as an elastic support. However, outside this region, the solution properties outside the star are equivalent to the field of two supercritical Kerr disks. By contrast to black holes (Hoenselaers 1984), two Kerr disks can be in equilibrium in the absence of supports (Zaripov *et al.* 1994; a graphic post-Newtonian approach was developed by Zaripov *et al.* 1995).

In section 4, we derive expressions for the energy, angular momentum, radius, and angular velocity of particles in the marginally stable orbit in the quadrupole solution. The above functions depend on j and b. At $b = 0$ and $j = 1$, these expressions have numerical solutions which were first found by Ruffini and Wheeler (1970). At $b = 0$ and $j < 1$, the above expressions approximate the corresponding formulas of Bardeen *et al.* (1972) in the form of polynomials in j.

The energy, angular momentum, radius, and Keplerian angular velocity of particles at the stellar equator depend markedly on the NS equation of state. In section 4,

these functions are given as functions of j, m (and j, M) for EOS FPS and as functions of j, m for EOS A.

The above set of functions proves to be enough to calculate the dependences of energy release on the NS surface and in the accretion disk (section 5) on j, m or on j, M. In section 5, we provide approximation formulas for the total luminosity and the luminosity ratio of the disk and the NS surface as functions of rotation frequency at fixed gravitational masses $M = 1.4$ and $1.8M_\odot$ for EOS FPS. Similar approximation formulas are given for the EOS A and EOS AU normal sequences with $M = 1.4M_\odot$ in the static limit. In section 5, we also discuss the NS spinup and provide approximation formulas for the spinup rate in the case of EOS FPS for fixed gravitational masses of 1.4 and 1.8 $M_\odot$. For comparison, we give formulas for the dependence of luminosity and spinup parameter on the dimensionless rotation frequency in the Newtonian theory.

Astrophysical applications and implications of our results (particularly for the most interesting case of NS and disk counterrotation) are discussed in section 6.

1. THE STATIC CRITERION FOR STABILITY AND THE FUNCTION $M(j, m)$

The static stability criterion for nonrotating isentropic stars (planets) has been discussed in the literature since the early 1950s (Ramsey 1950; Lighthill 1950; Zel'dovich 1963; Dmitriev and Kholin 1963; Calamai 1970). It was generalized to rotating configurations by Bisnovatyi-Kogan and Blinnikov (1974) and Hartle (1975).

Below, we follow Zel'dovich (1963) in its interpretation. In what follows, M is the NS gravitational mass, and m is the total mass of its constituent baryons (rest mass). All masses are measured in solar masses, so equalities of the type $m = 1.16$ and $M = 1.4$ imply that $m = 1.16M_\odot$ and $M = 1.4M_\odot$, respectively.

We choose central density ρ as one of the independent arguments and angular momentum J as the second argument. It can then be shown that the extremum of gravitational mass M in central density at fixed angular momentum coincides with the extremum of rest mass m (Zel'dovich and Novikov 1971; Shapiro and Teukolsky 1985). At the extremum, a steady-state configuration becomes unstable to the neutral mode of quasi-radial oscillations. NS stable states can exist only at lower masses.

Denote the extremum central density at fixed angular momentum by $\rho_* = \rho_*(J)$. The functions $M(\rho, J)$ and $m(\rho, J)$ near the extremum at fixed angular momentum can then be expanded in Taylor series:

$$M(\rho, J) = M_* + a_1(\rho - \rho_*)^2 + a_2(\rho - \rho_*)^3 + a_3(\rho - \rho_*)^4 + \ldots, \quad (4)$$

$$m(\rho, J) = m_* + b_1(\rho - \rho_*)^2 + b_2(\rho - \rho_*)^3 + b_3(\rho - \rho_*)^4 + \ldots \quad (5)$$

The coefficients a_i and b_i ($i = 1, 2, \ldots$) in formulas (4) and (5) depend on J.

Equation (5) allows the central density ρ to be expressed as a power series of $\sqrt{m_* - m}$:

$$\rho = \rho_* + \rho_0(m_* - m)^{0.5} + \rho_1(m_* - m) + \rho_2(m_* - m)^{1.5} + \ldots$$

Substituting this expression for ρ in (4) yields

$$M - M_* = M_0(m_* - m) + M_1(m_* - m)^{1.5} + M_2(m_* - m)^2 + \ldots \quad (6)$$

In this formula, M_*, m_*, M_0, M_1, M_2, … are some functions of angular momentum J.

If, alternatively, the central density is expressed as a series in half-integer powers of $M - M_*$ using (4) and substituted in (5), then

$$m - m_* = m_0(M_* - M) + m_1(M_* - M)^{1.5} + m_2(M_* - M)^2 + \ldots \quad (7)$$

Note the formal similarity between the expansions (6), (7) and the expansions for the mass and radius near the point of phase transition at the stellar center in nonrotating stellar models with phase transitions in general relativity (Seidov 1971; Lindblom 1998).

Determining the Gravitational and Rest Masses at the Stability Boundary. The numerical code of Stergioulas (1998) allows NS parameters to be computed for a given equation of state by specifying a numerical value of the central density and one of the parameters M, m, Ω, J, Ω_K. The functions $M_*(J)$ and $m_*(J)$ can be determined as the maximum values of $M(\rho, J)$ and $m(\rho, J)$ for any fixed J by using this numerical code.

It is convenient to use a dimensionless angular momentum $j \equiv cJ/GM^2$ (Kerr rotation parameter) instead of the angular momentum J, because, apart from the mass, the metric of the external field of a rigidly rotating neutron star is determined precisely by this parameter. The functions $M_*(j)$ and $m_*(j)$ have the meaning of dependences of the gravitational and rest masses on Kerr parameter at the stability boundary.

We approximate $M(j, m)$ and $m(j, M)$ by the above terms of the expansions (6) and (7) in finite ranges of the parameters: $|j| \le 0.7$ and $1.1M_\odot < m < 2.5M_\odot$. For this approximation, the extremum property of the gravitational and rest masses at loss of stability is retained. It is this property that is the main idea behind the static criterion for stability.

Determining the NS Angular Velocity and its Moment of Inertia. In SS 00, we showed that

$$\Omega = 2\pi f = \left.\frac{\partial Mc^2}{\partial J}\right|_m, \tag{8}$$

where $|_m$ denotes, as usual, differentiation at constant m. Given the definition of j, we have from (8)

$$\Omega = 2\pi f = \left.\frac{\partial Mc^2}{\partial J}\right|_m$$
$$= \left.\frac{\partial M}{\partial j}\right|_m c^3/GM^2 - 2j\left.\frac{\partial Mc^2}{\partial J}\right|_m /M,$$

hence,

$$\Omega = \frac{c^3}{GM} M_{,j}|_m/(M + 2jM_{,j}|_m); \tag{9}$$
$$M_{,j}|_m \equiv \left.\frac{\partial M}{\partial j}\right|_m.$$

In what follows, a comma in the subscript denotes a partial derivative with respect to the corresponding argument. Using $M(j, m)$, we can also determine the moment of inertia

$$I = (\Omega_{,j}|_m)^{-1} = c^2(M_{,JJ}|_m)^{-1}$$
$$= \frac{G}{c}(M^2 + 2jmM_{,j}|_m)/\Omega_{,j}|_m.$$

At the stability boundary $m = m_*(j)$, we have from (7)

$$\Omega_*(j) = \frac{c^3}{GM_*(j)} \tag{10}$$
$$\times \frac{(M_*(j))' + M_0(j)(m_*(j))'}{(M_*(j) + 2j(M_*(j))' + M_0(j)(m_*(j))')}.$$

Here, the prime denotes a derivative of the corresponding function with respect to j.

Determining the Coefficients $M_0(j)$, $M_1(j)$, and $M_2(j)$. The coefficients $M_0(j)$, $M_1(j)$, and $M_2(j)$ in formula (6) are sought in the form of formal expansions in even powers of j. We calculate the limiting values of these function when $j \longrightarrow 0$ by approximating the dependence of gravitational mass on rest mass in the static case:

$$M_{st} = M_*(0) + M_0(0)(m_*(0) - m) \tag{11}$$
$$+ M_1(0)(m_*(0) - m)^{1.5} + M_2(0)(m_*(0) - m)^2 \ldots$$

Based on numerical data for Ω at the stability boundary $m = m_*(j)$, we determine $M_0(j)$ from formula (10) by using the derived functions $M_*(j)$ and $m_*(j)$.

In order to successively determine the remaining coefficients $M_1(j)$ and $M_2(j)$ before the nonstatic terms in (6), we introduce the coefficient $\mu_1 - m$, with $M_1(j)$ (whose value at $j = 0$ is already known) being calculated by using numerical data precisely at $m = \mu_1$. We then have

$$M_1(j) \tag{12}$$
$$= \frac{M(j, \mu_1) - M_0(j)(m_*(j) - \mu_1) - M_2(0)(m_*(j) - \mu_1)^2}{(m_*(j) - \mu_1)^{1.5}}.$$

Having numerical data for the right-hand part at discrete j, we can easily find a sixth-degree polynomial with the smallest rms deviation by points. In our calculations, we choose μ_1 in such a way that $M_{st}(\mu_1)$ is equal to or differs only slightly from $1.4M_\odot$.

Having derived the expression for $M_1(j)$, we can determine $M_2(j)$ by using a different normal sequence, say, at $m = \mu_2$.

We construct the coefficient $M_2(j)$ as follows:

$$M_2(j) \tag{13}$$
$$= \frac{M(j, \mu_2) - M_0(j)(m_*(j) - \mu_2) - M_1(j)(m_*(j) - \mu_2)^{1.5}}{(m_*(j) - \mu_2)^2}.$$

The Function M(j, m) for EOS A. We choose the following constants μ_1 and μ_2 for EOS A: $\mu_1 = 1.5663$ and $\mu_2 = 1.1663$. The numerical data of Stergioulas's code for the dependences of critical masses on j can be approximated as

$$M_*(j) = 1.659 + 0.489j^2 + 0.273j^4 + 0.32j^6,$$
$$m_*(j) = 1.9495 + 0.5144j^2 + 0.335j^4 + 0.38j^6. \tag{14}$$

Combining our results (10)–(14) for EOS A, we finally obtain

$$M(j, m) \approx M_*(j)$$
$$+ (-0.6473 - 0.019j^2 - 0.182j^4 + 0.23j^6)$$
$$\times (m_*(j) - m)$$
$$+ (-0.0808 - 0.039j^2 + 0.31j^4 - 0.34j^6) \tag{15}$$
$$\times (m_*(j) - m)^{1.5}$$
$$+ (-0.0457 + (0.059j^2 - 0.222j^4 + 0.28j^6)$$
$$\times (1.5663 - m))(m_*(j) - m)^2.$$

Formula (15) describes the data of Stergioulas's (1998) numerical code to within the fourth decimal place in mass (expressed in solar masses) and to within the third decimal place in angular velocity Ω calculated using (9) (and expressed in units of 10^4 rad s^{-1}) in the following parameter ranges: $-0.7 < j < 0.7$ and $1.1 < m < 2.4$.

The Function M(j, m) for EOS FPS. For EOS FPS, which is harder than EOS A, our numerical searches for the maximum gravitational and rest masses at fixed angular momentum lead to the following dependences

of these masses on rotation parameter at the stability boundary:

$$M_*(j) = 1.8016 + 0.572j^2 + 0.164j^4 + 0.54j^6;$$
$$m_*(j) = 2.104 + 0.619j^2 + 0.154j^4 + 0.71j^6. \quad (16)$$

Approximating the data for the static case $j = 0$ yields

$$M_{st} = 1.8016 - 0.6546(2.104 - m)$$
$$- 0.0846(2.104 - m)^{1.5} - 0.035(2.104 - m)^2 \ldots$$

We determine $M_0(j)$, $M_1(j)$, and $M_2(j)$ by the above procedure: for the rest masses of normal sequences, we choose $\mu_1 = 1.56$ and $\mu_2 = 1.16$. Of course, the choice of these values is rather arbitrary. The final formula derived from (10)–(13) and (16) for the dependence of gravitational mass on rotation parameter and rest mass for EOS FPS is

$$M(j, m) \approx M_*(j)$$
$$+ (-0.6538 - 0.0295j^2 - 0.242j^4 + 0.49j^6)$$
$$\times (m_*(j) - m)$$
$$+ (-0.0846 - 0.009j^2 + 0.302j^4 - 0.52j^6) \quad (17)$$
$$\times (m_*(j) - m)^{1.5}$$
$$+ (-0.035 + (0.039j^2 - 0.188j^4 + 0.32j^6)$$
$$\times (1.56 - m))(m_*(j) - m)^2.$$

Formula (17) for the gravitational mass, like the previous (15), approximates the numerical data of Cook *et al.* (1994) and the results of Stergioulas's (1998) code in the argument ranges $-0.7 < j < 0.7$ and $1.1 < m < 2.5$ with an amazing accuracy: to within the fourth decimal place in gravitational mass and to within the third decimal place in angular velocity (expressed in units of 10^4 rad s^{-1}).

The Function m(j, M) for EOS FPS. Similarly, we can approximate $m(j, M)$ by using numerical data for the angular velocity, the baryon and gravitational masses at the stability boundary, and for the fixed $M = 1.4M_\odot$ and $M = M_\odot$. For EOS FPS, we then obtain

$$m(j, M) \approx m_*(j)$$
$$+ (-1.528 + 0.059j^2 + 0.45j^4 - 0.72j^6)$$
$$\times (M_*(j) - M)$$
$$+ (0.269 - 0.076j^2 - 0.354j^4 + 0.6j^6)$$
$$\times (M_*(j) - M)^{1.5}$$
$$+ (0.004 + (-0.121j^2 + 0.68j^4 - 1.05j^6)$$
$$\times (1.4 - M))(M_*(j) - M)^2.$$

The Dependence of Gravitational Mass and Dimensionless Angular Momentum j on Angular Velocity for $1.4M_\odot$ Normal Sequences in the Static Limit. At present, the gravitational masses and angular velocities of neutron stars are measured with a high accuracy (Thorsett and Chakrabarty 1998). Here, we give, for reference, approximations of $M(f)$ and $j(f)$ for various equations of state for $M = 1.4M_\odot$ normal sequences in the static limit (here, the masses are in solar masses, and $f = \Omega/2\pi$ is the cyclic rotation frequency):

EOS A: $M \approx 1.4 + 0.0075(f/1\text{ kHz})^2 + 0.0055(f/1\text{ kHz})^4$,
$j \approx 0.274(f/1\text{ kHz}) + 0.14(f/1\text{ kHz})^2$, $m = 1.566$;

EOS AU: $M \approx 1.4 + 0.01(f/1\text{ kHz})^2 + 0.006(f/1\text{ kHz})^4$,
$j \approx 0.34(f/1\text{ kHz}) + 0.12(f/1\text{ kHz})^2$, $m = 1.578$;

EOS FPS: $M \approx 1.4 + 0.01(f/1\text{ kHz})^2 + 0.0087(f/1\text{ kHz})^4$,
$j \approx 0.338(f/1\text{ kHz}) + 0.19(f/1\text{ kHz})^2$, $m = 1.56$;

EOS L: $M \approx 1.4 + 0.019(f/1\text{ kHz})^2 + 0.0345(f/1\text{ kHz})^4$,
$j \approx 0.56(f/1\text{ kHz}) + 0.61(f/1\text{ kHz})^2$, $m = 1.52$;

EOS M: $M \approx 1.4 + 0.0195(f/1\text{ kHz})^2 + 0.071(f/1\text{ kHz})^4$,
$j \approx 0.55(f/1\text{ kHz}) + 1.04(f/1\text{ kHz})^2$, $m = 1.494$. (18)

The right-hand parts approximate $M(f)$ and $j(f)$ in the entire range $0 \le f < f_K$; they were constructed on the basis of tables from Cook *et al.* (1994). These approximations are extended to negative f (counterrotation) by using the evenness condition for $M(f)$ and the oddness condition for $j(f)$: $j(-f) = -j(f)$.

It follows from the formulas for $M(f)$ that the dependence of gravitational mass on angular velocity for the harder EOS L and M is stronger than that for the softer equations of state. While matching in the static limit, the gravitational masses of a NS with different equations of state differ at $f = 600$ Hz:

$$M_A = 1.4034, \quad M_{AU} = 1.4043, \quad M_{FPS} = 1.4047,$$
$$M_L = 1.4113, \quad M_M = 1.4162.$$

The difference in the equations of state leads to a marked difference in the gravitational masses (for the same mass in the static limit) for the same rotation period. These differences exceed the accuracy of measuring the gravitational masses of millisecond pulsars in some binary systems (Thorsett and Chakrabarty 1998).

Determining the Equatorial Radius of a Neutron Star. Another important formula relating the constant μ (stellar chemical potential) to the derivative of the gravitational mass with respect to the rest mass at constant angular momentum, follows from theorem 3 in SS 00. Taking the value of μ at the equator, we obtain

$$\mu = M_{,m}|_J = M_{,m}|_j/(1 + 2jM_{,j}|_m)$$
$$= \sqrt{F - 2\omega f\tilde{\Omega} - (Rc^2/GM)^2\tilde{\Omega}^2}, \quad (19)$$
$$(Rc^2/GM)^2 = t/F - F^2\omega. \quad (20)$$

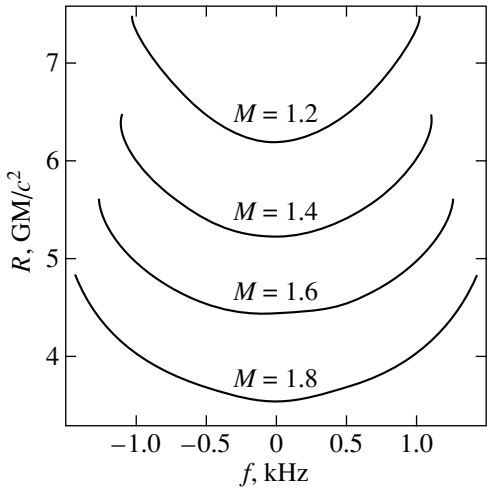

Fig. 5. Equatorial radius R versus NS rotation frequency for fixed gravitational masses M = const (EOS FPS).

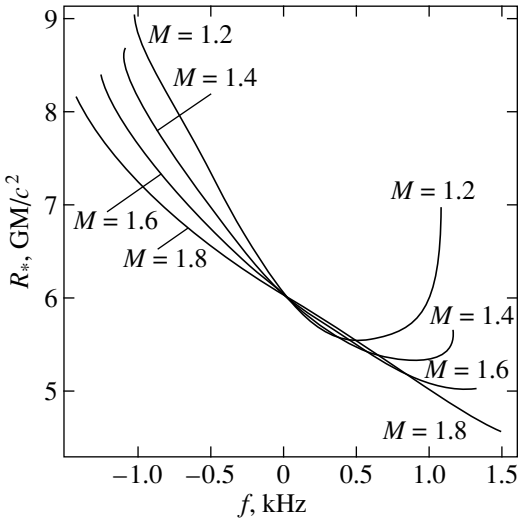

Fig. 6. Radius R_* of the marginally stable orbit versus NS rotation frequency for fixed gravitational masses M = const (EOS FPS).

Here, R is the NS geometric equatorial radius (the equator length divided by 2π), and $\tilde{\Omega} = \Omega GM/c^3$ is its dimensionless angular velocity. Below, we use a stationary, axially symmetric metric in Papapetru's form outside the star:

$$ds^2 = -F(dt - \omega d\phi)^2 + F^{-1}[\rho^2 d\phi^2 + e^{2\gamma}(d\rho^2 + dz^2)]. \quad (21)$$

In the static limit, the stellar radius can be determined from formula (20) by using the Schwarzschild metric

$$\frac{R_{st}c^2}{GM} = \frac{2}{1 - M_{,m}^2}, \quad M_{,m} \equiv \frac{dM}{dm}. \quad (22)$$

Remarkably, formula (22) for a rotating NS, if $M(j, m)$ is substituted in it and differentiated at constant j:

$$R \approx \frac{2GM/c^2}{1 - M_{,m}^2\big|_j}, \quad M_{,m}\big|_j \equiv \frac{\partial M}{\partial m} \quad (23)$$

closely agrees with the numerical data for the stellar equatorial radius from Cook *et al.* (1994) and with our data obtained by using the numerical code of Stergioulas (1998) with an accuracy up to 1%.

The NS Equatorial Radius and the Gap between the Marginally Stable Orbit and the Equator. Figure 5 shows plots of equatorial radius R (in units of GM/c^2) against rotation frequency f constructed using formula (23) for fixed gravitational masses M = 1.2, 1.4, 1.6, and $1.8M_\odot$ and for EOS FPS. In particular, the approximation of $R(f)$ at $M = 1.4M_\odot$ has a fairly simple form:

$$R/1\text{ km} = 11 + 1.78(f/1\text{ kHz})^4. \quad (24)$$

Figure 6 shows plots of radius R_* of the marginally stable orbit against f constructed using formula (47) for the same M. In particular, the approximation of $R_*(f)$at $M = 1.4M_\odot$ by a fourth-degree polynomial in the range $-1 < f < 0.6$ kHz is (EOS FPS)

$$R_*/1\text{ km} = 12.44 - 3.061(f/1\text{ kHz}) + 0.843(f/1\text{ kHz})^2 + 0.6(f/1\text{ kHz})^3 + 1.56(f/1\text{ kHz})^4. \quad (25)$$

In order to characterize the gap between the NS surface and the marginally stable orbit, let us consider the quantity $R_* - R$. In Fig. 7, $R_* - R$ is plotted against angular velocity for the same gravitational masses. The approximation of this dependence for $M = 1.4M_\odot$ is

$$(R_* - R)/1\text{ km} \approx 1.44 - 3.061(f/1\text{ kHz}) + 0.843(f/1\text{ kHz})^2 + 0.6(f/1\text{ kHz})^3 - 0.22(f/1\text{ kHz})^4. \quad (26)$$

These formulas can be used in the range $-1 < f < 0.6$ kHz.

In order to compare the gaps between the marginally stable orbit and the surface of a NS with different equations of state, we approximate the gap for $M = 1.4M_\odot$ normal sequences for a NS with EOS A and EOS AU as follows:

$$\text{EOS A: } (R_* - R)/1\text{ km} \approx 3 - 2.44f/1\text{ kHz} - 0.2(f/1\text{ kHz})^2, \quad (27)$$

$$\text{EOS AU: } (R_* - R)/1\text{ km} \approx 2.086 - 2.81f/1\text{ kHz} - 0.23(f/1\text{ kHz})^2. \quad (28)$$

2. THE QUADRUPOLE MOMENT OF A RAPIDLY ROTATING NEUTRON STAR IN GENERAL RELATIVITY

In order to describe the oblateness effect and the emergence of a quadrupole moment in the mass distribution via rapid rotation, in SS 98 we proposed to use an exact quadrupole solution, which contains an arbitrary parameter b compared to the Kerr metric. This parameter, to within a factor, matches the NS inherent quadrupole momentum: the total quadrupole moment in the asymptotics at large distances $\Phi_2 = G^2M^3/c^4(b + j^2)$ includes the Kerr quadrupole moment. The parameter Φ_2 was determined by Ryan (1995, 1997) from the considerations developed by Komatsu *et al.* (1989) and Salgado *et al.* (1994).

The Metric of the Quadrupole Solution in the Equatorial Plane. The metric components in the equatorial plane for this solution are (SS 98)

$$F = \frac{A-B}{A+B}, \quad \omega/M = -\frac{2jC}{A-B},$$
$$A \equiv (r_+ + r_-)^2 r_+ r_- - b, \tag{29}$$
$$B \equiv (r_+ + r_-)(r_+ r_- - b + r).$$

Here,

$$C \equiv (r_+ + r_-)(r_- r_+ + r) + b,$$
$$2r_\pm \equiv \sqrt{4r + (\sqrt{1-j^2} \pm \sqrt{1-j^2-4b})^2},$$
$$r \equiv \rho^2/M^2.$$

An exact quadrupole solution of the Einstein equations is contained as a special case in the exact five-parameter solution found by Manko *et al.* (1994) by specifying its properties on the symmetry axis using the method of Sibgatullin (1984). Ernst (1994) showed that this solution could also be obtained from Kramer–Neugebauer's (1980) solution for coaxially rotating black holes by a special choice of the constants in the solution.

The solution under consideration for $b < 0.25(1 - j^2)$ can be interpreted as a solution that describes the gravitational field of two coaxially rotating black holes with the same masses and angular momenta. For $b > 0.25(1 - j^2)$, it describes the gravitational field of coaxially rotating Kerr disks. In this case, the pressure clearly acts as elastic supports. For the curve of transition from black holes to Kerr disks to be found in the j, m plane, the equation $b(j, m) = 0.25(1 - j^2)$ must be solved.

Why the Kerr Metric Cannot Be Used to Describe the External Field of a Rapidly Rotating Neutron Star? Let us consider the dependence of the NS quadrupole moment on its angular velocity for various equations of state, from the soft EOS A to the hard EOS L. We express the quadrupole moment $\Phi_2 = G^2M^3(b + j^2)/c^4$ and the cyclic angular velocity in units of 10^{44} g cm^2 and kHz, respectively. We fix the corresponding normal

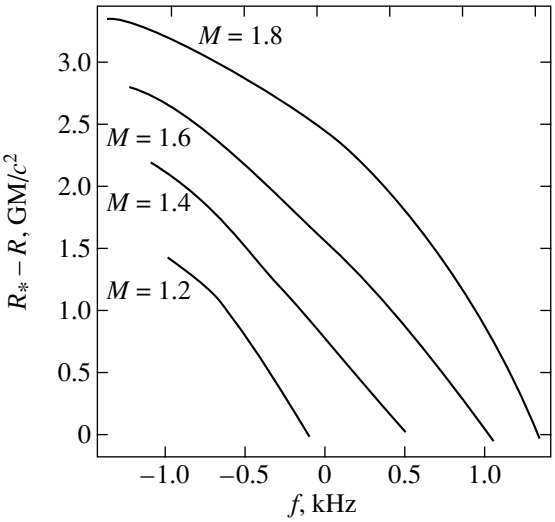

Fig. 7. Width R_*–R of the gap between the marginally stable orbit and the NS equator versus NS rotation frequency for fixed gravitational masses M = const (EOS FPS).

sequences (by definition, with a constant rest mass) by the condition that the NS gravitational mass is $1.4M_\odot$ in the static limit. Compare the total NS quadrupole moment with the Kerr quadrupole moment $Q_K = G^2M^3j^2/c^4$ (determined by the NS mass and angular momentum). Let us change to an observable variable, the rotation frequency f. Parabolic approximations of the dependence of dimensionless quadrupole coefficient b on Kerr parameter j are given in Laarakkers and Poisson (1998); more accurate approximations by fourth-degree polynomials in j were derived in SS 98. Having reduced the data obtained with the numeric code of Stergioulas (1998), we have

$$\text{EOS A: } \Phi_2/10^{44} \text{ g cm}^2$$
$$\approx 0.33(f/1\text{ kHz})^2 + 0.306(f/1\text{ kHz})^4,$$
$$Q_K/10^{44} \text{ g cm}^2 \approx 0.11(f/1\text{ kHz})^2 + 0.09(f/1\text{ kHz})^4;$$
$$\text{EOS AU: } \Phi_2/10^{44} \text{ g cm}^2$$
$$\approx 0.64(f/1\text{ kHz})^2 + 0.43(f/1\text{ kHz})^4,$$
$$Q_K/10^{44} \text{ g cm}^2 \approx 0.16(f/1\text{ kHz})^2 + 0.12(f/1\text{ kHz})^4; \tag{30}$$
$$\text{EOS FPS: } \Phi_2/10^{44} \text{ g cm}^2$$
$$\approx 0.54(f/1\text{ kHz})^2 + 0.9(f/1\text{ kHz})^4,$$
$$Q_K/10^{44} \text{ g cm}^2 \approx 0.13(f/1\text{ kHz})^2 + 0.22(f/1\text{ kHz})^4;$$
$$\text{EOS L: } \Phi_2/10^{44} \text{ g cm}^2$$
$$\approx 4.8(f/1\text{ kHz})^2 + 6.5(f/1\text{ kHz})^4,$$
$$Q_K/10^{44} \text{ g cm}^2 \approx 0.54(f/1\text{ kHz})^2 + 1.16(f/1\text{ kHz})^4.$$

Whereas the total quadrupole moment for the soft EOS A is approximately a factor of 3 larger than the Kerr component, for the hard EOS L, it exceeds the Kerr component by almost a factor of 10!

Determining the Non-Kerr Quadrupole Moment of a Rapidly Rotating NS Using M(j, m). The NS equato-

rial radius R is closely related to its quadrupole moment $\Phi_2 = G^2M^3j^2(k + 1)/c^4$. The system of equations (19) and (20) at given j and m in the metric (21) and (29) is algebraic for the NS coordinate radius ρ and its quadrupole moment b, because, according to (9) and (23), the functions $\Omega(j, m)$ and $R(j, m)$ are expressed in terms of $M(j, m)$ and its partial derivatives. We emphasize that $M(j, m)$, $R(j, m)$, $b(j, m)$, and $I(j, m)$ (moment of inertia) are even functions of the Kerr parameter j, while the angular velocity Ω is an odd function of j.

In the approximation of slow rotation, $b \sim j^2$. Denote $b \equiv j^2k$. The quadrupole moment can be approximated in finite ranges, $|j| \le 0.67$ and $1.1 < m < 2.5$, as a function of j, m or as a function of j, M.

We derive an approximation formula for $k(j, m)$ by a method similar to that described above for constructing $M(j, m)$ and $m(j, M)$: the function k is first approximated by a sixth-degree polynomial at the stability boundary in the segment $|j| \le 0.67$ in terms of the rms deviation and then by eighth-degree polynomials in j at two fixed values, say, $m = 1.56$ and 1.2358 ($M = 1.4$ and 1, respectively) in the segment $|j| \le 0.67$.

The Quadrupole Moment as a Function of j, m or j, M for EOS FPS. The resulting formula for $k(j, m)$ is a combination of four rms approximations and describes $b(j, m)$ to within the third decimal place.

For the quadrupole moment of an NS with EOS FPS rotating arbitrarily fast (up to the Keplerian angular velocity at the stellar equator), the following formula holds:

$$\begin{aligned}
&\Phi_2 = G^2M^3j^2(k+1)/c^4,\\
&k \approx k_*(j) + (1.525 - 3.365j^2 - 9.138j^4\\
&+ 23.37j^6 - 28j^8)(m_*(j) - m)^{0.5} + (0.62 + 3.086\\
&\times (0.188 - 3.447j^2 + 4.83j^4 + 5.11j^6 - 19j^8)\\
&\times (1.56 - m))(m_*(j) - m)\\
&+ 3.97(m_*(j) - m)^2 \approx k_*(j)\\
&+ (1.693 - 4.196j^2 - 12.268j^4 + 30.32j^6 - 37.2j^8)\\
&\times (M_*(j) - M)^{0.5} + (1.713 + 2.5(0.348 - 6.515j^2\\
&+ 8.285j^4 + 9j^6 - 31j^8)(1.4 - M))(M_*(j) - M)\\
&+ 5.453(M_*(j) - M)^2.
\end{aligned} \tag{31}$$

Here, $k_*(j)$ denotes the function at the stability boundary. It follows from our numerical data that $k_*(j) \approx 0.567 - 0.576|j| + 0.338j^2 - 0.47j^4 + 0.19j^6$; $M_*(j)$ and $m_*(j)$ are given by (16).

The Quadrupole Moment as a Function of j, m for EOS A. For EOS A, the formula for the inherent quadrupole coefficient can be written as

$$\begin{aligned}
&\Phi_2 = G^2M^3j^2(k+1)/c^4,\\
&k \approx 0.556 - 0.862|j| + 0.795j^2 - 0.611j^4\\
&+ (1.15 + 0.344|j| - 3.68j^3 - 3.62j^4)\\
&\times \sqrt{m_*(j) - m} + (1.196\\
&+ (1.1075 - 7.7013|j| + 3.574j^2)\\
&\times (1.5663 - M_0))(m_*(j) - m)\\
&+ 4.183(m_*(j) - m)^2.
\end{aligned} \tag{32}$$

Here, $M_*(j)$ and $m_*(j)$ are given by (14).

Results of Our Calculations. Figure 8 shows lines of constant gravitational mass $M(f, m)$ as functions of rotation frequency f for m at 0.1 steps in the interval (1.2, 2.5) for EOS FPS (recall that the masses are measured in $M_\odot$). We used the parametric dependences $M = M(j, m)$ and $\Omega = \Omega(j, m)$ [see formula (9) for $\Omega(j, m)$] to construct these curves. The dashed curve in Fig. 8 separates the NS states when it is within the marginally stable orbit from the NS states when this orbit is inside it. Obviously, the equation of this curve is $R(j, m) = R_*(j, m)$. The dots indicate the curves of stability loss according to the static criterion. Their parametric equation is $M = M_*(j)$ and $f = f_*(j)$.

The moment of inertia, the angular velocity, the equatorial radius, and the quadrupole moment can be inferred from the derived function $M(j, m)$, which determines the state of a two-parameter thermodynamic system.

Figure 9 shows lines of constant dimensionless quadrupole coefficient b as functions of rotation frequency f for rest masses at 0.1 steps in the interval (1.2, 2.5). In this case, the dimensionless angular momentum j acts as a parameter in the parametric specification of the curve on the plane. Points a, … in Figs. 8 and 9 correspond to the curve of transition from the external field of two coaxially rotating black holes to the external field of two coaxially rotating Kerr disks. The equation of this curve is $b(j, m) = 0.25(1 - j^2)$.

3. THE EXTERNAL GRAVITATIONAL FIELDS OF RAPIDLY ROTATING NEUTRON STARS

The External Gravitational Fields of Sources with a Finite Set of Multipole Moments. The external gravitational fields of rapidly rotating neutron stars at large angular velocities differ markedly from the Kerr field. To describe these fields by the solution of the Einstein equations with a finite set of multipole parameters, in SS 98 we proposed to use axisymmetric steady-state

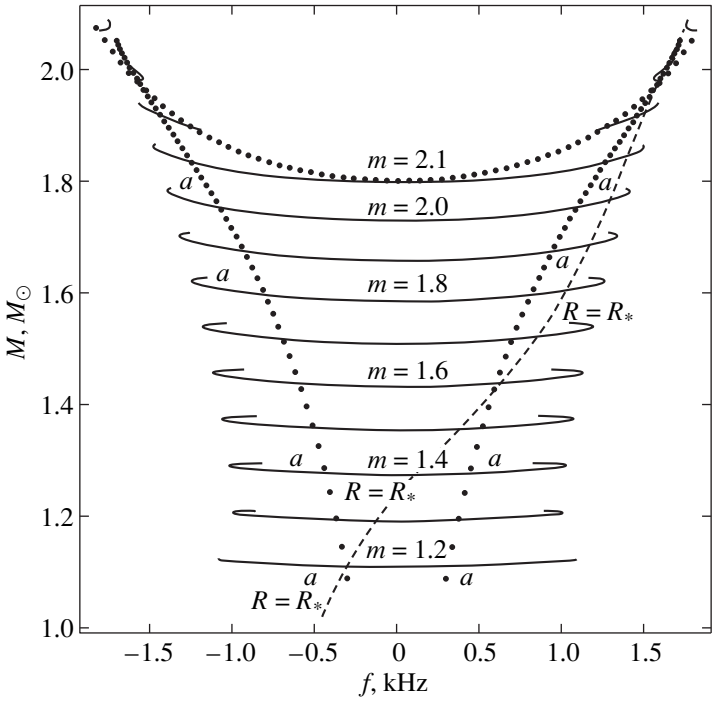

Fig. 8. Gravitational mass M versus NS rotation frequency for fixed rest masses (EOS FPS). The dashed line corresponds to the parameters at which $R = R_*$. Curves a correspond to a transition of the external field from the field of two Kerr black holes (inner region) to the field of two Kerr disks (outer region). The maximum gravitational masses at which the stability is lost according to the static criterion are also marked by dots (upper curve).

solutions specified on the symmetry axis by the following Ernst potential:

$$e(z) = \mathbf{E}|_{\rho=0} = \frac{z^n - z^{n-1} + \sum_{j=1}^{n} a_j z^{n-j}}{z^n + z^{n-1} + \sum_{j=1}^{n} a_j z^{n-j}}. \quad (33)$$

Below, the ρ and z coordinates are measured in units of length (GM/c^2).

The corresponding solution is symmetric about the equatorial plane if we additionally require that the coefficients with even subscripts a_{2k} be real (they are determined by the mass distribution and correspond to the Newtonian multipole moments), and that the coefficients with odd subscripts a_{2k-1} be purely imaginary (they are determined by the angular-momentum distribution in the NS and have no analog in the Newtonian theory). For this definition of multipole moments, the Kerr solution is a purely dipole one, and its higher multipoles are zero. General expressions for the metric coefficients are given in SS 98 [formulas (23) and (24)]. Denote the roots of the denominator in the expression for $\mathbf{E}$ on the symmetry axis by $b_1, b_2, \ldots, b_n$ and the roots of the equation $e(z) + \tilde{e}(z) = 0$ by $\pm\xi_1, \pm\xi_2, \ldots, \pm\xi_n$ (Sibgatullin 1984). Here, the tilde has the meaning of a complex conjugate. If we use the identity

$$\prod_{k=1}^{n} P(a_k)\det\left(\frac{1}{a_i - b_j}\right) = -V(a_1, \ldots, a_n)V(b_1, \ldots, b_n)$$

[here, $V(a_1, \ldots, a_n)$ is an $n \times n$ alternant on elements $a_1, \ldots, a_n$; and $P(z)$ is an nth-degree polynomial whose roots are $b_1, \ldots, b_n$], then we can represent the solution for the Ernst function differently. To describe it, we denote

$$\gamma_k \equiv a_1 + \frac{a_3}{\xi_k^2} + \ldots; \quad \sigma_k^{\pm} \equiv \pm\sqrt{1-\gamma_k^2} + i\gamma_k; \quad (34)$$

$$r_k^{\pm} \equiv \sqrt{\rho^2 + (z \mp \xi_k)^2};$$

$$a_{kl} \equiv r_l^{+}\sigma_l^{+}\xi_l^{k-1}; \quad b_{kl} \equiv r_l^{-}\sigma_l^{-}(-\xi_l)^{k-1}; \quad (35)$$

$$c_{kl} \equiv \xi_l^{k-1}; \quad d_{kl} \equiv (-\xi_l)^{k-1}.$$

The solution for the Ernst function symmetric about the equatorial plane and with the specified behavior on the symmetry axis (28) then takes a fairly elegant form:

$$\mathbf{E} = \frac{U-W}{U+W}; \quad U = \det\begin{pmatrix} A, & B \\ C, & D \end{pmatrix}, \quad (36)$$

$$W = \det\begin{pmatrix} A', & B' \\ C', & D' \end{pmatrix}.$$

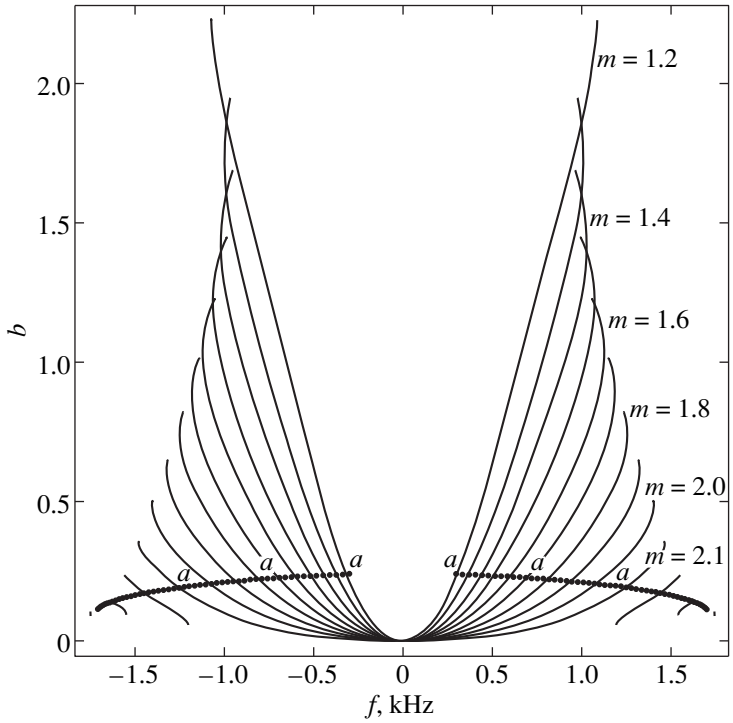

Fig. 9. Dimensionless quadrupole coefficient b versus rotation frequency f at fixed rest masses m (EOS FPS). Curves a correspond to a transition of the external field from the field of two Kerr black holes to the field of two Kerr disks. The curves were constructed at steps $\Delta m = 0.1$.

The square $n \times n$ matrices A, B, C, D consist of a_{kl}, b_{kl}, c_{kl}, d_{kl} (k, $l = 1, \ldots, n$), respectively [see Eq. (35)]. The rectangular $(n-1) \times n$ matrices A', B' consist of a_{kl}, b_{kl} ($k = 1, \ldots, n-1$; $l = 1, \ldots, n$), and the rectangular $(n+1) \times n$ matrices C', D' consist of c_{kl}, d_{kl} ($k = 1, \ldots, n+1$; $l = 1, \ldots, n$).

Formally, the solution (36) appears as the result of applying Backlund's transformation to the solution $\mathbf{E} = 1$ $2n$ times. For the Ernst equation, it was found by Neugebauer (1980) [see formula (7) from Kramer and Neugebauer (1980)]. However, an attempt to directly determine the parameters of this solution from the data on the axis leads to cumbersome calculations even for $n = 2$. Ernst (1994) established a relation between Sibgatullin's method of constructing electrovac solutions with a given rational behavior on the symmetry axes and Neugebauer's $2n$ parametric family of solutions for $n = 2$. Manko and Ruiz (1998) were able to represent the solution of the Ernst equations corresponding to the Ernst rational function on the symmetry axis with the asymptotics $\mathbf{E} \longrightarrow 1$ when $z \longrightarrow \infty$ in a form that contained only the roots ξ_k of the equation $e(z) + \tilde{e}(z) = 0$ and that did not contain the roots b_k for arbitrary $n > 2$.

We hypothesized in SS 98 that the coefficients a_{2k-1} for rigidly rotating stars, which are related to differential rotation, were zero for $k > 1$, with $a_1 \equiv j \neq 0$. This coefficient is the ratio of the NS angular momentum to its mass squared. Then, a substantial simplification of the solution (36) is that all constants σ_k^+ and σ_k^- [defined in (34)] turn out to be equal:

$$\sigma_k^+ = \sqrt{1 - j^2} + ij, \quad \sigma_k^- = -\sqrt{1 - j^2} + ij,$$
$$k = 1, \ldots, n.$$

An Exact Solution of the Einstein Equations for a Rotating Deformed Source and Numerical Data. The available numerical data on the external gravitational fields of rigidly rotating neutron stars [forward (Z_f) and backward (Z_b) redshifts at the equator edges, which allow the metric coefficients F and ω on the stellar equator to be calculated; see Cook *et al.* (1994) for numerical values of the radius of the marginally stable orbit] suggest that these fields can be described by some exact solution of the Einstein equations. The corresponding Ernst function on the symmetry axis is

$$e(z) = \frac{z^2 - (1 + ij)z + b}{z^2 + (1 - ij)z + b}, \qquad (37)$$

which is obtained from the general case (33) at $n = 2$. Recall that $J = GM^2j/c$ is the angular momentum, and G^2bM^3/c^4 is the quadrupole moment of the NS. Manko *et al.* (1994, 2000) proposed to model the external fields of neutron stars with strong magnetic fields by special exact solutions of the system of Einstein–Maxwell equations.

In contrast to the multipole decompositions at large radii (Shibata and Sasaki 1998; Laarakkers and Poisson

1998), which converge slowly at the stellar surface, the quadrupole solution closely approximates numerical data up to the stellar surface. The parameter $b = b(j)$ of this solution can be independently determined by several methods: for example, by comparing either the radius of the marginally stable orbit or the metric coefficient F at the stellar surface, which is $((1 + Z_f)(1 + Z_b))^{-1}$ (recall that $1/\sqrt{F} - 1$ has the meaning of gravitational redshift), with numerical data. The metric coefficients F and ω in the solution corresponding to (37) on the symmetry axis take the form (29) in the equatorial plane.

Remarkably, $b = b(j)$ determined from independent comparisons with numerical data proved to be the same for a given equation of state and at fixed rest mass.

The function $R_*(j)/M$ constructed from the Kerr solution differs markedly from the realistic curves for $|j| > 0.15$. Nevertheless, the realistic $R_*(j)c^2/GM$ curves and the Kerr curve have a tangency of the first order at $j = 0$. This circumstance serves as a good illustration of the remarkable observation by Hartle and Thorne (1969) that the external gravitational field of a slowly rotating star is described by the Kerr metric linearized in rotation parameter.

Here, by contrast to SS 98, we approximated the function $b(j, m)$ in finite ranges of j and m [see formulas (26) and (27)].

4. GLOBAL PROPERTIES OF THE EXACT QUADRUPOLE SOLUTION

Parameters of Equatorial Circular Orbits in an Arbitrary Axisymmetric Stationary Field in a Vacuum. The specific energy and angular momentum of particles rotating in the equatorial plane in a Keplerian circular orbit in an arbitrary axisymmetric stationary field in a vacuum can be calculated using the formulas (SS 98)

$$\begin{gathered} E = \frac{\sqrt{F}}{\sqrt{1 - F^2 p^2/r}}, \quad l = MGc^{-1}(p + \omega)E, \\ p \equiv r(-\lambda + \sqrt{\lambda^2 + \mu - \mu^2 r})/n, \\ \lambda \equiv F\dot{\omega}, \quad \mu \equiv \dot{F}/F, \quad n \equiv F - r\dot{F}. \end{gathered} \tag{38}$$

Here, the dot denotes a derivative with respect to $r \equiv \rho^2$.

For the angular velocity of a particle in a Keplerian circular orbit, we can derive the formula

$$\Omega_K = \frac{c^3}{GM}\frac{p}{(r/F^2 + \omega p)}. \tag{39}$$

The radius of the marginally stable orbit can be determined by using the condition of energy extremum in circular orbits. In explicit form, it appears as

$$\begin{gathered} r(\lambda\mu n + \dot{\lambda} n - \dot{n}\lambda)\sqrt{\lambda^2 + \mu - \mu^2 r} \\ - (\lambda^2 + \mu - \mu^2)(n - r\dot{n}) \\ - rn(\lambda\dot{\lambda} + 0.5(\dot{\mu} - \mu^2) - r\mu\dot{\mu}) = 0. \end{gathered} \tag{40}$$

For the particle energy and angular momentum in the marginally stable orbit to be calculated as functions of rotation parameter j, the root of the algebraic equation (40) must be substituted in (38).

Disk Luminosity and Parameters of Equatorial Circular Orbits in the Kerr Field. The external field of a slowly rotating NS can be described by the Kerr solution linearized in angular momentum (Hartle and Thorne 1969). The physical processes in the field of a slowly rotating NS were considered by Kluzniak and Wagoner (1985), Sunyaev and Shakura (1986), Ebisawa *et al.* (1991), Biehle and Blanford (1993), and Miller and Lamb (1996).

For the extreme Kerr solution ($j = 1$), the particle energy and angular momentum in the marginally stable orbit were calculated by Ruffini and Wheeler (1970) in their pioneering study.

At $0 \le j \le 1$, the particle energy and angular momentum in circular orbits in the Kerr field (Bardeen *et al.* 1972) are related to the orbital radius and the rotation parameter j by

$$\begin{gathered} E = \frac{1 - 2x + jx\sqrt{x}}{\sqrt{1 - 3x + 2jx\sqrt{x}}}, \\ l = GM/c\frac{-2jx + (1 + j^2x^2)/\sqrt{x}}{\sqrt{1 - 3x + 2jx\sqrt{x}}}, \\ x \equiv GM/(rc^2). \end{gathered} \tag{41}$$

Here, r is the Boyer–Lindquist radial coordinate in the Kerr metric.

The expressions for j, E, and l corresponding to the marginally stable orbit, where the x coordinate is treated as a parameter, are

$$\begin{gathered} j_* = \frac{4\sqrt{x} - \sqrt{3 - 2x}}{3x}, \quad E_* = \sqrt{1 - \frac{2}{3}x}, \\ cl_*/GM - j_*E_* = \frac{1}{x\sqrt{3}}. \end{gathered} \tag{42}$$

The parameter x varies in the intervals (1/9, 1/6) and (1/6, 1) for disk and black-hole counterrotation and corotation, respectively. The corresponding values of j for the former interval are negative.

The disk energy release in the field of a black hole is obviously $\dot{M}c^2(1 - E_*)$. In order to express the energy release as a function of the black-hole angular velocity Ω, we use the formula [formula (12) in Christodolou and Ruffini (1971); see also Misner *et al.*

(1973), Sibgatullin (1984), Novikov and Frolov (1986)]

$$2\tilde{\Omega} = j/(1+\sqrt{1+j^2}), \quad \tilde{\Omega} \equiv \Omega MG/c^3.$$

Hence, it is easy to obtain

$$j = \frac{4\tilde{\Omega}}{(4\tilde{\Omega}^2+1)}. \tag{43}$$

Therefore, the energy release L_d in the disk around a Kerr black hole is a function of $\tilde{\Omega} = \Omega MG/c^3$ specified parametrically with $x = GM/rc^2$ (r is the Boyer–Lindquist coordinate radius of the marginally stable orbit). L_d has the following well-known values: $L_d = 0.0377\dot{M}c^2$ at $\tilde{\Omega} = -0.5$ ($j = -1$); $L_d = 0.0572\dot{M}c^2$ at $\tilde{\Omega} = 0$ ($j = 0$); and $L_d = 0.4226\dot{M}c^2$ at $\tilde{\Omega} = 0.5$ ($j = 1$). Note that $j = 1$ corresponds to a rotation frequency $f = c^3/(4\pi GM) \approx 11.56$ kHz for a black hole with $M = 1.4M_\odot$. The Taylor expansion of the energy release in the disk around a Kerr black hole in the interval $-0.4 \le \tilde{\Omega} \le 0.4$ ($-0.975 < j < 0.975$) is

$$L_d/\dot{M}c^2 \approx 0.0572 + 0.128\tilde{\Omega} + 0.349\tilde{\Omega}^2 + 0.532\tilde{\Omega}^3 + 0.52\tilde{\Omega}^4 + 0.417\tilde{\Omega}^5 + 0.65\tilde{\Omega}^6. \tag{44}$$

The function $L_d(\tilde{\Omega})/\dot{M}c^2$ is not analytic at $\tilde{\Omega} = 0.5$. Its expansion in terms of fractional powers of the difference $0.5 - \tilde{\Omega}$ is

$$L_d/\dot{M}c^2 \approx 0.4226 - 1.155(0.5-\tilde{\Omega})^{2/3} + 1.443(0.5-\tilde{\Omega})^{4/3} - 0.77(0.5-\tilde{\Omega})^{5/3} - 0.5(0.5-\tilde{\Omega})^2. \tag{44a}$$

The calculation using formula (44) at $\tilde{\Omega} = 0.4$ ($j \approx 0.975$) yields 0.2185; this value differs from that calculated by using formula (44a) and from the exact value by less than 0.0005. One should therefore use (44) for $|\tilde{\Omega}| < 0.4$ and the expansion (44a) for $0.4 < \tilde{\Omega} \le 1$. In the range $-0.5 < \tilde{\Omega} \le -0.4$, the first two terms in the Taylor expansion near $\tilde{\Omega} = -0.5$ ($j = -1$) can be used for the Kerr-disk luminosity:

$$L_d/\dot{M}c^2 \approx 0.0377 + 0.024(\tilde{\Omega}+0.5)^2.$$

Note that if the NS radius is smaller than the radius of the marginally stable orbit, then the energy release L_d in the disk around the NS is approximately equal to L_d in the disk around a black hole of the same mass and the same angular momentum. Indeed, we see from formula (45) for E_* that the corrections to the Kerr expression associated with powers of the quadrupole coefficient b are small.

Comparison of the Functions $j(\tilde{\Omega})$ for Black Holes and Neutron Stars. As the NS mass increases to its maximum value, when the star collapses in the static limit, the relationship between the dimensionless angular velocity of a NS with different equations of state and the Kerr parameter approaches the above relationship between these parameters for rotating black holes. Moreover, the NS external field differs only slightly from the gravitational field of a rotating black hole.

Indeed, using tables from Cook *et al.* (1994), we can construct approximations for the $M = 1.4M_\odot$ normal sequences in the static limit in the range $0 < j < 0.6$ [the function $j(\tilde{\Omega})$ is extended to negative $\tilde{\Omega}$ by using the oddness condition $j(\tilde{\Omega}) = -j(-\tilde{\Omega})$]:

EOS A $j \approx 6.573\tilde{\Omega} + 0.655(10\tilde{\Omega})^2$, $m = 1.566$;

EOS AU $j \approx 8.2\tilde{\Omega} + 0.65(10\tilde{\Omega})^2$, $m = 1.577$;

EOS FPS $j \approx 8.035\tilde{\Omega} + 0.91(10\tilde{\Omega})^2$, $m = 1.56$;

EOS L $j \approx 13.3\tilde{\Omega} + 3.03(10\tilde{\Omega})^2$, $m = 1.52$.

Let us now consider the functions $j(f)$ of maximum masses stable only in the presence of rotation:

EOS A $j \approx 4.066\tilde{\Omega} + 0.388(10\tilde{\Omega})^2$, $m = 1.92$;

$0 \le 10\tilde{\Omega} \le 0.84$;

EOS AU $j \approx 4.095\tilde{\Omega} + 0.14(10\tilde{\Omega})^2$, $m = 2.638$;

$0 \le 10\tilde{\Omega} \le 1.1$;

EOS FPS $j \approx 4\tilde{\Omega} + 0.445(10\tilde{\Omega})^2$, $m = 2.1$;

$0 \le 10\tilde{\Omega} \le 0.8$;

EOS L $j \approx 4.33\tilde{\Omega} + 0.34(10\tilde{\Omega})^2$, $m = 3.23$;

$0 \le 10\tilde{\Omega} \le 0.86$.

It follows from the above formulas that, for the maximum possible masses, the functions $j(\tilde{\Omega})$ of arbitrary NS equations of state are closely approximated by the dependence for Kerr black holes (43) at small $\tilde{\Omega}$: $j \approx 4\tilde{\Omega}$. At the same time, $j(\tilde{\Omega})$ for neutron stars with $M = 1.4M_\odot$ have $j(\tilde{\Omega}$ considerably exceed the Kerr values.

Parameters of the Marginally Stable Orbit in the Equatorial Plane in the Field of a Rotating NS. The external fields of rapidly rotating neutron stars differ markedly from the Kerr field. This difference can be described by introducing only one multipole moment, namely, the quadrupole one (Laarakkers and Poisson 1998; SS 98) at stellar masses larger than $M_\odot$. In general, the external gravitational fields at $M < M_\odot$ in the case of rapid rotation have all multipole components, much like the external field of a Maclaurin spheroid at a rotation velocity comparable in magnitude to the Keplerian velocity on the stellar equator.

In order to calculate the parameters of the marginally stable orbit, let us consider four quadrupole coefficients: $b = 0$, 0.25, 0.5, and 0.75. For each of these values, we break up the j range –0.7 to +0.7 into 30 equal parts and seek a minimum of the particle energy in circular orbits for each j [rather than seek the root of the complex equation (40), as we did in SS 98]. Having determined the corresponding radial coordinates, we can calculate all the remaining parameters of the marginally stable orbit and construct an approximating polynomial in j with the smallest rms deviation in the interval (–0.7, 0.7) at fixed b. We then construct an interpolation polynomial in b using Lagrange–Silvester's formula. Let us write out the functions (38) and (39) derived in this way, which, however, have a meaning only when the stellar radius is smaller than the radius of the marginally stable orbit. In the formulas given below, E_* has the meaning of binding energy of a particle of unit mass in the marginally stable orbit, and Ω_* is the angular velocity in this orbit:

$$\begin{aligned}E_* \equiv \min E &= 0.943 - 0.031j - 0.022j^2 - 0.014j^3\\ &- 0.01j^4 - 0.02j^5 - 0.02j^6 + b(0.008 + 0.017j\\ &+ 0.024j^2 + 0.016j^3 + 0.013j^4\\ &+ 0.085j^5 + 0.1j^6) + b^2(-0.002 - 0.01j\\ &- 0.021j^2 - 0.005j^3 - 0.002j^4\\ &- 0.14j^5 - 0.18j^6) + b^3(0.001 + 0.004j + 0.009j^2\\ &- 0.002j^3 - 0.004j^4 + 0.08j^4 + 0.11j^6);\end{aligned} \tag{45}$$

$$\begin{aligned}cl_*/(GM) &= 3.464 - 0.943j - 0.258j^2 - 0.125j^3\\ &- 0.074j^4 - 0.11j^5 - 0.09j^6 +\\ &+ b(0.189 + 0.226j + 0.244j^2 + 0.178j^3 + 0.15j^4\\ &+ 0.49j^5 + 0.51j^6) + b^2(-0.039 - 0.108j - 0.191j^2\\ &- 0.123j^3 - 0.123j^4 - 0.85j^5 - 0.96j^6)\\ &+ b^3(0.009 + 0.036j + 0.078j^2 + 0.034j^3\\ &+ 0.036j^4 + 0.5j^5 + 0.59j^6);\end{aligned} \tag{46}$$

$$\begin{aligned}R_*c^2/GM &= 6 - 3.267j - 0.278j^2 - 0.112j^3\\ &- 0.059j^4 - 0.07j^5 - 0.05j^6 + b(1.085 + 0.96j\\ &+ 0.904j^2 + 0.723j^3 + 0.177j^4\\ &+ 0.63j^5 + 1.53j^6) + b^2(-0.25 - 0.607j\\ &- 1.134j^2 - 1.107j^3 + 0.643j^4\\ &- 1.18j^5 - 4.89j^6) + b^3(0.059 + 0.223j\\ &+ 0.633j^2 + 0.604j^3 - 0.923j^4 + 0.71j^5 + 3.94j^6);\end{aligned} \tag{47}$$

$$\begin{aligned}\Omega_K^* GM/c^3 &= 0.068 + 0.051j + 0.037j^2 + 0.025j^3\\ &+ 0.017j^4 + 0.03j^5 + 0.03j^6\\ &+ b(-0.016 - 0.035j - 0.052j^2 - 0.039j^3\\ &- 0.033j^4 - 0.16j^5 - 0.18j^6)\\ &+ b^2(0.006 + 0.024j\\ &+ 0.053j^2 + 0.028j^3 + 0.014j^4 + 0.29j^5 + 0.37j^6)\\ &+ b^3(-0.002 - 0.01j - 0.025j^2 - 0.007j^3\\ &+ 0.008j^4 - 0.18j^5 - 0.24j^6).\end{aligned} \tag{48}$$

These formulas are universal and valid for any NS equation of state. If, alternatively, the dimensionless quadrupole coefficient $b = kj^2$ is expressed in terms of j and m for a specific equation of state (respectively, j and M), for example, by using formula (31), then we obtain the above formulas as functions of j and m (respectively, j and M). Formula (32) must be used for EOS A.

We emphasize that, in contrast to the Taylor expansions of Shibata and Sasaki (1998) for small j and $b \sim j^2$, formulas (45)–(48), which were derived from the exact solution by the combination of least squares and interpolation in b (Silvester–Lagrange's formula), describe the behavior of the solution in finite ranges: $b \le 0.75$ and $|j| \le 0.7$. Note that the corrections associated with the coefficient b ("non-Kerr behavior") in formula (45) for E_* are small.

Radial and Azimuthal Velocities on the NS Surface for the Particles Falling to the Stellar Equator from the Marginally Stable Orbit. The radial and azimuthal velocities of the particles that fell from the marginally stable orbit on the stellar surface in a local frame which is stationary relative to the orbits of Killing's timelike vector of the metric (21) are

$$\frac{V_\phi}{c} = \frac{f}{\sqrt{r}}(p_* + \omega_* - \omega),$$

$$\frac{V_r}{c} = \sqrt{1 - \frac{f^2}{r}(p_* + \omega_* - \omega)^2 - \left(1 - \frac{f_*^2 p_*^2}{r_*}\right)\frac{f}{f_*}}.$$

Here, the asterisk denotes the corresponding parameter in the marginally stable orbit. The approximations for V_ϕ and V_r for a NS with fixed mass $M = 1.4M_\odot$ and EOS A valid in the range $-1.2 < f < 0.88$ kHz are

$$\frac{V_\phi}{c} \approx 0.6 - 0.006(f/1\ \text{kHz}) - 0.04(f/1\ \text{kHz})^2,$$

$$\frac{V_r}{c} \approx 0.062 - 0.057(f/1\ \text{kHz}) - 0.015(f/1\ \text{kHz})^2.$$

and those for EOS FPS valid in the range $-1.0 < f < 0.6$ kHz are

$$\frac{V_\phi}{c} \approx 0.553 - 0.018(f/1\ \text{kHz}) - 0.052(f/1\ \text{kHz})^2,$$

$$\frac{V_r}{c} \approx 0.03 - 0.044(f/1\ \text{kHz}) - 0.03(f/1\ \text{kHz})^2.$$

In SS 98, we gave formulas for V_ϕ and V_r in a frame entrained by NS rotation. The corresponding approximations for $M = 1.4M_\odot$ for the azimuthal velocity are

$$\text{EOS A: } \frac{V_\phi}{c} \approx 0.6 - 0.035(f/1\ \text{kHz}) - 0.042(f/1\ \text{kHz})^2,$$

$$\text{EOS FPS: } \frac{V_\phi}{c} \approx 0.553 - 0.046(f/1\ \text{kHz}) - 0.055(f/1\ \text{kHz})^2.$$

The radial components of the 4-velocity do not change when passing from one frame to the other.

The kinetic energy of radial particle motion produces energy release in a shock wave near the equator, while the energy of azimuthal motion produces energy release in the spread layer that concentrates around two bright latitudinal rings (Inogamov and Sunyaev 1999). Clearly, this difference can, in principle, allow the case with a radius smaller than the radius of the marginally stable orbit $R < R^*$ (three bright rings) to be experimentally distinguished from the case with $R > R^*$ (two bright rings).

Since the particles in the gap are assumed to have no time to gather a high radial velocity for any reasonable f, $V_r \ll V_\phi$. Expanding the fourth tetrad 4-velocity component in a series yields

$$\frac{1}{\sqrt{1 - V_r^2/c^2 - V_\phi^2/c^2}} \approx \frac{1}{\sqrt{1 - V_\phi^2/c^2}} + \frac{V_r^2/c^2}{\sqrt{(1 - V_\phi^2/c^2)^3}}.$$

The flux of radial kinetic energy is therefore

$$L_{\text{rad}} \approx \dot{M}\frac{V_r^2/2}{\sqrt{(1 - V_\phi^2/c^2)^3}}.$$

The approximation of L_{rad} for a NS with the soft EOS A, where this flux reaches a maximum, is

$$L_{\text{rad}}/\dot{M}c^2 \approx 0.0035 - 0.01(f/1\ \text{kHz}) + 0.0025(f/f/1\ \text{kHz})^2 + 0.005(f/1\ \text{kHz})^3.$$

For the harder EOS FPS, the flux of radial energy is considerably lower,

$$L_{\text{rad}}/\dot{M}c^2 \approx 0.00026 - 0.003(f/1\ \text{kHz}) + 0.0036(f/1\ \text{kHz})^2 + 0.0035(f/1\ \text{kHz})^3.$$

The angular velocity of the particles falling from the marginally stable Keplerian orbit along helical trajectories is at a maximum on the NS surface. As follows from SS 98, the formula

$$f_s = \frac{p_* + \omega - \omega_*}{r/F^2 + \omega(p_* + \omega - \omega_*)}$$

holds for the particle angular velocity near the NS surface $f_s = d\phi/dt/2\pi$.

The approximations for f_s on the stellar surface and for f_K^* in the marginally stable orbit as functions of the NS rotation frequency are

$$\text{EOS A} \quad f_s/1\ \text{kHz} \approx 2.251 - 0.0236(f/1\ \text{kHz}) - 0.28(f/1\ \text{kHz})^2 + 0.062(f/1\ \text{kHz})^3;$$

$$f_K^*/1\ \text{kHz} \approx 1.575 + 0.421(f/1\ \text{kHz}) - 0.065(f/1\ \text{kHz})^2 - 0.016(f/1\ \text{kHz})^3;$$

$$\text{EOS FPS} \quad f_s/1\ \text{kHz} \approx 1.891 - 0.07(f/1\ \text{kHz}) - 0.224(f/1\ \text{kHz})^2 + 0.194(f/1\ \text{kHz})^3;$$

$$f_K^*/1\ \text{kHz} \approx 1.561 + 0.484(f/1\ \text{kHz}) - 0.081(f/1\ \text{kHz})^2 + 0.008(f/1\ \text{kHz})^3.$$

We emphasize that $f_s = f_K^*$ when $R = R_*$. The softer is the equation of state and the higher is the NS angular velocity when it counterrorates with the disk, the larger is the difference $f_s - f_K^*$. Thus, f_s specifies an additional characteristic frequency in the problem considered by Inogamov and Sunyaev (1999), which is appreciably higher than the rotation frequency of the matter in the bright latitudinal rings.

The NS Parameters at Which Its Equatorial Radius Is Equal to the Radius of the Marginally Stable Circular Orbit. In order to determine the NS parameters at which its equatorial radius is equal to the radius of the marginally stable circular orbit in the equatorial plane, we must solve the system of equations (19) and (20) in which the radius of the marginally stable orbit must be substituted for R. If we use formula (23) for the equatorial radius, which includes only one function $M(j, m)$ and its derivative with respect to m, then we obtain values that differ only slightly from those calculated using (19) and (20), within the accuracy of our calculation. In this case, however, we do not know the radial parameter ρ to approximate the functions expressed in terms of the metric coefficients.

Recall that the thermodynamic function $M(j, m)$ of its own corresponds to each equation of state [see expressions (15) and (17) for this function in the case of EOS A and EOS FPS].

We use formula (46) for the radius R_* in which the corresponding expressions [see formulas (31) and (32) for EOS FPS and EOS A, respectively must be substituted for the quadrupole coefficient $b = b(j, m)$. Thus, for each fixed j, we sought the corresponding solutions of the algebraic system (19) and (20) for m, $r \equiv \rho^2$. Using the Mathematica program, we can find a polynomial with the smallest rms deviation from the constructed points in the (j, m) plane and obtain the $m = \tilde{m}(j)$ curve that separates the equilibrium positions when the NS lies within its marginally stable circular orbit in the equatorial plane from the equilibrium positions with the NS lying outside this orbit.

The corresponding equations of the above curve in the (j, m) plane are

$$\tilde{m}(j) = 1.228 + 0.675j - 0.159j^2 + 0.104j^3 + 2.077j^4 + 1.25j^5 \quad (49)$$

for EOS A and

$$\tilde{m}(j) = 1.355 + 0.797j - 0.093j^2 - 0.343j^3 + 1.944j^4 + 2.86j^5 \quad (50)$$

for EOS FPS.

For EOS FPS in the (j, M) plane, the equation of the curve separating the states with the NS inside and outside R_* is (see Fig. 8)

$$\tilde{M}(j) \approx 1.259 + 0.575j - 0.109j^2 - 0.163j^3 + 0.94j^4 + 3.2j^5.$$

Parameters of Circular Orbits on the NS Equator at $R > R^*$ for EOS A. Let us introduce the parameters

$$d_m \equiv (\tilde{m}(j) - m)/(\tilde{m}(j) + 2jm),$$

$$d_M \equiv (\tilde{M}(j) - M)/(\tilde{M}(j) + 2jM).$$

These parameters are zero at $R = R_*$ and unity at $j = -0.5$. When d_m changes from 0 to 0.5, the $d_m(j, m) =$ const curves in the (j, m) plane fill the region $D = \{1.1 \geq m \geq 2.5\} \cap \{R \geq R_*\}$. Accordingly, when d_M changes from 0 to 0.5, the $d_M(j, M) =$ const curves in the (j, M) plane fill the region $D = \{1 \geq M \geq 2.1\} \cap \{R \geq R_*\}$. We therefore approximate the energy E, angular momentum l [calculated using (38)], and particle angular velocity f_K in a circular orbit lying on the stellar equator [calculated using (39)] in the region D by polynomials in j and d_m. For this purpose, we first approximate these functions at $d_m = 0$, 0.1, 0.2, and 0.3 by fourth-degree polynomials, finding the corresponding radial coordinates using Eq. (17), and then interpolate them in d_m (or d_M) using Silvester–Legendre's formula. Again using the Mathematica program, we obtain for EOS A

$$E = 0.943 - 0.029j + 0.019j^2 - 0.017j^3 - 0.074j^4 + d_m(0.002 - 0.001j + 0.031j^2 + 0.305j^3 + 0.416j^4) + d_m^2(0.097 + 0.398j + 0.072j^2 - 1.46j^3 - 1.56j^4) + d_m^3(-0.057 - 0.537j - 0.752j^2 + 1.712j^3 + 3.011j^4), \quad (51)$$

$$lc/(GM) = 3.463 - 0.909j + 0.661j^2 - 0.41j^3 - 1.373j^4 + d_m(0.028 + 0.076j + 1.18j^2 + 4.304j^3 + 3.95j^4) + d_m^2(1.418 + 5.279j + 0.318j^2 - 15.653j^3 - 13.44j^4) + d_m^3(0.855 - 3.047j - 14.241j^2 + 8.861j^3 + 35.58j^4), \quad (52)$$

$$f_K/1\ \text{кГц} = 1.972 + 0.466j - 1.226j^2 - 0.741j^3 + 2.746j^4 + d_m(-1.183 - 2.536j + 4.738j^2 - 0.986j^3 - 32.15j^4) + d_m^2(0.394 + 2.551j - 2.079j^2 + 22.97j^3 + 102.84j^4) + d_m^3(-0.993 - 1.237j + 13.343j^2 - 34.48j^3 - 169.05j^4). \quad (53)$$

Parameters of Circular Orbits on the NS Equator at $R > R^*$ for EOS FPS. For EOS FPS, we derive the following approximation formulas for the parameters of an equatorial Keplerian orbit using (38) and (39):

$$E = \tilde{E}(j) + d_m(0.01 - 0.02j - 0.294j^2 + 0.196j^3 + 1.586j^4) + d_m^2(0.026 + 0.537j + 2.775j^2 - 1.21j^3 - 11.039j^4) + d_m^3(0.103 - 0.874j - 7.258j^2 + 1.943j^3 + 27.516j^4) \approx \tilde{E}(j) + d_M(0.002 - 0.026j + 0.043j^2 + 0.131j^3 + 0.373j^4) + d_M^2(-0.105 + 0.748j - 1.184j^2 + 0.916j^3 + 2.726j^4) + d_M^3(-0.069 - 1.583j + 5.382j^2 - 6.883j^3 - 14.83j^4), \quad (54)$$

$$\tilde{E}(j) \approx 0.942 - 0.03j + 0.039j^2 - 0.011j^3 - 0.153j^4;$$

$$lc/(GM) = \tilde{l}(j) + d_m(0.049 - 0.147j + 0.237j^2 + 0.408j^3 + 4.79j^4) + d_m^2(1.306 + 5.733j + 5.272j^2 - 2.106j^3 - 3.207j^4) + d_m^3(0.743 - 3.434j - 23.054j^2 - 11.233j^3 + 32.45j^4) \approx \tilde{l}(j) + d_M(0.041 - 0.466j + 2.926j^2 - 1.619j^3 + 1.189j^4) \quad (55)$$

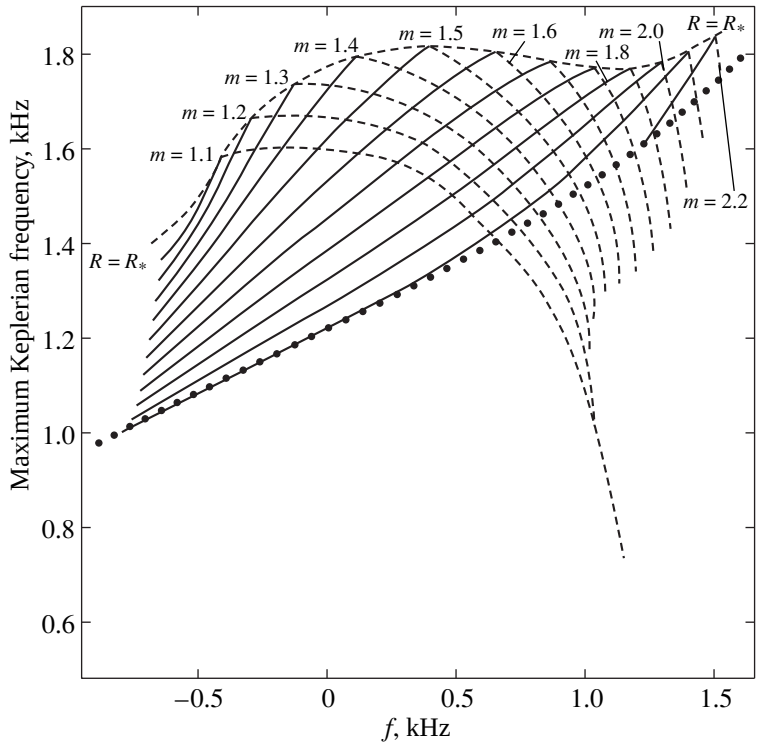

Fig. 10. Particle rotation frequency in the marginally stable circular Keplerian orbit at $R \le R_*$ (solid lines) and particle rotation frequency in an equatorial Keplerian orbit at $R \ge R_*$(dashed lines) versus NS rotation frequency for fixed rest masses m (EOS FPS). The upper envelope specifies the frequency for $R = R_*$; at m = const, the functions $f_K^*(f)$ monotonically increase for $R < R_*$, while the functions $f_K(f)$ monotonically decrease for $R > R_*$.

$$
\begin{aligned}
&+ d_M^2(1.604 + 12.501j - 42.641j^2 \\
&+ 63.336j^3 + 41.062j^4) + d_M^3(2.512 - 25.467j \\
&+ 182.594j^2 - 284.35j^3 - 202.93j^4), \\
&\tilde{l}(j) \approx 3.457 - 0.924j + 0.895j^2 - 0.375j^3 - 2.224j^4; \\
&\Omega_K GM/c^3 = \tilde{f}(j) + d_m(0.083 + 0.184j - 0.013j^2 \\
&- 0.087j^3 - 0.116j^4) + d_m^2(-1.013 - 2.31j - 0.268j^2 \\
&+ 1.116j^3 + 2.894j^4) + d_m^3(1.794 + 4.686j + 3.981j^2 \\
&- 2.428j^3 - 17.387j^4) \\
&\approx \tilde{f}(j) + d_M(-0.097 - 0.17j \\
&+ 0.071j^2 - 1.156j^3 - 2.302j^4) + d_M^2(-0.136 \\
&- 0.754j + 1.681j^2 + 11.715j^3 + 9.366j^4) \\
&+ d_M^3(0.614 + 3.075j - 5.577j^2 - 32.591j^3 - 13.9j^4), \\
&\tilde{f}(j) \approx 0.059 + 0.025j - 0.062j^2 - 0.017j^3 + 0.148j^4.
\end{aligned}
\tag{56}
$$

Here, $\Omega_K = 2\pi f_K$ is the particle angular velocity in the equatorial Keplerian orbit (in rad s^{-1}).

The Maximum Rotation Frequency in Circular Orbits at $R < R_*$ and $R > R_*$. The marginally stable orbits [see formula (48)] and the Keplerian orbits lying on the NS surface [see formulas (53) and (56)] have the largest frequency in Keplerian equatorial orbits around the NS at $R < R_*$ and $R > R_*$, respectively. We emphasize that we deal with circular orbits; for the spiraling-in particles in the gap between R_* and R, the angular velocities f_s are higher than those in the marginally stable orbit (see above). In order to interpret the quasi-periodic millisecond oscillations from LMXB objects, it is useful to calculate the dependence of the largest Keplerian frequency on the NS angular velocity; either (48) or (53) and (56) must be used, depending on the situation. In Fig. 10, maximum Keplerian frequency is plotted against NS rotation frequency for EOS FPS for fixed rest masses m at 0.1 steps. The NS angular velocity was calculated by using (9). The corresponding curves are indicated by solid and dashed lines at $R < R_*$ and $R > R_*$, respectively. The curve for $R = R_*$ is also indicated by a dashed line. When this curve is reached, the maximum possible Keplerian frequencies are obtained for a fixed rest mass. The dots indicate the curve of stability loss according to the static criterion;

it correspond to the $M = M_*(j)$ curve [$m = m_*(j)$] [see formulas (14) and (16)].

5. NS SPINUP VIA ACCRETION AND ITS LUMINOSITY

Spinup in the Newtonian Theory. Let us first consider the Newtonian pattern for an incompressible, self-gravitating rotating mass of fluid whose equilibrium figure is a MacLaurin spheroid.

The spheroid eccentricity e is defined as $e = \sqrt{1 - c^2/a^2}$. The Keplerian equatorial rotation frequency can be determined by equating the gravity and the centrifugal force:

$$f_K = \sqrt{G\rho/2\pi}B(e);$$
$$B(e) \equiv \sqrt{\frac{\sqrt{1-e^2}}{e^3}\arcsin e - \frac{1-e^2}{e^2}}. \quad (57)$$

The formula relating the angular frequency and the eccentricity of a Maclaurin spheroid follows, in particular, from equilibrium conditions:

$$f = \sqrt{G\rho g(e)/2\pi};$$
$$g(e) \equiv \frac{\sqrt{1-e^2}}{e^3}(3-2e^2)\arcsin e - 3\frac{1-e^2}{e^2}. \quad (58)$$

Denote the mass brought by the accreting particles from the disk to the stellar equator per unit time, which subsequently spreads over the star, changing its mass, angular momentum, and total energy in an equilibrium way, by $\dot{M}$. From the law of conservation of angular momentum, we have

$$\frac{d}{dt}If = \dot{M}a f_K. \quad (59)$$

We derive the following evolutionary equation for the eccentricity from formula (59) (see also Finn and Shapiro 1991):

$$\frac{de}{dt} = \frac{5\left(B(e) - \frac{2}{3}\sqrt{g(e)}\right)}{2\left(2e\sqrt{g(e)}/(3(1-e^2)) + \frac{d}{de}\sqrt{g(e)}\right)}\dot{M}/M. \quad (60)$$

When the disk and the Maclaurin spheroid counterrotate, the sign in Eq. (53) before $B(e)$ must be changed to the opposite one.

Let us introduce a dimensionless parameter of angular acceleration q:

$$q\dot{M}/M = \frac{df}{dt}\sqrt{\frac{2\pi}{G\rho}} = \frac{d\sqrt{g(e)}}{de}\frac{de}{dt}. \quad (61)$$

We substitute the right-hand part of (60) for de/dt.

The right-hand part of (61) can be expanded in a Taylor series in e by using (58). Passing to a Taylor expansion of q as a function of dimensionless angular velocity $\tilde{f} \equiv f\sqrt{2\pi/G\rho}$ or the ratio of the NS rotation frequency to the rotation frequency in an equatorial Keplerian orbit, we obtain

$$q \approx 2.0412 - 5/3\,\tilde{f} - 5.868\,\tilde{f}^2 + 25/6\,\tilde{f}^3$$
$$- 0.371\,\tilde{f}^4 + 0.744\,\tilde{f}^5 \approx 2.0412 - 1.3608\frac{f}{f_K}$$
$$- 3.9124\left(\frac{f}{f_K}\right)^2 + 2.6085\left(\frac{f}{f_K}\right)^3$$
$$+ 1.7911\left(\frac{f}{f_K}\right)^4 - 1.1941\left(\frac{f}{f_K}\right)^5. \quad (61a)$$

Note that formulas (61a) are also valid for negative f (counterrotation). The parameter of NS angular acceleration is determined solely by its density and angular velocity.

Spinup in General Relativity. In general relativity, the dimensionless parameter of angular acceleration q can be introduced as follows:

$$\frac{df}{dt} = \frac{c^3}{GM_\odot}\frac{\dot{M}}{M}q \text{ or } \frac{df/1\text{ kHz}}{dt} = 111.37\frac{\dot{M}}{M}q.$$

Using our results from SS 00, we can easily obtain for q in general relativity

$$q/M_\odot = \frac{lc/(G) - 2jMM_{,m}}{M + 2jM_{,j}}$$
$$\times\left(\frac{M_{,j}}{M(M+2jM_{,j})}\right) + \left(\frac{M_{,j}}{M(M+2jM_{,j})}\right)_{,m}M. \quad (62)$$

For slowly rotating stars ($j < 0.1$), the angular acceleration [as follows from (62)] is given by

$$q \approx \frac{M_\odot M_{,jj}}{M^2}. \quad (63)$$

At $M = 1.4M_\odot$, $q \approx 9.55$, 8.33, and 8.54 for EOS A, EOS AU, and EOS FPS, respectively. We emphasize that, here, we consider the instantaneous rate of change in the rotation frequency of a NS with a given gravitational mass and angular velocity rather than the evolution of NS parameters during accretion.

Below, we restrict ourselves to numerically constructed dependences for the EOS FPS alone.

The approximation formula for q in the case of NS and disk corotation at $M = 1.4M_\odot$ is

$$q \approx 10.964 - 6.057(f/1\text{ kHz}) + 1.54(f/1\text{ kHz})^2. \quad (64)$$

This formula is valid for angular velocities from 100 to 800 Hz. In the case of accretion-disk and NS counterrotation (when the NS spins down), the approxima-

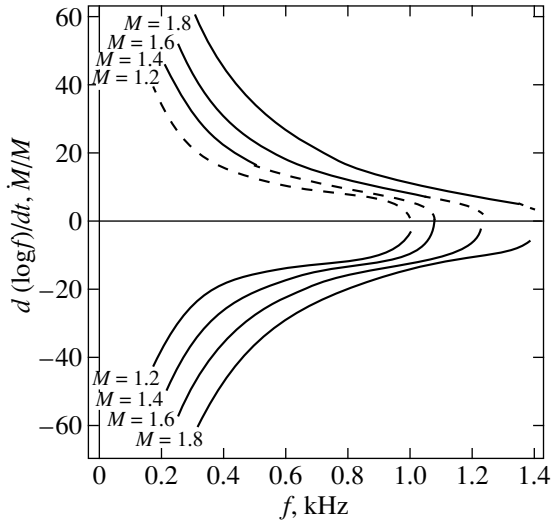

Fig. 11. Angular acceleration via disk accretion versus NS rotation frequency at $R \le R_*$ (solid lines) and at $R \ge R_*$ (dashed lines) for fixed gravitational masses M(EOS FPS) [see the approximation formulas (54)–(58) for $q(f)$ at the fixed gravitational masses $M = 1.4M_\odot$ and $M = 1.8M_\odot$]. The lower curves describes counterrotation (spindown). The upper curves describe spinup when the NS and the disk corotate.

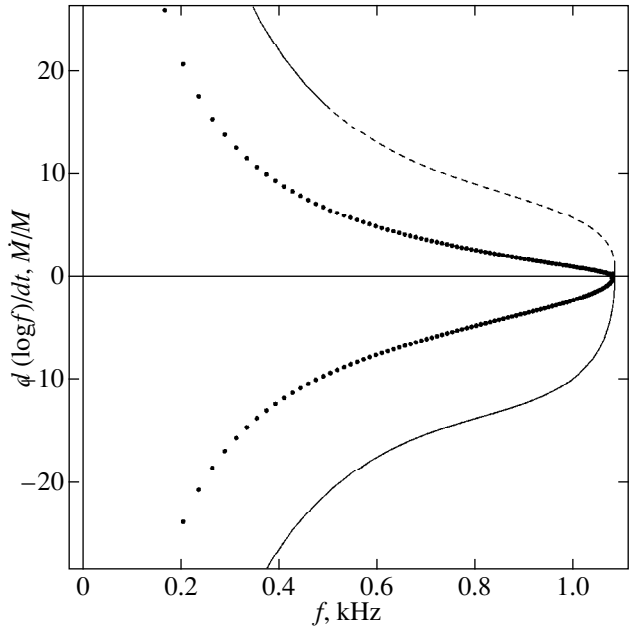

Fig. 12. Comparison of the plots of angular acceleration q versus NS rotation frequency for the fixed gravitational mass $M = 1.4M_\odot$ in general relativity (EOS FPS) (heavy line) and in the Newtonian theory (thin line) at matched maximum angular velocities.

tion formula for $|q|$ in the same range of angular velocities is

$$q \approx 10.565 - 2.4(|f|/1\ \text{kHz}) - 4.34(f/1\ \text{kHz})^2. \quad (65)$$

For $M = 1.8M_\odot$, an approximate formula for the parameter of angular acceleration q is

$$q \approx 22.234 - 9.664(f/1\ \text{kHz}) - 1.63(f/1\ \text{kHz})^2 \quad (66)$$

in the case of corotation and

$$q \approx 20.27 - 2.96(|f|/1\ \text{kHz}) - 2.59(|f|/1\ \text{kHz})^2 \quad (67)$$

in the case of counterrotation. These formulas are valid in the range of angular velocities from 150 to 1200 Hz.

Formulas (64)–(67) are slightly inaccurate for slow rotation. In this case, formula (63) must be used. The transition from corotation to counterrotation of the star and the disk in the exact statement (61)–(63) is smooth. In Fig. 11, 1 kHz q/f is plotted against f for fixed gravitational masses M = 1.2, 1.4, 1.6, and $1.8M_\odot$. For comparison, Fig. 12 shows the $(M/\dot{M})d\ln f/dt$ dependences in the Newtonian theory and in general relativity. The density ($\sim 10^{14}$ g cm^{-3}) was chosen in such a way that the maximum possible angular velocities were equal in both approaches.

Energy Release on the NS Surface During Disk Accretion for Weak Magnetic Fields. In Figs. 3 and 4, total energy release on the surface of a NS with EOS FPS and in the accretion disk (solid line), as well as the ratio of these energy releases (dashed line), are plotted against NS angular velocity for normal sequences with the fixed rest mass $m = 1.56M_\odot$ ($M = 1.4M_\odot$ in the static limit) and $m = 2.1M_\odot$ ($M = 1.8M_\odot$ in the static limit).

We derived formulas for the energy releases in SS 00:

$$L_s = \dot{M}c^2(E - \Omega l/c^2 - \mu), \quad L_d = \dot{M}c^2(1 - E) \ \text{ at } \ R \ge R_*; \quad (68)$$

$$L_s = \dot{M}c^2(E_* - \Omega l_*/c^2 - \mu), \quad L_d = \dot{M}c^2(1 - E_*) \ \text{ at } \ R \le R_*. \quad (69)$$

Here, μ is the NS chemical potential, and Ω is its angular velocity (see SS 00). The quantities in the formulas for the surface energy release are given by the following formulas: (9) for Ω; (19) for μ; (45), (46) for E_*, l_*; (51), (52) for EOS A; and (54), (55) for EOS FPS for E, l. In the case of a nonrotating NS, the formulas for gravitational energy release were derived by Sunyaev and Shakura (1986).

The energy release reaches a maximum when the disk and the neutron star counterrotate: for EOS FPS, it is $0.414\dot{M}c^2$ at $f = -1.08$ kHz for $m = 1.56M_\odot$ and $0.67\dot{M}c^2$ at $f = -1.49$ kHz for $m = 2.1M_\odot$.

Figures 1 and 2 show these quantities for the fixed gravitational masses $M = 1.4$ and $M = 1.8M_\odot$.

The maximum luminosity for the gravitational mass $M = 1.4M_\odot$ is $0.408\dot{M}c^2$ at $f = -1.08$ kHz. The approximations for the total luminosity and the $L_s/(L_s + L_d)$ ratio at $|f| \le 1$ kHz for the gravitational mass $M = 1.4\,M_\odot$ are given by formulas (1) and (2) in the Introduction.

The maximum luminosity for $M = 1.8M_\odot$ is $0.62\dot{M}c^2$ at $f = -1.41$ kHz. The approximation for the total luminosity at $|f| \le 1$ kHz for $M = 1.8M_\odot$ is

$$L_s + L_d \approx 0.333 - 0.193\,f/1\text{ kHz} + 0.006(f/1\text{ kHz})^2\dot{M}c^2. \quad (70)$$

If the f dependence of $L_s/(L_s + L_d)$ is approximated by a quadratic trinomial in the range $-1 < f < 1$ kHz at $M = 1.8M_\odot$, then we obtain

$$L_s/(L_s + L_d) \approx 0.83 - 0.17\,f/1\text{ kHz} - 0.1(f/1\text{ kHz})^2. \quad (71)$$

For comparison, we give approximations for $\epsilon_{grav} = (L_s + L_d)/M_\odot$, the efficiency of gravitational energy release on the surface of a NS with the soft EOS A and the moderate EOS AU, as functions of rotation frequency f for $M = 1.4M_\odot$ NS normal sequences in the static limit:

$$\text{EOS A: } \epsilon_{grav}/c^2 = 0.245 - 0.152\,f/1\text{ kHz} + 0.02(f/1\text{ kHz})^2, \quad (72)$$

$$L_s/(L_s + L_d) = 0.765 - 0.242\,f/1\text{ kHz} - 0.108(f/1\text{ kHz})^2, \quad |f| < 1.3\text{ kHz}; \quad (73)$$

$$\text{EOS AU: } \epsilon_{grav}/c^2 = 0.225 - 0.137\,f/1\text{ kHz} + 0.01(f/1\text{ kHz})^2, \quad (74)$$

$$L_s/(L_s + L_d) = 0.773 - 0.301\,f/1\text{ kHz} - 0.174(f/1\text{ kHz})^2, \quad |f| < 1\text{ kHz}. \quad (75)$$

The softer is the equation of state, the stronger is the concentration of matter toward the stellar center, and the larger is the gap between the marginally stable orbit and the NS surface. Therefore, the energy release on the surfaces of stars with a soft equation of state at the same masses and angular velocities exceeds the energy release on the surfaces of stars with a hard equation of state.

As follows from (1), (70), (72), and (74), the total energy release is a nearly linear function of the NS rotation frequency over a wide range of its variation, $|f| < 1$ kHz. This distinguishes the general-relativity results from the Newtonian theory of disk accretion onto Maclaurin spheroids (see below).

Estimating the Energy Release in the Newtonian Theory. When a rotating NS is modeled by a Maclaurin spheroid, the following formula holds for the total energy release in the disk and on the NS surface (ϕ_e is the gravitational potential at the equator):

$$\frac{L_s + L_d}{\dot{M}R^2} = \frac{1}{2}\left((\Omega_K - \Omega)^2 + 2\frac{\phi_e}{R^2} - \Omega_K^2\right) = \pi G\rho\left((B - \sqrt{g})^2 + 2\frac{(1-e^2)^{3/2}}{e^3}\arcsin e + 2 - 2e^2\right). \quad (76)$$

The notation (57) and (58) is used in (76). Expanding $B(e)$ and $g(e)$ in a Taylor series in powers of e and expressing e in terms of f $\tilde{f} \equiv f\sqrt{2\pi/G\rho}$ and f/f_K yield

$$\frac{L_s + L_d}{0.11\dot{M}c^2}\left(\frac{M}{1.4M_\odot}\right)^{-2/3}\left(\frac{\rho}{10^{14}\text{ g/cm}^3}\right)^{-1/3} \approx 1 - 1.2247\tilde{f} + 0.5\tilde{f}^2 - 1.0716\tilde{f}^3 + 0.3125\tilde{f}^4 - 1.608\tilde{f}^5 \approx 1 - \frac{f}{f_K} + \frac{1}{3}\left(\frac{f}{f_K}\right)^2 - \frac{1}{3}\left(\frac{f}{f_K}\right)^3 - \frac{1}{36}\left(\frac{f}{f_K}\right)^4 + \frac{1}{36}\left(\frac{f}{f_K}\right)^5. \quad (77)$$

The speed of light in (77) was introduced for convenience of comparing the energy releases in the Newtonian theory and in general relativity.

For the ratio of the energy release on the surface of a Maclaurin spheroid and the total energy release, we have an exact formula:

$$\frac{L_s}{(L_d + L_s)} = 0.5(1 - f/f_K). \quad (78)$$

Note that, in contrast to general relativity, the Newtonian theory underestimates the contribution of the surface luminosity to the total luminosity for slow rotation and counterrotation: compare formulas (77) with (2), (71), (73), and (75).

6. NEUTRON-STAR AND DISK COUNTERROTATION

The approach developed here allows the energy release during disk accretion to be calculated in the two most important cases where the star and the disk matter corotate and counterrotate. Unfortunately, the problem

with an arbitrary angle between the disk and NS rotation axes is much more complex.

As we see from the figures and the approximation formulas (1), (2), (70)–(75), when the directions of the rotation axes coincide, the surface energy release decreases in importance compared to the static case, while the disk energy release increases in importance. An important thing is that the gap between the disk and the NS disappears for rapid rotation in the same sense. The total energy release is appreciably smaller (by a factor of 1.55) than that for a nonrotating NS with the external geometry described by the Schwarzschild solution even at the observed rotation periods of bursters (of the order of 600 Hz). The L_d/L_s ratio is equal to unity at $f = 600$ Hz for EOS FPS and $M = 1.4M_\odot$.

Generally, counterrotation is of great interest. In this case, the total energy release during disk accretion abruptly increases, reaching the record $0.49\dot{M}c^2$ for an $1.4M_\odot$ star in the case of the most rapid counterrotation, and even reaches $0.67\dot{M}c^2$ for the maximum-mass normal sequence, which is unstable in the static limit for a NS with the soft EOS A. Note that this energy release exceeds appreciably the energy release of $0.422\dot{M}c^2$ in the disk during accretion onto a Kerr black hole with the maximum possible dimensionless angular momentum $j = 1$. Interestingly, by contrast to a Kerr black hole, the energy release during accretion onto a NS is at a maximum in the case of counterrotation. In section 5, we provide approximation formulas for the other two equations of state as well, showing that there is the same tendency for them. In general relativity, enhanced energy release is accompanied by a faster angular deceleration of the NS than in the Newtonian theory. As we see from Figs. 1–4 and the approximation formulas (24)–(28), there is a gap between the marginally stable orbit and the NS surface in the case of counterrotation almost for all equations of state.

We do not consider the detailed physics of the spread and boundary layers but discuss only the parameters of the marginally stable orbit disregarding other forces acting on the accreting particles, for example, light-pressure forces. Concurrently, the L_s/L_d ratio abruptly increases for counterrotation: much more energy is released on the NS surface than in the disk. Formulas (2), (71), (73), and (75) give simple approximations of $L_s/(L_s + L_d)$ for three characteristic NS equations of state as functions of stellar rotation frequency.

Nuclear and Gravitational Energy Release in X-ray Bursters. The most important parameter of X-ray bursters is the ratio of energy E_{nucl} released during a relatively short (5–20 s) X-ray burst (resulted from a nuclear explosion in the matter accreted onto the NS surface) to energy E_{grav} released via accretion in intervals between two successive explosions T. This energy release of the infalling matter is related to the release of gravitational energy. Explosions recur as nuclear fuel is accumulated and follow with a quasi-period from several hours to several days. Clearly,

$$\frac{E_{nucl}}{E_{grav}} = \frac{\int_{t_i}^{t_{burst}} L_{burst}dt}{\int_{t_i}^{t_i+T} L_{grav}dt} = \frac{\epsilon_{nucl}}{\epsilon_{grav}},$$

where ϵ_{nucl} is the efficiency of nuclear energy release, close to 1 MeV/nucleon $\approx 10^{-3}c^2$, for helium burning and its conversion into C^{12} and for the subsequent thermonuclear reactions up to the production of iron (Bildsten 2000). As we pointed out above, $\epsilon_{grav} = (L_s + L_d)/\dot{M}$ is a strong function of the NS angular velocity and its direction.

For a $1.4M_\odot$ star, the energy release ϵ_{grav} during accretion onto a NS is (depending on the equation of state): (1) $0.245c^2$ for EOS A, $0.217c^2$ for EOS AU, and $0.213c^2$ for EOS FPS in the case of a slowly rotating star; (2) $0.172c^2$ for EOS A, $0.145\ c^2$ for EOS AU, and $0.128c^2$ for EOS FPS in the case of corotation with a frequency of 600 Hz; and (3) $0.32c^2$ for EOS A, $0.311c^2$ for EOS AU, and $0.308c^2$ for EOS FPS in the case of counterrotation with a frequency of 600 Hz.

It is thus clear that allowance for rotation can account for the observed luminosity variations from source to source within a factor of 2–2.5.

In this case, only ϵ_{grav} varies; we assume ϵ_{nucl} to be independent of the stellar rotation and ignore the difference in the spectra of the disk and the stellar surface.

This simple argument indicates that $\epsilon_{grav}/\epsilon_{nucl}$ is relatively low for corotating objects. At the same time, the considerably rarer cases of counterrotation must result in abnormally high $\epsilon_{grav}/\epsilon_{nucl}$; this cannot affect the recurrence time of nuclear bursts, but appreciably reduces their amplitude. It is reflected only in an increase of the persistent flux between bursts. Such cases are observed. One should pay particular attention to such sources as objects in which the angle between the NS and disk rotation axes exceeds appreciably $\pi/2$.

Observational Differences between Corotating and Counterrotating Objects. The observational manifestations of accreting neutron stars must strongly depend on whether the NS and the disk corotate or counterrotate even at observed rotation frequencies of ~600 Hz. The most important difference is associated with the presence of a fairly extended gap between the disk and the NS when they counterrotate. This may give rise to an appreciable energy release in the equatorial boundary region, in addition to the two regions equidistant from the equator predicted by the theory of matter spread over the NS surface. At low accretion rates, a hard spectrum originating in a strong shock wave, in which the radial velocity is lost, can form in the equatorial region. Thus, the radial and azimuthal velocities determine the energy release in the equatorial region

and in the bright equidistant belts (Inogamov and Sunyaev 1999), respectively. At all the observed NS rotation frequencies, the energy release associated with the radial velocity (though it reaches 10–15% of the azimuthal velocity in the equatorial region on the NS surface) is incapable of significantly affecting the dynamics of the infalling gas, because it cannot compensate for the difference between the gravity and the centrifugal force for the infalling particles near the NS surface. The presence of a gap at low accretion rates allows us to record photons from the lower NS hemisphere, which is completely hidden by the disk from the observer in the case of corotation where there is no gap. However, the main thing is that the surface luminosity greatly exceeds the luminosity in the accretion disk when the L_s/L_d ratio reaches 5 or 6 for counterrotation of an $M = 1.4M_\odot$ star with a frequency of 600 Hz. Note that, when the star cororates and has a rotation frequency of 600 Hz, the disk luminosity is approximately the same as that of the entire NS surface. This case is much closer to the case of accretion onto a black hole (where there is no solid surface at all) than the case of counterrotation.

Why Might We Expect the Existence of Accretion Disks around Counterrotating Stars? In the standard pattern of NS spinup by the accreting matter, all stars must eventually corotate with the accretion disk. Nevertheless, nature allows for the formation of counterrotating low-mass star and disk.

(1) Imagine a binary produced by an explosion of the more massive component turning into a NS. The kick during an asymmetric explosion, which is widely discussed in the literature, must result not only in a high velocity of the formed NS but also in its appreciable rotation (Spruit and Phinney 1998). In this case, it is doubtful that the sense of rotation resulting from the kick coincides with the sense of rotation of the disk, which is determined by the direction of the binary's orbital angular momentum. The circularization time of a close binary's orbit must be appreciably shorter than the time of change in the NS rotation axis.

(2) Tens of millisecond pulsars are observed in rich globular clusters, and there may be many hundreds of binaries containing neutron stars with weak magnetic fields. A change of the low-mass partner in such a binary during a close encounter with a single star (see McMillan and Hut 1996) can, in principle, give rise to a binary with NS and disk counterrotation. The ejection of such a binary from the globular cluster by tidal forces when the cluster traverses the central part of the Galaxy (or through the interaction of close pairs inside the globular cluster) can give rise to binaries with NS and disk counterrotation outside these clusters.

(3) If a rapidly rotating neutron star with a weak magnetic field is born during gravitational collapse in a massive binary, then accretion of the high-speed stellar wind emitted by a massive, hot supergiant takes place. Illarionov and Sunyaev (1974) pointed out that, in this case, an accretion disk can form around the NS, but the sense of rotation of the disk can depend on density and velocity fluctuations of the matter near the capture radius. Clearly, the transition from states close to NS and disk corotation to states with an appreciable angle between the NS and disk rotation axes must be accompanied by a radical change in the effective energy release and spectrum. If a counterrotating disk is formed in this case, then surface nuclear explosions are much more difficult to observe in such a binary because of the low $\epsilon_{nucl}/\epsilon_{grav}$ ratio, which may hamper the binary's identification as an X-ray burster. Such a binary may turn out to be similar in many ways to 4U 1700–37, from which no regular X-ray pulsations are observed (there is no strong magnetic field) and from which (although the X-ray emission is erratic) no X-ray bursts of the first type (coupled with surface nuclear explosions) have been observed so far.

DISCUSSION

Rapid rotation of accreting neutron stars is widely discussed in the literature devoted to interpretation of the nature of kilohertz quasi-periodic X-ray oscillations from low-mass X-ray binaries (Van der Klis 2000; Wijnands and Van der Klis 1997; Miller *et al.* 1998; Stromayer *et al.* 1998; Titarchuk and Osherovich 1998). The kilohertz quasi-periodic oscillations were discovered from the RXTE satellite.

For neutron stars rotating with periods of 300–600 Hz, the NS rotation affects significantly its internal structure and external field. Hartle and Sharp (1967) (see also Hartle 1978) developed a variational principle for rotating barotropic stars.

Numerical calculation of a rapidly rotating star with a polytropic equation of state, calculation of differential rotation, and the case of piecewise constant polytropic indices (as the asymptotics of the equations of state for stellar matter at temperatures below the degeneracy temperature; see Eriguchi and Mueller 1985) for large angular velocities present series computational difficulties even in the Newtonian approximation. These difficulties have been overcome only relatively recently (see Ostriker and Mark 1968; Tassoul 1978; Hachisu 1986). In general relativity, there are several numerical algorithms (codes) for finding steady-state configurations of rotating gas masses in their gravitational fields: Butterworth–Ipser's (1976) method, Friedman *et al.*'s (1986) modification of this method, the KEH method (Komatsu *et al.* 1989), Cook *et al.*'s (1994) modification of this method (see also Stergioulas and Friedman 1995), and the BGSM code based on spectral methods (Bonazzola *et al.* 1993; see Eriguchi *et al.* 1994 for a comparison of different approaches; Nozawa *et al.* 1998). Friedman *et al.* (1986) first published calculations of steady-state configurations of rapidly rotating neutron stars using realistic tabulated equations of state. Previously, Butterworth and Ipser (1976) and Bonazzola and Schneider (1974) used polytropic mod-

els and an incompressible fluid model. Many important physical parameters of the NS external field for 14 equations of state (including detailed tables of sequences with a fixed rest mass for EOS A, AU, FPS, M, and L) are contained in Cook *et al.* (1994). Based on the BGSM code, Salgado *et al.* (1994) analyzed the global parameters of neutron stars with different equations of state.

Datta *et al.* (1998) gave tables of NS parameters at fixed NS angular velocity and central density for EOS A, B, C, D, E, F, and the new equations of state BBB1, BBB2, BPAL21, and BPAL32. Based on the KEH method, Stergioulas (1998) developed a numerical code for computing the global parameters of neutron stars with many known equations of state. This code computes the NS properties as functions of two parameters: one is the central density, and the other can be either the rest mass or the gravitational mass, or the angular momentum, or the angular velocity. We repeatedly used this code in our calculations, which allowed us to construct the above approximation formulas.

As was already pointed out above, the gravitational fields of rotating gas configurations are essentially nonspherical at large angular velocities (Chandrasekhar 1986); all multipole components [as, for example, on the surface of a Maclaurin spheroid; see formulas (76)–(78)] contribute to the gravitational field near them.

Approximate and exact analytic solutions of the Einstein equations in a vacuum which approximate the numerical results obtained by the above authors are of considerable interest in describing the physical processes in strong external gravitational fields.

This problem was independently considered by several authors in 1998. Based on the numerical results of Cook *et al.* (1994), Laarakkers and Poisson (1998) analyzed the dependence of the quadrupole coefficient [which emerges in the expansion of the metric potential ν in the form of Bardeen and Wagoner (1971) at large radii] on Kerr parameter j. Laarakkers and Poisson (1998) pointed out that, in contrast to the nonrelativistic case, this dependence can be approximated by a parabolic law for the equations of state they considered.

Shibata and Sasaki (1998) used Fodor *et al.*'s (1989) asymptotic expansions of the function $\xi = \sqrt{\rho^2 + z^2}\,(1 - \mathbf{E})/(1 + \mathbf{E})$ (here, $\mathbf{E}$ is the Ernst complex potential; ρ and z are Weil's canonic coordinates) in the equatorial plane and on the symmetry axis to determine the radius of the marginally stable orbit and the particle angular velocity in this orbit in the form of formal expansions in powers of the dimensionless angular momentum j. The coefficients of these expansions were expressed in terms of Geroch–Hansen's multipole coefficients (see Hansen 1974), relative to which their order by j was assumed.

The marginally stable orbit is of considerable importance in interpreting the kilohertz QPOs detected by the RXTE satellite. Therefore, based on the numerical results of Cook *et al.* (1998), Miller *et al.* (1998) analyzed the dependences of the radius and angular velocity in the marginally stable orbit, as well as the equatorial radius, on the NS angular velocity for various equations of state of neutron matter.

Independently, Thampan and Datta (1998) also numerically analyzed the dependence of the Keplerian angular velocity in the marginally stable orbit on the NS angular velocity. When calculating the luminosity from the equatorial boundary layer, these authors assumed that the accreting particles radiated away all the energy equal to the difference between the energy in a Keplerian orbit and the energy of the particle corotating with the star on its equator. This assumption differs radically from our treatment in SS 98, SS 00, and this paper.

When the inverse effect of the spreading matter is considered on long time scales, the structural changes in the neutron star caused by the changes in its mass and angular momentum through their influx during accretion must be take into account. In their calculations of NS spinup via disk accretion, Lipunov and Postnov (1984) and Kluzniak and Wagoner (1985) assumed the moment of inertia to be equal to that of a nonrotating star and the rotation velocities to be low enough.

Burderi *et al.* (1998) made an attempt to describe the evolution of the NS angular velocity under the effect of disk accretion by using the Kerr metric for the NS external field. These authors also used approximation formulas for the gravitational mass of the type $M = m(1 - \alpha/R)$, $MR^3 = \text{const}$ (here, m is the NS rest mass) and extrapolated the formula of Ravenhall and Pethick (1994) for the moment of inertia in the static case to the case of rapid rotation; they postulated a relationship between the equatorial radius and the angular velocity, expressions for the maximum radius and the maximum angular velocity, etc.

Our approach (SS 00 and this paper) assumes that the luminosity from the stellar surface is considered on the basis of the first law of thermodynamics by taking into account changes in the NS total energy during quasi-uniform changes in its parameters under the effect of disk accretion. In the Newtonian problem, the energy release is proportional to the square of the Keplerian velocity on the NS equator relative to the frame of reference corotating with the star. This idea was generalized to the case of general relativity. In the absence of a magnetic field and for a constant entropy, the energy release takes place only in an extended disk and on the surface of a cool star.

In order to accurately describe the external field of a rotating neutron star, we proposed (SS 98) to use exact solutions of the Einstein equations in a vacuum, for which the Ernst complex potential on the symmetry axis has a simple structure with arbitrary constants that have the meaning of multipole coefficients. The exact quadrupole solution accurately describes the external fields of rapidly rotating neutron stars, and, by contrast to asymptotic expansions in inverse powers of the radius, is meaningful up to the stellar surface. Note that

expanding our solution in inverse powers of the radius in the equatorial plane yields a result that differs from the result of Shibata and Sasaki (1998) by terms of the order of j^4, because their assumption about the order of Geroch–Hansen's multipole coefficient Q_4 breaks down in our exact solution. Note that in SS98 [see formulas (11) and (12)], we calculated the radial and tangential velocities of accreting particles on the NS surface.

As the NS rest mass approaches the largest mass which is stable only in the presence of rotation, the quadrupole coefficient decreases, and the NS external gravitational field differs only slightly from the gravitational field of a rotating black hole (Kerr solution).

CONCLUSION

The method developed here and based on the static criterion for stability has allowed us to construct approximation formulas for the NS mass and its quadrupole coefficient as functions of its rotation parameter j and rest mass m. Using these functions and their partial derivatives, we determined all the remaining global NS characteristics: angular velocity, moment of inertia, equatorial radius, external gravitational field, parameters of the marginally stable orbit at $R < R_*$, and parameters of an equatorial Keplerian orbit at $R > R_*$ as functions of j and m or as functions of j and $M_\odot$. To this end, we used the thermodynamic ideas developed in SS 00. To describe the external field of a NS, we used an exact solution of the Einstein equations with an additional constant compared to the Kerr solution, which has the meaning of quadrupole coefficient. In the parameter plane, we found the curves that separate the states with a NS inside and outside the marginally stable orbit, as well as the neutral curves of stability loss according to the static criterion.

The inferred parameters enabled us to calculate (i) the energy release in the disk and on the NS surface in the presence and absence of a marginally stable orbit, (ii) the tetrad velocity components and the particle angular velocity on the NS surface on which they fell from the marginally stable orbit, and (iii) the spinup (spindown) rate as a function of the NS rest mass (or gravitational mass) and rotation frequency. We provided the corresponding approximation formulas for several equations of state at $M = 1.4M_\odot$.

In the Newtonian formulation (when the stellar matter is modeled by an incompressible fluid), the surface energy release and the spindown rate are given in the form of Taylor expansions in terms of the dimensionless rotation frequency for an arbitrary NS mass.

Using the property of the solution for the external gravitational field to belong to the class of solutions for two coaxially rotating black holes or Kerr disks, we hypothesize that the NS stability to the "quadrupole" oscillation mode is lost at the critical quadrupole moment $b = 0.25(1 - j^2)$.

ACKNOWLEDGMENTS

We wish to thank N. Stergioulas for his numerical code and R. Vilebinskii and N. Inogamov for a discussion.

REFERENCES

1. M. A. Alpar, A. F. Cheng, M. A. Ruderman, and J. Shaham, Nature **300**, 728 (1982).
2. W. D. Arnett and R. L. Bowers, Astrophys. J., Suppl. Ser. **33**, 415 (1977).
3. J. M. Bardeen, W. H. Press, and S. A. Teukolsky, Astrophys. J. **178**, 347 (1972).
4. J. M. Bardeen and R. V. Wagoner, Astrophys. J. **167**, 359 (1971).
5. G. Biehle and R. D. Blanford, Astrophys. J. **411**, 302 (1993).
6. L. Bildsten, astro-ph/0001135.
7. G. S. Bisnovatyĭ-Kogan and S. I. Blinnikov, Astron. Astrophys. **31**, 391 (1974).
8. G. S. Bisnovatyĭ-Kogan and B. V. Komberg, Astron. Zh. **51**, 373 (1974) [Sov. Astron. **18**, 217 (1974)].
9. S. Bonazzola, E. Gourgoulhon, M. Salgado, and J. A. Marck, Astron. Astrophys. **278**, 421 (1993).
10. S. Bonazzola and J. Schneider, Astrophys. J. **191**, 273 (1974).
11. L. Burderi, A. Possenti, M. Colpi, *et al.*, astro-ph/9904331.
12. I. M. Butterworth and J. R. Ipser, Astrophys. J. **204**, 200 (1976).
13. G. Calamai, Astrophys. Space Sci. **8**, 53 (1970).
14. F. Camilo, D. R. Lorimer, P. Freire, *et al.*, Astrophys. J. **535**, 975 (2000); astro-ph/9911234.
15. D. Chakrabarty and E. H. Morgan, Nature **394**, 346 (1998).
16. S. Chandrasekhar, *Ellipsoidal Figures of Equilibrium* (Dover, New-York, 1986).
17. D. Christodolou and R. Ruffini, Phys. Rev. **4**, 3552 (1973).
18. G. B. Cook, S. L. Shapiro, and S. A. Teukolsky, Astrophys. J. **424**, 823 (1994).
19. B. Datta, A. V. Thampan, and I. Bombaci, Astron. Astrophys. **334**, 943 (1998); astro-ph/9801312.
20. N. A. Dmitriev and S. A. Kholin, Vopr. Kosmog. **9**, 254 (1963).
21. K. Ebisawa, K. Mitsuda, and T. Hanawa, Astrophys. J. **367**, 213 (1991).
22. Y. Eriguchi and E. Mueller, Astron. Asrophys. **146**, 260 (1985).
23. Y. Eriguchi, I. Hachisu, and K. Nomoto, Mon. Not. R. Astron. Soc. **266**, 179 (1994).
24. F. J. Ernst, Phys. Rev. D. **50**, 4993 (1994).
25. L. S. Finn and S. Shapiro, Astrophys. J. **359**, 444 (1990).
26. G. Fodor, C. Hoenselaers, and Z. Perjes, J. Math. Phys. **30**, 2252 (1989).
27. B. Friedman and V. R. Pandharipande, Nucl. Phys. A **361**, 502 (1981).
28. J. F. Friedman, J. R. Ipser, and L. Parker, Astrophys. J. **304**, 115 (1986).
29. M. Gilfanov, M. Revnivtsev, R. Sunyaev, and E. Churazov, Astron. Astrophys. **339**, 483 (1998).

30. I. Hachisu, Astrophys. J., Suppl. Ser. **61**, 479 (1986).
31. I. Hachisu, Y. Eriguchi, and D. Sugimoto, Prog. Theor. Phys. **68**, 191 (1982).
32. R. O. Hansen, J. Math. Phys. **15** (1), 46 (1974).
33. J. B. Hartle, Phys. Rep. **46**, 202 (1978).
34. J. B. Hartle and D. H. Sharp, Astrophys. J. **147**, 317 (1967).
35. J. B. Hartle, Astrophys. J. **195**, 203 (1975).
36. J. B. Hartle and K. S. Thorne, Astrophys. J. **158**, 719 (1969).
37. C. Hoenselaers, Prog. Theor. Phys. **72**, 761 (1984).
38. A. F. Illarionov and R. A. Sunyaev, Astron. Zh. **51**, 1162 (1974) [Sov. Astron. **18**, 691 (1974)].
39. N. A. Inogamov and R. A. Sunyaev, Pis'ma Astron. Zh. **25**, 323 (1999) [Astron. Lett. **25**, 269 (1999)].
40. W. Kley, Astron. Astrophys. **247**, 95 (1991).
41. W. Kluzniak, Ph.D. Thesis (Stanford Univ., 1987).
42. W. Kluzniak and R. V. Wagoner, Astrophys. J. **297**, 548 (1985).
43. H. Komatsu, Y. Eriguchi, and I. Hachisu, Mon. Not. R. Astron. Soc. **237**, 355 (1989).
44. D. Kramer and G. Neugebauer, Phys. Lett. A**75**, 259 (1980).
45. W. Laarakkers and E. Poisson, gr-qc/9709033.
46. M. J. Lighthill, Mon. Not. R. Astron. Soc. **110**, 339 (1950).
47. L. Lindblom, Phys. Rev. D **58**, 024008 (1998); gr-qc/9802072.
48. V. M. Lipunov and K. A. Postnov, Astrophys. Space Sci. **106**, 103 (1984).
49. C. P. Lorenz, D. G. Ravenhall, and C. J. Pethick, Phys. Rev. Lett. **70**, 379 (1993).
50. V. S. Manko, E. W. Mielke, and J. D. Sanabria-Gómez, Phys. Rev. D **61**, 081501 (2000); gr-qc/0001081.
51. V. S. Manko, J. Martín, E. Ruíz, *et al.*, Phys. Rev. D **49**, 5144 (1994).
52. V. S. Manko and E. Ruíz, Class. Quantum. Grav. **15**, 2007 (1998).
53. D. Markovic and F. K. Lamb, *Rossi2000: Astrophysics with the Rossi X-ray Timing Explorer* (NASA's Goddard Space Flight Center, Greenbelt, 2000), p. E61.
54. S. L. W. McMillan and P. Hut, Astrophys. J. **467**, 348 (1996).
55. M. C. Miller and F. K. Lamb, Astrophys. J. **470**, 1033 (1996).
56. M. C. Miller, F. K. Lamb, and G. B. Cook, Astrophys. J. **509**, 793 (1998); astro-ph/9805007.
57. Ch. W. Misner, K. S. Thorne, and J. A. Wheeler, *Gravitation* (Freeman, New York, 1973).
58. G. Neugebauer, J. Phys. **13**, L19 (1980).
59. I. D. Novikov and V. P. Frolov, *Physics of Black Holes* (Nauka, Moscow, 1986).
60. T. Nozawa, N. Stergioulas, E. Gourgoulhon, and Y. Eriguchi, Astron. Astrophys. **132**, 431N (1998); gr-qc/9804048.
61. J. P. Ostriker and J. W.-K. Mark, Astrophys. J. **151**, 1075 (1968).
62. V. R. Pandharipande, Nucl. Phys. A **174**, 641 (1971).
63. R. Popham and R. Narayan, Astrophys. J. **442**, 337 (1995).
64. P. Popham and R. Sunyaev, astro-ph/0004017.
65. J. E. Pringle and M. J. Rees, Astron. Astrophys. **21**, 1 (1972).
66. W. H. Ramsey, Mon. Not. R. Astron. Soc. **110**, 325 (1950).
67. D. G. Ravenhall and C. J. Pethick, Astrophys. J. **424**, 846 (1994).
68. R. Ruffini and J. A. Wheeler, Bull. Am. Phys. Soc. **15** (11), 76 (1970).
69. F. D. Ryan, Phys. Rev. D **52**, 5707 (1995).
70. F. D. Ryan, Phys. Rev. D **55**, 6081 (1997).
71. M. Salgado, S. Bonazzola, E. Gourgulhon, and P. Haensel, Astron. Astrophys. **291**, 155 (1994).
72. Z. F. Seidov, Astron. Zh. **48**, 443 (1971) [Sov. Astron. **15**, 347 (1971)].
73. N. I. Shakura and R. A. Sunyaev, Adv. Space Res. **8** (2-3), 135 (1988).
74. S. L. Shapiro and S. A. Teukolsky, *Black Holes, White Dwarfs, and Neutron Stars: the Physics of Compact Objects* (Wiley, New York, 1983; Mir, Moscow, 1985).
75. M. Shibata and M. Sasaki, Phys. Rev. D **58**, 104011 (1998); gr-qc/9807046.
76. N. R. Sibgatullin, *Oscillations and Waves in Strong Gravitational and Electromagnetic Fields* (Nauka, Moscow, 1984; Springer-Verlag, Berlin, 1991).
77. N. R. Sibgatullin and R. A. Sunyaev, Pis'ma Astron. Zh. **24**, 894 (1998) [Astron. Lett. **24**, 774 (1998)]; astro-ph/9811028.
78. N. R. Sibgatullin and R. A. Sunyaev, Pis'ma Astron. Zh. **26** (2000) [Astron. Lett. (2000) (in press)].
79. H. C. Spruit and E. S. Phinney, Nature **393**, 139 (1998).
80. N. Stergioulas, http://pauli.phys.uwm.edu/Code/rns; www.livingreviews.org/ Articles/Volume1/1998-8stergio.
81. N. Stergioulas and J. L. Friedman, Astrophys. J. **444**, 306 (1995).
82. T. Stromayer, W. Zhang, J. H. Swank, *et al.*, Astrophys. J. Lett. **498**, L135 (1998); astro-ph/03119.
83. R. A. Sunyaev and N. I. Shakura, Pis'ma Astron. Zh. **12**, 286 (1986) [Sov. Astron. Lett. **12**, 117 (1986)].
84. J. L. Tassoul, *Theory of Rotating Stars* (Princeton Univ. Press, Princeton, 1978).
85. A. Thampan and B. Datta, Mon. Not. R. Astron. Soc. **297**, 570 (1998).
86. S. E. Thorsett and D. Chakrabarty, Astrophys. J. **512**, 288 (1999); astro-ph/9803260.
87. L. Titarchuk and V. Osherovich, astro-ph/0005375.
88. M. van der Klis, astro-ph/0001167.
89. R. A. D. Wijnands and M. van der Klis, Astrophys. J. Lett. **482**, L65 (1997).
90. R. B. Wiringa, V. Fiks, and A. Fabroccini, Phys. Rev. C **38**, 1010 (1988).
91. M. N. Zaripov, N. R. Sibgatullin, and A. Chamorro, Prikl. Mat. Mekh. **59** (5), 750 (1995).
92. M. N. Zaripov, N. R. Sibgatullin, and A. Chamorro, Vestn. Mosk. Univ., Ser. 1: Mat., Mekh., No. 6, 61 (1994).
93. Ya. B. Zel'dovich, Vopr. Kosmog. **9**, 157 (1963).
94. Ya. B. Zel'dovich and I. D. Novikov, *The Theory of Gravitation and Evolution of Stars* (Nauka, Moscow, 1971).

Translated by V. Astakhov

Astronomy Letters, Vol. 26, No. 11, 2000, pp. 725–729. Translated from Pis'ma v Astronomicheskiĭ Zhurnal, Vol. 26, No. 11, 2000, pp. 842–847.

A Preliminary Version of a Catalog of High-Low-Mass X-ray Binaries

O. H. Guseĭnov[1]*, A. T. Sayagac[2], A. Allakhverdiev[1], H. Caliskan[2], S. Ozdemir[3], S. K. Yerli[4], and A. Ankay[4]

[1] *University of Akdeniz, Faculty of Science and Education, Department of Physics, Antalya, Turkey*
[2] *University of Istanbul, Faculty of Science, Department of Astronomy and Space Sciences, Istanbul, Turkey*
[3] *Ankara University, Department of Astronomy and Space Science, Ankara, Turkey*
[4] *Middle East Technical University, Department of Physics, Ankara, 06531 Turkey*

Received October 1, 1999; in final form, December 27, 1999

Abstract—We introduce a catalogue of X-ray binaries. The full catalogue is available at http://astroa.physics.metu.edu.tr/XRBC/. The aim of this catalogue is to provide basic information about X-ray sources and their counterparts. The catalog contains positions, information about distances and counterparts, spectral, photometric and timing properties of the X-ray sources in the X-ray and optical bands, as well as references. The list of references, comments and the catalog as a whole will be periodically updated to include the most up-to-date information about all X-ray binaries and guide users to the recent literature on individual sources. In some cases, there is some doubt about the nature of an X-ray source, which has been noted. The sources are ordered according to right ascension. Here, we present a guide to the organization of the full catalogue. The full catalogue is represented here with an excerpt containing two HMXBs and two LMXBs as examples. *© 2000 MAIK "Nauka/Interperiodica".*

Key words: *catalogs, X-ray binaries, neutron stars, X-rays*

INTRODUCTION

The discovery of the first point X-ray source Sco X-1 (Giacconi *et al.* 1963) outside the solar system was a surprise, because the only previously known stellar X-ray emission, that of the solar corona, did not lead to an expectation of bright point X-ray sources. The general properties of point X-ray sources in the Galaxy were understood in terms of accretion onto compact objects (Zel'dovich and Guseinov 1965; Shklovskii 1967; Guseinov 1970) just before the first UHURU satellite sky survey in 1971. The results of the UHURU sky survey (Forman *et al.* 1978) were followed by publications from various rocket and satellite observations (Ariel V sky survey, McHardy *et al.* 1981; Warwick *et al.* 1981; MIT OSO-7, Markert *et al.* 1979; HEAO A-1 sky survey, Wood *et al.* 1984), and catalogs were compiled to bring together data from different experiments (Amnuel *et al.* 1979, 1982).

The first X-ray transient (nova) Cen X-2 was discovered from a rocket (Harries 1967). The first X-ray pulsar Cen X-3 was observed in 1971 (Giacconi *et al.* 1971; Schreier 1972). The first burster LMXB 1820-303 was discovered in 1976 (Grindlay *et al.* 1976); Cyg X-1 was discovered in 1965 and discussed as a black-hole candidate in 1972. The first quasi-periodic oscillation (QPO) behavior was also noted from Cyg X-1 (Frontera and Fuligni 1975). The classic QPO phenomenon from LMXBs was first discovered by Van der Klis *et al.* (1985) from the source LMXB 1758-250.

The first comprehensive catalog of X-ray binaries was presented by Van Paradijs (1995). Our catalog includes, as X-ray binaries, the point X-ray sources powered by accretion onto neutron stars and black holes. The weak sources powered by stellar coronas, Wolf-Rayet stars, and cataclysmic variables are not included. Among those X-ray binaries presented in the catalog, there are 78 HMXBs (35 and 5 of which are pulsars and possible pulsars, respectively) and 138 LMXBs (only 9 of which are pulsars), 89 transient and possible transient sources, and 25 possible black holes (6 HMXBs+19 LMXBs). There are also 43 bursters (all of which are Galactic LMXBs) and 21 QPOs. The present catalog extends the work by Van Paradijs, tabulates further information on the compact objects and their companions, as discussed below, as well as attempts to provide a more comprehensive guide to the literature. Where different authors obtained different values for system parameters, we have quoted all parameter values together with the references to guide the reader to the relevant literature for the derivation of the parameters. We introduce the catalog with four examples given in tabular form below.

* E-mail address for contacts: huseyin@sci.akdeniz.edu.tr

1063-7737/00/2611-0725$20.00 © 2000 MAIK "Nauka/Interperiodica"

Data for 2 HMXBs and 2 LMXBs

Table 1 (sample)

Name	Location	Type	RA (2000)	Dec (2000)	RA (1950)	Dec (1950)
0115+634		P, T	$01^n18^m32^s$	63°44′24″	$01^n15^m13\overset{s}{.}8$	63°28′38″
0115–737	SMC	P	01 17 05	−73 26 35	01 15 45.6	−73 42 22
J0422+32		Q, R	04 21 42.7	32 54 27.1	04 18 29.9	32 47 24
0620–003		R	06 22 44.4	00 20 44.7	06 20 11.1	−00 19 11

Table 2 (sample)

Name	l^{II}	b^{II}	P_{orb}, days	P_{pulse}, s	P_{rem}	kT, keV	α	Distance, kpc
0115+634	125.9	1.0	24.309	3.61451	*			*
0115–737	300.4	–43.6	3.89239	0.717	*	0.18*		57
J0422+32	165.9	–11.9	0.212140			2		1.2*
0620–003	210	–6.5	0.325		*	*	~1.6	1*

Table 3 (sample)

Name	$\log N_H$, cm^{-2}	A_V, mag.	L_X, erg s^{-1}	L_X/L_0	SpecT	V, mag.	$B–V$, mag.
0115+634	22.08	>5	*	1.7	OBe	14.8*	1.61*
0115–737	<21.60	0.1	6.0×10^{38}	*	B0 Ib	13.3	–0.14
J0422+32	<21.7*	1.2*	2.7×10^{37}	*	M2 V	22.24*	0.15*
0620–003	21.2*	1.2	$1.0\times10^{38*}$	200	K4–K7 V	18.3	1.4

Table 4 (sample)

Name	$U–B$, mag.	$E(B–V)$, mag.	M_X, $M_\odot$	M_{opt}, $M_\odot$	$f_X(M)$, $M_\odot$	$f_{opt}(M)$, $M_\odot$	e_{opt}
0115+634	0.3	1.7		>20*	5		0.34
0115–737	–0.98	~0.1*	1.17*	15.2*	10.8		$<10^{-5}$*
J0422+32	–0.5	0.2*	>3*	0.39*	3.1*	0.9	
0620–003	–0.8	0.35*	5.17	*		2.9	

Table 5 (sample)

Name	K_X, km s^{-1}	K_{opt}, km s^{-1}	γ, km s^{-1}	$a_1 \sin i$, light-s	$a_2 \sin i$, light-s	i, deg
0115+634	133.7		365	140		
0115–737	299.5	*	180	53.46*		70*
J0422+32	41.6	380*				≤45*
0620–003	43*	442*	–28	0.311	2.03	90*

THE CATALOG

This paper aims at providing a guide in print to the long and comprehensive full catalog of X-ray binaries at the Web site http://astroa.physics.metu. edu.tr/XRBC/. Below, we present the data and references of HMXBs 0115+634, 0115-737 and LMXBs J0422+32, 0620-003 as examples. The full catalog on the Web will be updated periodically.

The full catalog mainly consists of two parts, hmxb and lmxb, each of which has four files:

(1) The main catalog is composed of hmxb_cat and lmxb_cat. The most recent and/or the most reliable data are given in these files.

(2) All of the cross catalog names of the sources and the names of the optical counterparts are given in hmxb_nam and lmxb_nam.

Table 6 (sample)

Name	Names of optical counterparts	Other names of sources
0115+634	V635 Cas	2E 0115.1+6328
		H 0115+634, 1H 0115+635
		3U 0115+63, 4U 0115+63
		1XRS 01152+634
		PSR B0115+63.4
0115–737	Sk 160	SMC X-1
		2A 0116–737, 3A 0115–737
		1E 0115.5–7342, 2E 0115.8–7342
		H 0115–737
		3U 0115–73, 4U 0115–73
		1XRS 01157–737
		SK 160, WW 63
J0422+32	V518 Per	GRO J0422+32
		Nova Persei 1992
0620–003	V616 Mon	A 0620–00
		N Mon 1917, 1975

(3) The intensity values (in units of μJy, erg cm^{-1} s^{-2}, and mCrab), energy bands, dates of observations, names of satellites for these observations, and the references of all these data are given in hmxb_obs and lmxb_obs.

(4) All of the data other than the most recent and/or the most reliable ones are presented in hmxb_rem and lmxb_rem. The values given in intervals are also presented in these two files (e.g., a distance value of 4–5 kpc of a source is given in hmxb_rem or lmxb_rem (not in hmxb_cat or lmxb_cat) even if it is the most recent and/or the most reliable distance value of that source).

The columns in the main catalog (hmxb_cat and lmxb_cat) present: (1) numbers of the sources according to right ascension (RA), (2) names, (3) locations, (4) types (H—black hole, B—burster, P—pulsar, T—transient, R—recurrent tr., Q—QPO), (5) right ascension RA (2000), (6) declination (dec) (2000), (7) RA (1950), (8) dec (1950), (9) Galactic longitude (l^{II}), (10) Galactic latitude (b^{II}), (11) orbital period (P_{orb}), (12) pulse period (P_{pulse}), (13) remarks on period values (P_{rem}) (shown with asterisks), (14) X-ray temperature *kT*, (15) spectral index (α), (16) distance, (17) logarithm of neutral hydrogen column density ($\log N_H$), (18) optical absorption (A_V), (19) X-ray luminosity (L_X), (20) X-ray to optical luminosity (L_X/L_0), (21) spectral type (SpecT), (22) *V* (stellar magnitude), (23) *B–V* (stellar magnitude), (24) *U–B* (stellar magnitude), (25) *E(B–V)* (stellar magnitude), (26) mass of the compact object (M_X), (27) mass of the

Table 7 (sample)

Name	References	Dates	Satellites	Energy bands, keV
0115+634	1994IAUC.5990....1S	Jan., 1971	Uhuru	2–6
	1994IAUC.5999....2W	May 15, 1994	BATSE	20–40
	1997MNRAS.284..859N	May 18, 1994	BATSE	20–50
		May 28, 1994	BATSE	20–50
		May 30, 1994	BATSE	20–50
	Intensity, μJy	Intensity, erg cm^{-2} s^{-1}	Intensity, mCrab	
	120			
			45	
			65	
			75	
			180	
0115–737	1977ApJ..217...543P	1971–73	Uhuru	2–6
	60			
J0422+32	1995ApJ...441..786C	Aug. 8, 1992	GRO	20–300
	1992IAUC.5580....1P		GRO	2–11
	1993A&A...280L...1S		ROSAT	0.1–2.4
	1995ApJ...461..351C	1994	BATSE	2–11
			≫3	
		9.3×10^{-9}		
			0.3	
		9.3×10^{-9}		
0620–003	1975Nat..257...656E	Aug. 14, 1975	ArielV	2–18
		Jan. 7, 1976	S3	2–6
		Feb. 1976	ArielV	2–6
		Mar. 1976	ArielV	2–6
	83500		~25	
	300			
	1500			
	<70			

Table 8 (sample)

Name	References	Other Data	Values of Other Data
0115+634	1978Nat..273...367C	P_{pulse}	3.61 s
	1979Nat..282...240W	$P/\dot{P}$	5.9×10^{-11} s
	1983ApJ..270...711W	Distance	4.4, 3.5, 4, 3 kpc
	1991ApJ..375L...49N	Distance	5–7 kpc
	1992ApJ..389...657T	L_X	8×10^{36} erg s^{-1}
	1989A&A..217...115V	L_X	$(0.7–3) \times 10^{37}$ erg s^{-1}
	1978ApJ..223L...71J	M_{opt}	35 $M_\odot$
	1981ApJ..247...222H	Spec. Type	O–Be
		V	$14\overset{m}{.}5$–$16\overset{m}{.}3$, $15\overset{m}{.}5$
		$B–V$	$1\overset{m}{.}4$
0115–737	1986A&A..154....77T	Energy	2.17 keV
	1984ApJ..283...546W	L_X/L_{opt}	1.2–8
	1983ApJ..266...814M	M_X	1.6 $M_\odot$
	1981A&A...97...134B	M_{opt}	16 $M_\odot$
	1995A&A..303...497V	e_{opt}	<0.0007, 0
	1993MNRAS.261...337R	K_{opt}	19, 23 km s^{-1}
	1981A&A..101...184B	K_{opt}	23–27.5 km s^{-1}
	1984ApJ..283...249H	$a_1 \sin i$	53.5 light-s
	1982A&A..106...339V	i	67°
	1983ApJ..266...814M	$E(B–V)$	$0\overset{m}{.}03$
J0422+32	1993A&A...273L..11P	P_{orb}	$0\overset{d}{.}2157$, 0.211, 0.216
	1995A&A..297...103C	Distance	~2, >1, 2.4, ≤2.2 kpc
	1993A&A..288L...1S	L_X/L_{opt}	44, ~500
	1995PASJ..47...31K	L_X/L_{opt}	4–75
	1993A&A..276L...37C	L_X	6.7×10^{36}, 1.5×10^{38}, 8×10^{36}
	1995ApJ..455...614F	$\log N_H$	21.23
	1995ApJ..446L...59O	A_V	$1\overset{m}{.}25$
	1996A&A..312...105C	M_X	>2.4, 3.57, 4–6, 2.9–6.2 $M_\odot$
	1995ApJ..441...779V	M_{opt}	<0.5 $M_\odot$
	1997ApJ..476L...23V	K_{opt}	~340, 300–400 km s^{-1}
	1992PASJ..44L...15F	i	41°–43°, <59°, 48°
	1992ApJ..399L..145R	Spec. Type	M0 V
	1995MNRAS.276L.35C	V	$13–20\overset{m}{.}7$, $12\overset{m}{.}6$, $22\overset{m}{.}4$
	1996MNRAS.282.191D	$B–V$	$0\overset{m}{.}3$, $0\overset{m}{.}38$
	1995ApJ..442...786C	$E(B–V)$	$0\overset{m}{.}3$, $0\overset{m}{.}4$
0620–003	1995ApJ..442...358M	P_{orb}	$0\overset{d}{.}323$
	1974A&SS..29...331A	Distance	0.9–1.1, 0.6–1.4, 0.87 kpc
	1977ApJ..212...203K	Energy	1.5–3.0 keV
	1986ApJ..308...110V	L_X	10^{38}, 1.6×10^{38}, 6×10^{30} erg s^{-1}
	1977ApJ..212...209K	$\log N_H$	21.59
	1994MNRAS.268.763S	M_X	6, ~10, 2.7–3.2, 3.19–3.82 $M_\odot$
	1988ApJ..334...336D	M_{opt}	0.6, 0.36, 0.5–0.8 $M_\odot$
	1977ApJ...217..181O	K_X	43 km s^{-1}
	1983ApJ...266L..27M	K_{opt}	457 km s^{-1}
	1994MNRAS.271L.10S	i	57°
	1990ApJ..359L...47H	Spec. Type	K3, K5V, K4–K5V
		V	$12–18^m$
		$B–V$	$0\overset{m}{.}2$
		$E(B–V)$	$0\overset{m}{.}4$

optical companion (M_{opt}), (28) mass function from X-ray observations (f_X), (29) mass function from optical observations (f_{opt}), (30) eccentricity of the orbit from optical observations (e_{opt}), (31) semi-amplitude velocity of the compact object (K_X), (32) semi-amplitude velocity of the optical companion (K_{opt}), (33) center-of-mass velocity (γ), (34) semi-major axis multiplied by inclination ($a_1 \sin i$), (35) ($a_2 \sin i$), and (36) inclination (i). An asterisk (*) shows that there are remarks on the related data.

ACKNOWLEDGMENTS

We are grateful to M.A. Alpar, H. Ögelman and Ü. Kiziloğlu for valuable discussions and helpful remarks. We thank M.A. Gürkan for his help in the preparation of the manuscript and T. Özişik for Internet Web Site support. This work was supported by the Scientific and Technical Research Council of Turkey, *TÜBITAK*, under the High Energy Astrophysics Research Unit TBAG Ü-18, and by the Research Fund of the University of Istanbul (project no. 952/0900 597).

REFERENCES

1. P. R. Amnuel, O. H. Guseinov, and Sh. Yu. Rakhamimov, Astrophys. J., Suppl. Ser. **41**, 327 (1979).
2. P. R. Amnuel, O. H. Guseinov, and Sh. Yu. Rakhaminov, Astrophys. Space Sci. **82**, 3 (1982).
3. W. Forman, C. Jones, L. Cominsky, *et al.*, Astrophys. J., Suppl. Ser. **38**, 357 (1978).
4. F. Frontera and F. Fuligni, Astrophys. J. Lett. **198**, L105 (1975).
5. R. Giacconi, H. Gursky, E. Kellog, and H. Tananbaum, Astrophys. J. Lett. **167**, L67 (1971).
6. R. Giacconi, H. Gursky, F. R. Paolini, and B. Rossi, Phys. Rev. Lett. **9**, 439 (1963).
7. J. E. Grindlay, H. Gursky, H. Schnopper, *et al.*, Astrophys. J. Lett. **205**, L127 (1976).
8. O. H. Guseinov, Astron. Zh. **47**, 1143 (1970) [Sov. Astron. **14**, 912 (1971)].
9. J. Harries, Nature **215**, 38 (1967).
10. T. H. Markert, P. F. Winkler, F. N. Laird, *et al.*, Astrophys. J., Suppl. Ser. **39**, 573 (1979).
11. I. M. McHardy, A. Lawrence, J. P. Pye, and K. A. Pounds, Mon. Not. R. Astron. Soc. **197**, 893 (1981).
12. E. Schreier, Astrophys. J. Lett. **172**, L112 (1972).
13. I. S. Shklovskiĭ, Astron. Zh. **44**, 930 (1967) [Sov. Astron. **11**, 749 (1967)].
14. M. van der Klis, F. Jansen, J. van Paradijs, *et al.*, Nature **316**, 225 (1985).
15. J. van Paradijs, in *X-ray Binaries*, Ed. by W. H. G. Lewin *et al.* (Cambridge Univ.Press, Cambridge, 1995).
16. R. S. Warwick, N. Marshall, G. W. Fraser, *et al.*, Mon. Not. R. Astron. Soc. **197**, 865 (1981).
17. K. S. Wood, J. F. Meekins, D. J. Yentis, *et al.*, Astrophys. J., Suppl. Ser. **56**, 507 (1984).
18. Y. Zel'dovich and O. H. Guseinov, Astrophys. J. **144**, 840 (1965).

Translated by V. Astakhov

Astronomy Letters, Vol. 26, No. 11, 2000, pp. 730–735. Translated from Pis'ma v Astronomicheskiĭ Zhurnal, Vol. 26, No. 11, 2000, pp. 848–854.

Oscillation Structure of Gamma-Ray Bursts and Their Possible Origin

S. S. Gershteĭn

Institute of High-Energy Physics, Protvino, Moscow oblast, 142284 Russia

Received May 16, 2000

Abstract—It is hypothesized that thermonuclear burning of the matter from the envelope of a massive compact star accreting onto a hot neutron star produced by spherically symmetric collapse of a stellar iron core can proceed in oscillation mode (much as is the case during thermal explosions of carbon–oxygen cores in lower mass stars). Local density oscillations near the neutron-star surface can generate shock waves; in these shocks, the electron–positron plasma is stratified from the remaining matter, and shells of an expanding relativistic fireball with an oscillation time scale in cosmological gamma-ray bursts (GRBs) of $\sim 10^{-2}$ s are formed. It is pointed out that the GRB progenitors can be nonrotating massive Wolf–Rayet (WR) stars whose collapse, according to observational data, can proceed without any substantial envelope ejection. © *2000 MAIK "Nauka/Interperiodica".*

Key words: *gamma-ray bursts, supernovae, Wolf–Rayet stars*

INTRODUCTION: THE FIREBALL MODEL

The observed gamma-ray bursts (GRBs) are a highly interesting and as yet unsolved phenomenon [see the reviews by Piran (1999), Postnov (1999), Blinnikov (1999), Luchkov *et al.* (1996) and references therein]. Optical identifications of GRBs with the host galaxies have proved that at least some of them originate in galaxies at redshifts $Z \geq 1$; i.e., they are cosmological in origin. This is consistent with the completely isotropic sky distribution of GRBs and with the statistical distribution of their number in intensity. Optical identifications of GRBs have made it possible to determine their distances and to establish that an enormous energy of 10^{52}–10^{54} erg is released in the gamma-ray (30–500 keV) band during them. Many of the observed GRB parameters can be explained in terms of the fireball model (Cavallo and Rees 1978; Goodman 1986; Paczynski 1986), an ultrarelativistically expanding cloud of electron–positron plasma. Ultrarelativistic expansion velocities (which naturally arise in an electron–positron plasma) (Goodman 1986) allow the problem of compactness of the GRB source to be solved (Goodman 1986; Paczynski 1986; Krolik and Pier 1991) and the nonthermal GRB spectrum to be reconciled with the short time scale of GRB variability ($\delta t \sim 10$ ms)[1]. Based on the fireball model, researchers also managed to predict the observable effects of long-term optical GRB afterglows produced by the interaction of a relativistically expanding fireball with the interstellar medium (Meszaros and Rees 1997) and the effect of an early afterglow, which overlaps in time with a long-duration GRB (Sari and Piran 1999a, 1999b; Sari 1997). Thus, the relativistic fireball model with a small number of baryons allows the observed GRB parameters to be reconciled and the accompanying phenomena to be explained. At the same time, the following questions are yet to be solved:

(1) The fireball formation mechanism.

(2) The great energy in the fireball.

(3) The presence of many ($\sim 10^2$–10^3) gamma-ray pulsations on a time scale $\delta t \approx 10$ ms in some GRBs. In our view, the latter can serve as the key to unraveling the mystery of GRBs. Here, we draw attention to the fact that γ-ray oscillations can naturally arise during hydrodynamic collapse of some compact massive nonrotating stars at the final stage of their evolution.

POSSIBLE OSCILLATION BURNING OF THERMONUCLEAR FUEL DURING HYDRODYNAMIC COLLAPSE

The formation of a fairly large iron core during the evolution of massive stars with $M \geq 10 M_\odot$ is known to be responsible for their hydrodynamic collapse. In this case, having exhausted the source of thermonuclear energy, the stellar core begins to contract and heat up. However, the resulting increase in pressure cannot stop the contraction, because the thermal energy is spent on the endothermic decay reaction of iron nuclei and, subsequently, on core neutronization. As a result, the core

[1] In this case, it is crucially important that a constraint on the number of baryons contained in a lepton–photon plasma, which must be small enough (Paczynski 1990; Shemi and Piran 1990), is the condition for its ultrarelativistic expansion.

* E-mail address for contacts: gershtein@mx.ihep.su

contraction gives way to a catastrophic hydrodynamic collapse, which ends with the formation of a hot neutron star (Hoyle 1946). According to Fowler and Hoyle (1965, 1967), accretion of the nuclear fuel remained in the stellar envelope onto a hot neutron star causes its explosion and ejection, which shows up as a supernova explosion. However, self-consistent hydrodynamic calculations did not confirm this hypothesis. It turned out that consistent allowance for neutrino radiation leads to a delay in collapse, which ceases only when the core matter becomes opaque to neutrino radiation. As a result of this delay, the accreting nuclear fuel burns in a deep gravitational potential, and, hence, the thermonuclear energy being released is not enough for the envelope to be ejected (Arnett 1966, 1967; Ivanova *et al.* 1970) [see, e.g., the review by Imshennik and Nadyozhin (1982) and references therein]. The shock wave, that emerges when collapse slows down, ejects only a minor fraction of the envelope with energy $\sim 10^{49}$ erg (Nadyozhin 1977a, 1977b, 1978), which is two orders of magnitude lower than the characteristic energy of a supernova explosion, 10^{51} erg. This phenomenon was therefore called "silent" or quiet collapse. Subsequent attempts to account for the supernova explosions during spherically symmetric collapse of massive stars did not produce the desirable result (Burrows 1987; Arnett 1987). At present, most experts incline to the idea that the observed explosions of supernovae with massive progenitors are associated, in one way or another, with the rotation effects of a collapsing star: magnetic pressure on the envelope, Rayleigh–Taylor instability, or a neutron-star breakup into two components [see, e.g., the reviews by Imshennik and Nadyozhin (1988, 1989) and references therein; Imshennik and Nadyozhin (1992)]. However, one should take into account the fact that the burning of thermonuclear fuel as it accretes onto a hot neutron star can proceed in oscillation mode. This effect is well known and shows up at the final evolutionary stage of low-mass stars, $3M_\odot \le M \le 10M_\odot$. An oxygen–carbon core with a degenerate electron gas is formed in such stars during their evolution. In this case, instability results from a thermal explosion in a degenerate stellar core, when its mass reaches a value close to the Chandrasekhar limit (Arnett 1969). The oscillation burning of thermonuclear fuel is physically quite understandable in this case if we take into account the relatively low calorie content of this fuel with carbon–oxygen and the like composition. The energy being released during a thermal explosion causes the degeneracy to be removed and the thermal pressure to increase, resulting in expansion of the star. The expansion causes the stellar temperature to decrease. This leads to subsequent contraction of the star and to an enhancement of the thermonuclear burning, which, in turn, results in its subsequent expansion and so on. The aforesaid is illustrated by Fig. 1, where the results of calculations are shown (Ivanova *et al.* 1977a, 1977b, 1977c; Chechetkin *et al.* 1977). The detected oscillations were not only preserved but were also enhanced when convection was taken into account, resulting in the so-called delayed detonation with an explosion energy of $\sim 10^{51}$ erg (the paper by V.S. Imshennik at the workshop in memory of S.I. Syrovatskii on March 2, 2000).

Such oscillations may also arise in layers of the thermonuclear fuel accreting onto a hot neutron star. In contrast to the case considered above, they can only be local, developing in the layers adjacent to the surface of a hot neutron star. The period of these oscillations can be estimated from dimension considerations:

$$\tau \sim \frac{1}{\sqrt{G_N \bar{\rho}}}, \tag{1}$$

where G_N is the gravitational constant, and $\bar{\rho}$ is the matter density near the neutron star. According to our calculations (see Fig. 2), $\bar{\rho} \sim 10^{11}$ g cm^{-3}. Thus, the oscillation period is

$$\tau \sim 10^{-2} \text{ s}, \tag{2}$$

which intriguingly matches the oscillation period of the gamma-ray flux from some GRBs[2]. Density and temperature oscillations near the surface of a hot neutron star must generate diverging shock waves in the surrounding envelope (with the density falling off with increasing radius) which are repeated with the oscillation frequency (see also the Appendix).

POSSIBLE STRATIFICATION OF ELECTRON–POSITRON PLASMA

The most important effect to be taken into account when considering the passage of shock waves through a stellar envelope is the possible stratification of electron–positron plasma, which takes place without affecting the electrical neutrality of ordinary matter (the nuclei and the electrons compensating for their electric charge). Such stratification is possible under light pressure in a propagating shock wave, because the Eddington limit for an electron–positron plasma is a factor of 3600 smaller than that for ordinary matter with nuclei $A \simeq 2Z$. Therefore, when an electron–positron plasma emerges on the stellar surface, it contains baryons with a relatively low density (just right to reconcile the fireball model with observational data). Note also that an equilibrium electron–positron plasma can arise in a rarefied stellar atmosphere at relatively low temperatures, because under these conditions at $kT \ll m_e c^2$,

[2] It should be noted that conditions for the generation of oscillations are also created in hot neutron stars produced by collapse of an iron core (Zentsova and Nadyozhin 1975). However, their frequency is at least two orders of magnitude higher.

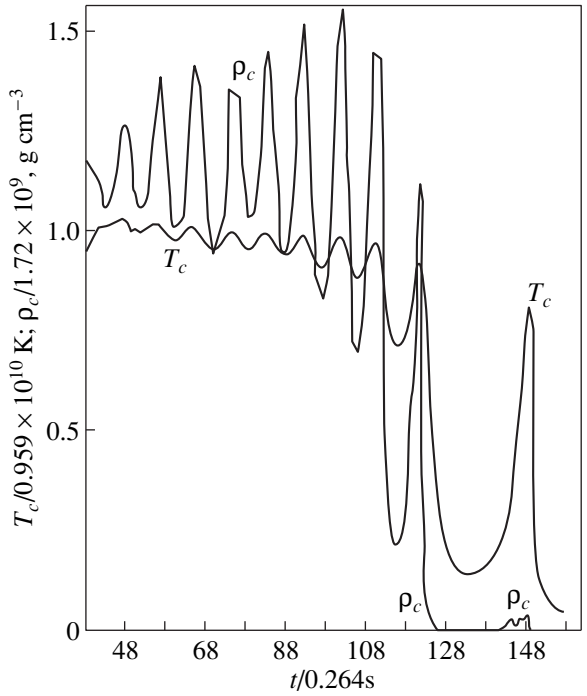

Fig. 1. Central density and temperature versus time during a carbon flash. The pulsation mode of carbon burning, which gives way to a complete expansion of the stellar core (Chechetkin *et al.* 1977; Imshennik and Nadyozhin 1982, 1983), is clearly seen.

$$n_{e^+} \approx n_{e^-} \approx \frac{1}{(2\pi^3)^{1/2}}\left(\frac{m_e c}{\hbar}\right)^3 e^{-1/x} x^{3/2},$$
$$x = \frac{kT}{mc^2} \ll 1, \quad (3)$$

whereas in a dense medium, the positron density is proportional to $\exp -\left(\frac{2mc^2}{kT}\right)$ (see, e.g., Zel'dovich and Novikov 1971). The fact that fairly high temperatures ($kT \geq m_e c^2$) develop near the center of a collapsing star is confirmed by the existence of explosive nucleosynthesis of ^{56}Ni nuclei to produce ^{56}Co, as suggested by observations of SN 1987 (Imshennik and Nadyozhin 1988, 1989; Woosley 1988). According to the calculations by Nadyozhin (1977a, 1977b, 1978), $kT \simeq 5.6$ MeV near the neutrinosphere.

When a cloud of electron–positron plasma emerges from the stellar atmosphere, its expansion inevitably becomes ultrarelativistic (see, e.g., Goodman 1986). This is known to cause variations in the pulse of gamma-ray radiation received by a distant observer:

$$\delta t \simeq \frac{R}{2c\Gamma^2}, \quad (4)$$

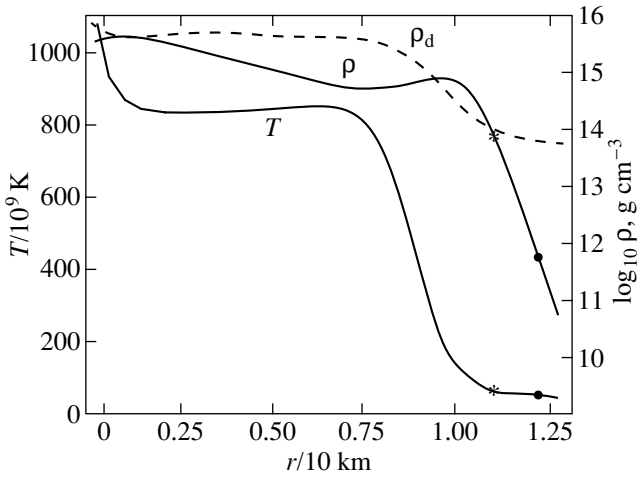

Fig. 2. The density and temperature distributions over a hot neutron star (the dashed line represents the degeneracy density). The position of the neutrino photosphere is marked by an asterisk, and the neutron core boundaries are represented by a filled circle (Nadyozhin 1978).

where R is the cloud radius, and $\Gamma = (1 - v^2/c^2)^{-1/2}$ is the Lorentz factor corresponding to the expansion velocity v. Clearly, gamma-ray oscillations are observed if

$$\delta t \leq \tau. \quad (5)$$

Otherwise ($\delta t \gg \tau$), gamma-ray oscillations are obscured for a distant observer. This could be the reason why no oscillations are seen in some GRBs. The stratification of an electron–positron plasma from ordinary matter must cause each oscillation near the neutron star to generate shock waves in the form of two shells expanding at different velocities. In this case, the electron–positron shell emitted in the succeeding oscillation can catch up with the shell containing baryons emitted in the preceding oscillation. Thus, the internal shock waves can interact inside the fireball itself (Narayan and Paczynski 1992; Paczynski and Xu 1994; Rees and Meszaros 1994; Sari and Piran 1999a, 1999b).

The ultrarelativistic pattern of fireball expansion ($\Gamma \sim 10^2$) leads us to conclude that, at the observed $\delta t \sim 10^{-2}$ s, the fireball sizes can be large enough (and, accordingly, the plasma density can be low enough) for the fireball to be considered as a "thin" source. This allows the nonthermal (power-law) GRB spectrum to be explained. The internal shock waves producing the fireball can also generate high-energy particles by the standard acceleration mechanism. This can account for the observation of high-energy (up to 18 GeV) gamma-ray photons in some GRBs.

POSSIBLE GRB PROGENITORS

The above scenario for the emergence of oscillations in GRBs restricts the class of objects that could be the GRB progenitors.

First, these must be sufficiently massive stars with $M > (15–20)M_\odot$. The quiescent evolutionary stage of such stars must end in times of the order of several Myr or less. A sufficiently large stellar mass is also required to account for the GRB energy.

Second, these must be nonrotating (or slowly rotating) stars. Rapidly rotating stars must apparently explode through effects related to their rotation as ordinary Type II supernovae with the ejection of a fairly massive envelope (Imshennik 1992).

Third, these must be compact stars without an extended hydrogen and, possibly, partially helium envelope, which is capable of preventing the outward emergence of electron–positron plasma because of positron annihilation.

Wolf–Rayet (WR) stars—the most massive compact stars that have lost virtually all their hydrogen and partially helium envelope during their evolution—satisfy all these requirements. It may be in connection with the loss of much of their envelope that they also lost their angular momentum. In any case, rotation is observed only in 15% of the WR stars (Harries *et al.* 1998). A.M. Cherepashchuk [see Cherepashchuk (1996, 1998) and references therein] established that the decrease in the mass of WR stars during their subsequent evolution (which takes place due to stellar wind) could be disregarded. This allows the masses of WR stars and their CO cores to be compared with the masses of relativistic objects (neutron stars and black holes), whose progenitors are WR stars. Based on measurements of the masses of X-ray sources in binary systems, A.M. Cherepashchuk reached a crucially important conclusion that the mass distribution of X-ray sources is distinctly bimodal. There is a gap in mass between neutron stars (pulsars) whose masses lie in a narrow range $(1–2)M_\odot$ with a mean mass of $(1.35 \pm 0.15)M_\odot$ and black-hole candidates whose masses are distributed over the range $(5–15)M_\odot$ with a mean mass of $(8–10)M_\odot$. The bimodal mass distribution and the existence of a gap provide evidence for different origins of these objects. As for the massive black-hole candidates, the correlation noted by Cherepashchuk (1996, 1998) between their masses and the masses of WR stars, which lie in the range $(5–55)M_\odot$ and whose CO cores have a mean mass of $(8–12)M_\odot$, close to the mean mass of observable black-hole candidates, seems of considerable importance in elucidating their origin. Thus, there is reason to believe that at least some of the WR stars collapse into massive objects through "silent" collapse without any substantial ejection of their envelope. This is true primarily for the evolutionally most advanced WC stars with envelopes rich in carbon nuclei (produced by thermonuclear helium burning) whose mean mass is $13.4M_\odot$. The data by Cherepashchuk (1996, 1998) are a strong argument for the hypothesis put forward by Conti (1982, 1998) back in 1982 that WR stars most commonly disappear as a whimper rather than as an explosion[3].

The compact structure of WR stars suggests that the shells of electron–positron plasma produced by stratification in shock waves can go outside the star, and even a minor fraction of the large gravitational energy released during the collapse of a massive star can account for the GRB energy.

GRB ENERGY

In order to determine the GRB energy requires a self-consistent hydrodynamic calculation of silent collapse of massive stars with allowance for the possible stratification of e^+e^- plasma from the remaining matter. However, we can attempt to estimate the possible GRB energy from physical (though not very reliable) considerations. If a gravitational energy $\epsilon \approx 5 \times 10^{53}$ erg is released in the form of neutrino radiation during collapse into a hot neutron star of mass $M = 1.5M_\odot$, then one might expect a gravitational energy $\sim\epsilon \simeq 10^{56}$ erg to be released at $M = (15–20)M_\odot$ (when no envelope ejection occurs)[4]. Therefore, to ensure a GRB energy of $\sim 10^{53}$ erg, it will suffice that ~0.1% of the gravitational energy being released be spent on the ejection of e^+e^- plasma. Such an estimate can also be obtained by using calculations of hydrodynamic collapse of an iron–oxygen stellar core (Nadyozhin 1977a, 1977b, 1978) with certain boldness. Although the shock wave emerging in this process is damped through neutrino radiation and its power is not enough to account for the supernova explosion, the energy of the ejected envelope can still be $\sim 10^{49}$ erg. For the inferred envelope expansion velocity $v \sim 1.5 \times 10^3$ km s^{-1}, the mass of the ejected envelope is $\Delta M \simeq 0.44\ M_\odot$. If such a mass were ejected in the form of e^+e^- plasma, then an energy of 8×10^{53} erg would be released during its subsequent annihilation. Of course, the above comparison is not entirely justified, but it gives an idea of the possible magnitude of the effect. The bulk of the GRB energy in the mechanism under consideration is thus gravitational in origin. The heating of a collapsing star gives rise to a dense and hot e^+e^- plasma, while the energy being released during the oscillating burning of thermonuclear fuel is spent on the generation of shock waves, which drive the e^+e^- plasma out of the star.

The possible pumping of energy into the diverging e^+e^- plasma through the neutrinos and antineutrinos emitted during collapse (because during their scattering by electrons and positrons, they can transfer much of their energy to the latter) should also be taken into account. The gamma-ray spectra of GRBs require a special consideration. It may well be that the absence of

[3] Some WR stars may be Ib supernova progenitors (I am grateful to V.S. Imshennik for this remark.) Rotating WR stars could also be such objects.

[4] Note that a hot neutron star can be stable up to a mass $M_{NS} \approx 70M_\odot$ (Bisnovatyĭ-Kogan 1968).

the 511-keV line from e^+e^- annihilation at rest is associated with ultrarelativistic fireball expansion.

DISCUSSION

Observational data (Cherepashchuk 1996, 1998) strongly suggest that massive, compact, nonrotating (Harries *et al.* 1998) Wolf–Rayet stars undergo relativistic collapse without any substantial ejection of their envelopes. This suggestion is consistent with the fact that, in our hydrodynamic calculations of spherically symmetric collapse of massive stars, we have failed to obtain the envelope ejection that is enough to account for supernova explosions. The gravitational energy released during relativistic collapse of such objects can be 10^{55}–10^{56} erg.

Here, we hypothesize that the thermonuclear fuel accreting onto a hot neutron star burns in oscillation mode, generating shock waves that drive the e^+e^- plasma out of the star (if it is stratified). This hypothesis qualitatively accounts for the emergence of a relativistic fireball with a low content of baryons and the oscillations observed in GRBs (the oscillation period is quantitatively explained in order of magnitude). The GRB duration (~20 s) is in agreement with the time it takes for the outer envelope to accrete onto a neutron star and with its cooling time. The fact that WR stars can be the GRB progenitors is supported by observational data provided by Paczynski (1998), in particular, by evidence that GRBs originate in regions of intense star formation.

According to our hypothesis, the collapse of a WR star and the ejection of e^+e^- plasma are spherically symmetric. Spherical symmetry of GRBs is suggested by the successful description of optical afterglows on long (of the order of 200 days) time scales (Wijers *et al.* 1977). (Though there is evidence that jets can appear in some GRBs.)

ACKNOWLEDGMENTS

I wish to thank G.V. Domogatskiĭ, A.M. Dykhna, V.S. Imshennik, A.A. Logunov, D.K. Nadyozhin, and K.A. Postnov for interest in this study and for valuable discussions. I am particularly grateful to A.M. Cherepashchuk, who familiarized me with his work and with the data pertaining to WR stars. This study was supported by the Russian Foundation for Basic Research (project nos. 99-02-16 558 and 00-15-96 645).

REFERENCES

1. W. D. Arnett, Can. J. Phys. **44**, 2553 (1966).
2. W. D. Arnett, Can. J. Phys. **45**, 1621 (1967).
3. W. D. Arnett, Astrophys. Space Sci. **5**, 180 (1969).
4. W. D. Arnett, Astrophys. J. **319**, 136 (1987).
5. G. S. Bisnovatyĭ-Kogan, Astrofizika **4**, 221 (1968).
6. S. Blinnikov, astro-ph/9911138 (Nov. 9, 1999).
7. A. Burrows, Astrophys. J. Lett. **318**, L57 (1987).
8. G. Cavallo and M. J. Rees, Mon. Not. R. Astron. Soc. **183**, 359 (1978).
9. A. M. Cherepashchuk, Astron. Soc. Pac. Conf. Ser. (2000), accepted 1996.
10. A. M. Cherepashchuk, in *Proceedings of the International Conference in Honour of Prof. A. G. Massevitch "Modern Problems of Stellar Evolution,"* Ed. by D. S. Wiebe (Zvenigorod, 1998), p. 198.
11. V. M. Chechetkin, V. S. Imshennik, L. N. Ivanova, and D. K. Nadyozhin, in *Supernovae*, Ed. by D. N. Shramm (Reidel, Doredrecht, 1977), p. 159.
12. P. S. Conti, in *Wolf-Rayet Stars: Observations, Physics, Evolution*, Ed. by C. W. H. de Loore and A. J. Willis (Reidel, Dordrecht, 1982), p. 3.
13. P. S. Conti, in *Wolf-Rayet Stars in the Framework of Stellar Evolution*, Ed. by J. M. Vreiex *et al.* (Liege Univ., 1996), p. 655.
14. W. A. Fowler and F. Hoyle, *Neutrino Processes and Pair Formation in Massive Stars and Supernovae* (Univ. of Chicago Press, Chicago, 1965; Mir, Moscow, 1967).
15. J. Goodman, Astrophys. J. Lett. **308**, L47 (1986).
16. T. J. Harries, D. J. Hiller, and I. D. Howarth, Mon. Not. R. Astron. Soc. **29**, 1072 (1998).
17. F. Hoyle, Mon. Not. R. Astron. Soc. **106**, 343 (1946).
18. V. S. Imshennik, Pis'ma Astron. Zh. **18**, 489 (1992) [Sov. Astron. Lett. **18**, 194 (1992)].
19. V. S. Imshennik and D. K. Nadyozhin, Itogi Nauki Tekh., Ser.: Astronomiya **21**, 63 (1982).
20. V. S. Imshennik and D. K. Nadyozhin, Sov. Sci. Rev., Sect. E **2**, 75 (1983).
21. V. S. Imshennik and D. K. Nadyozhin, Usp. Fiz. Nauk **156**, 561 (1988).
22. V. S. Imshennik and D. K. Nadyozhin, Sov. Sci. Rev., Sect. E **8**, 1 (1989).
23. V. S. Imshennik and D. K. Nadyozhin, Pis'ma Astron. Zh. **18**, 195 (1992) [Sov. Astron. Lett. **18**, 79 (1992)].
24. L. N. Ivanova, V. S. Imshennik, and D. K. Nadyozhin, Nauchn. Inf. Astron. Soveta Akad. Nauk SSSR **13**, 3 (1970).
25. L. N. Ivanova, V. S. Imshennik, and V. M. Chechetkin, Astron. Zh. **54**, 354 (1977a) [Sov. Astron. **21**, 197 (1977a)].
26. L. N. Ivanova, V. S. Imshennik, and V. M. Chechetkin, Astron. Zh. **54**, 661 (1977b) [Sov. Astron. **21**, 374 (1977b)].
27. L. N. Ivanova, V. S. Imshennik, and V. M. Chechetkin, Astron. Zh. **54**, 1009 (1977c) [Sov. Astron. **21**, 571 (1977c)].
28. J. H. Krolik and E. A. Pier, Astrophys. J. **373**, 277 (1991).
29. B. I. Luchkov, I. G. Mitrofanov, and I. L. Rozental', Usp. Fiz. Nauk **167**, 743 (1996) [Phys. Usp. **39**, 695 (1996)].
30. P. Mészáros and M. J. Rees, Astrophys. J. **476**, 232 (1997).
31. D. K. Nadyozhin, Astrophys. Space Sci. **49**, 399 (1977a).
32. D. K. Nadyozhin, Astrophys. Space Sci. **49**, 283 (1977b).
33. D. K. Nadyozhin, Astrophys. Space Sci. **53**, 131 (1978).
34. R. Narayan, B. Paczynski, and T. Piran, Astrophys. J. Lett. **395**, L83 (1992).

35. B. Paczynski, Astrophys. J. Lett. **308**, L43 (1986).
36. B. Paczynski, Astrophys. J. **363**, 218 (1990).
37. B. Paczynski and G. Xu, Astrophys. J. **427**, 708 (1994).
38. B. Paczynski, in *Gamma-Ray Bursts*, Ed. by C. A. Meegan *et al.* (American Inst. of Physics, 1998), p. 783.
39. T. Piran, Phys. Rep. **314**, 557 (1999).
40. K. A. Postnov, Usp. Fiz. Nauk **169**, 545 (1999).
41. M. J. Rees and P. Mészáros, Astrophys. J. Lett. **430**, L93 (1994).
42. R. Sari, Astrophys. J. Lett. **489**, L37 (1997).
43. R. Sari and T. Piran, Proc. Astron. Astrophys. **138**, 537 (1999a); astro-ph/9901105.
44. R. Sari and T. Piran, Astrophys. J. **520**, 641 (1999b); astro-ph/9901338.
45. A. Shemi and T. Piran, Astrophys. J. Lett. **365**, L55 (1990).
46. R. A. Wijers, M. J. Rees, and P. Mészáros, Mon. Not. R. Astron. Soc. **288**, L51 (1997).
47. S. E. Woosley and T. A. Weaver, Phys. Rep. **163**, 79 (1988).
48. Ya. B. Zel'dovich and I. D. Novikov, *The Theory of Gravitation and Evolution of Stars* (Nauka, Moscow, 1971).
49. A. S. Zentsova and D. K. Nadyozhin, Astron. Zh. **52**, 234 (1975) [Sov. Astron. **19**, 146 (1975)].

APPENDIX

The detonation of thermonuclear fuel during hydrodynamic collapse, which produces local oscillations, could begin before its accretion onto a hot neutron star. In this case, the oscillation period can be roughly estimated as

$$\tau \simeq 2\pi\sqrt{\frac{\Delta R}{g}},$$

where ΔR is the oscillation amplitude, and g is the free-fall acceleration on the inner mass $M(R^*)$ corresponding to the detonation radius R^*. Assuming the calorie content of the thermonuclear fuel to be $q \simeq$ 1 MeV/nucleon $\simeq 10^{-3} m_N c^2$ and $\Delta R \ll R^*$, we have

$$g\Delta R \simeq 10^{-3} c^2;$$

hence, we obtain an estimate for τ

$$\tau \approx 2 \times 10^2 \frac{\Delta R}{c}.$$

At $\tau \simeq 10^{-2}$ s, ΔR is

$$\Delta R \simeq 1.5 \times 10^6 \text{ cm},$$

and the radius at which the detonation takes place is

$$R^* \simeq 1.5 \times 10^7 \sqrt{\frac{M(R^*)}{M_\odot}} \text{ cm}.$$

It stands to reason that testing our hypothesis requires a consistent calculation of hydrodynamic collapse.

Translated by V. Astakhov

Astronomy Letters, Vol. 26, No. 11, 2000, pp. 736–742. Translated from Pis'ma v Astronomicheskiĭ Zhurnal, Vol. 26, No. 11, 2000, pp. 855–861.

Peculiarities of the Plasma Mechanism of Radio Emission from Late-Type Stars

V. V. Zaĭtsev[1], E. G. Kupriyanova[2]*, and A. V. Stepanov[2]

[1] *Institute of Applied Physics, Russian Academy of Sciences, ul. Ul'yanova 46, Nizhniĭ Novgorod, 603600 Russia*
[2] *Pulkovo Astronomical Observatory, Russian Academy of Sciences, Pulkovskoe sh. 65, St. Petersburg, 196140 Russia*

Received May 26, 2000

Abstract—The plasma mechanism of radio emission in the coronas of late-type stars is shown to be considerably more efficient than that in the solar corona because of the high plasma temperature in their magnetic arches. This is attributable to an increase in the length of plasma-wave conversion into electromagnetic waves and a decrease in the optical depth of collisional wave absorption. Magnetic-arch filamentation results in a decrease in the intensity of the fundamental-tone radio emission and in the relative dominance of the second-harmonic radio emission. The efficiency of the fundamental-tone radio emission increases with plasma density in a coronal arch. The plasma mechanism accounts for the high brightness temperature of the flare radio emission from stars ($\geq 10^{14}$ K). © *2000 MAIK "Nauka/Interperiodica".*

Key words: *stars—variable and peculiar stars; Sun*

INTRODUCTION

UV Cet flare red dwarfs and close RS CVn- and Algol-type binaries, which consist mainly of subgiants, giants, or dwarfs, belong to the late-type radio stars. It is customary to divide stellar radio emission into quiescent and flaring one. By contrast to the solar radio emission, the quiescent stellar radio emission is nonthermal in nature (the brightness temperatures reach 10^9 K) and is most likely associated with the gyrosynchrotron emission of energetic electrons in the magnetic fields of stellar coronas. Sporadic (flaring) radio emission with high brightness temperatures $T_b \sim 10^{10}$–10^{16} K is produced by masing mechanisms in stellar coronas. Two of the masing mechanisms are usually discussed: an electron cyclotron maser (ECM) and a plasma mechanism. ECM emission arises if the electron distribution function in magnetoactive plasma is unstable to the generation of ordinary and extraordinary electromagnetic waves near the low electron-gyrofrequency harmonics (Melrose 1994; Fleishman and Mel'nikov 1998). An electron cyclotron maser is realized in stellar coronas with relatively strong magnetic fields, at $\omega_p/\omega_c < 1$, and becomes inefficient at $\omega_p/\omega_c > 1$ (Sharma and Vlahos 1984). Here, ω_p and ω_c are the plasma frequency and the electron gyrofrequency, respectively. In addition, there is a problem with the escape of ECM radio emission from the corona. The point is that an ECM generates mostly extraordinary waves. However, as was shown by Stepanov *et al.* (1995), it is an extraordinary wave that is mainly absorbed in hot stellar coronas.

The coherent plasma mechanism includes two stages: the generation of Langmuir turbulence and the subsequent conversion of plasma waves into electromagnetic ones. Observations of late-type stars suggest that, in several cases, especially in events with a fine structure, the plasma mechanism of radio emission takes place (Bastian *et al.* 1990; Abada-Simon *et al.* 1994; White and Franciosini 1995; Stepanov *et al.* 1995). In some measure, sporadic stellar radio emission is similar to solar type II, III, and V meter bursts and to type IV decimeter bursts. Such stellar radio emission is characterized by high ($\geq 10^{10}$ K) brightness temperatures, a high (up to 100%) degree of polarization (occasionally in the form of an ordinary wave), a frequency drift, and rapid variability. The plasma mechanism of generation of such bursts on the Sun is universally recognized. Despite the phenomenological similarity between the parameters of flaring radio emission, the results of calculations of wave transformation for the solar corona cannot be directly applied to stellar coronas. While studying the efficiency of coherent mechanisms under typical conditions of the coronas of the Sun and flare dMe stars, Abada-Simon *et al.* (1994b) pointed out that the efficiency of the plasma mechanism (the ratio of the radio flux density to the fast-electron density) in the coronas of red dwarfs is higher than that in the solar corona by several orders of magnitude. At the same time, they noted that the high efficiency could be related to peculiarities of the plasma-wave conversion into electromagnetic waves. The main feature of stellar radio emission is that the temperature in the

* E-mail address for contacts: lioka@gao.spb.ru

coronas of late-type stars is higher ($T \geq 10^7$ K) than that in the solar corona (Ottmann 1993). As we show below, this significantly increases the length of the resonant nonlinear interaction between plasma and electromagnetic waves and makes the plasma mechanism very efficient in stellar coronas.

It is widely believed (Dulk 1985; Melrose 1987; Skinner 1991) that the fundamental-tone plasma radio emission and the second harmonic can be observed in the solar and stellar coronas only at frequencies ≤300 MHz and ≤1 GHz, respectively. This constraint is based on the formula of Dulk (1985) for the optical depth of collisional absorption of the fundamental-tone emission with frequency f

$$\tau_{\rm coll} = 1.5 \times 10^{-17} T^{-3/2} f^2 L. \quad (1)$$

The absorption for the second-harmonic plasma emission is a factor of 16 smaller. Indeed, $\tau_{\rm coll} \approx 1$ at $f =$ 300 MHz for $T = 10^6$ K and the source's size $L = 10^9$ cm. However, as follows from (1), free-free absorption in hot stellar coronas, for example, at temperature $T = 5 \times 10^7$ K is substantial only for a frequency $f > 5$ GHz.

The second feature is that red dwarfs and close binaries exhibit a considerably higher surface activity then does the Sun. The surface activity of a star is proportional to its rotational velocity, which is higher than that of the Sun (Katsova 1999). The surface activity of a star is characterized by the relative area of the photosphere occupied by spots. On the Sun, this parameter is less than 0.4% of the visible photospheric area in the years of solar maximum. It is considerably higher for late-type stars. It was found from photometric observations that the spot area accounts for up to 11–13% of the stellar surface for DK Leo, AD Leo, and GT Peg (Alekseev 1998), up to 42% for V775 Her, and up to 68% for the spectroscopic binary V833 Tau (Alekseev and Bondar' 1998). According to spectroscopic observations in the 705.5 and 886.0 nm TiO lines, spots cover 55 ± 5% of the stellar visible hemisphere in an RS CVn II Peg type binary (O'Neal *et al.* 1998). The magnetic arches connecting spots of different polarities are the main structural element of coronas and an active source of radio emission. Magnetic arches form active regions in the solar corona. In close binaries and on red dwarfs, they essentially form the magnetic structure of the entire corona. In this case, cool arches with a plasma temperature $T \sim 10^6$ K alternate with hot ($T \sim 10^7$–10^8 K) arches (White 1996). The interaction between arches results in plasma heating and in particle acceleration (Sakai and de Jager 1996). Thus, late-type stars with numerous coronal magnetic arches must be powerful sources of radio emission.

Coronal arches (loops) are magnetic traps for energetic particles, which form an anisotropic velocity distribution of the "loss-cone" type, resulting in plasma-wave instability. We consider the following coherent plasma mechanism of radio emission. We assume the plasma-wave spectrum to be specified and restrict ourselves to the case of a dense plasma ($\omega_{\rm p}^2 \gg \omega_{\rm c}^2$), because the role of the magnetic field reduces to a redistribution of the emission energy over the spectrum, while we are interested in the total stellar radio flux. Stepanov *et al.* (1999) considered a moderate magnetic field ($1 < \omega_{\rm p}^2/\omega_{\rm c}^2 \leq 5$) for the second-harmonic plasma emission.

THE TRANSFORMATION OF PLASMA WAVES INTO ELECTROMAGNETIC ONES

The Fundamental-Tone Radio Emission

The fundamental-tone radio emission ($\omega \approx \omega_{\rm p}$) arises during Rayleigh scattering of plasma waves by background plasma particles. The energy conservation law for scattering is

$$\omega_t - \omega_l = (\mathbf{k}_t - \mathbf{k}_l)\mathbf{v}, \quad (2)$$

where ω_t and $\mathbf{k}_t$, ω_l and $\mathbf{k}_l$ are the frequencies and wave vectors of the electromagnetic and plasma waves, respectively; and $\mathbf{v}$ is the velocity of the scattering particles.

At $\omega_{\rm p}^2 \gg \omega_{\rm c}^2$, the high-frequency electromagnetic waves are described by the dispersion relation

$$\omega_t^2 = \omega_{\rm p}^2 + k_t^2 c^2, \quad (3)$$

while the dispersion relation for the plasma waves is

$$\omega_l^2(k_l) = \omega_{\rm p}^2 + 3v_T^2 k_l^2. \quad (4)$$

From the dispersion relations (3) and (4) and the energy conservation law (2), we determine the region of a nonlinear wave interaction:

$$L = 3L_N \frac{v_T^2}{\omega_{\rm p}^2}(k_{\max}^2 - k_{\min}^2) \approx 3L_N \frac{v_T^2}{v^2}, \quad (5)$$

where L_N is the nonuniformity scale length of the particle density of a source in a coronal magnetic arch of the star, $L_N = N/|\nabla N|$; and v_T and v are the velocities of the background plasma particles and energetic particles, respectively,

$$v_T = \sqrt{\frac{T}{m_{\rm e}}}, \quad v = c\sqrt{1 - \left(\frac{m_{\rm e}c^2}{T_1 + m_{\rm e}c^2}\right)^2}. \quad (6)$$

Here, T_1 is the kinetic energy of the fast particles, and $k_{\max}$ and $k_{\min}$ are the maximum and minimum wave numbers of the generated plasma waves.

The transfer equation for the brightness temperature of radio emission appears as follows:

$$\frac{dT_{\rm b}}{dl} = a - (\mu_{\rm c} + \mu_{\rm nl})T_{\rm b}, \quad (7)$$

where a is the emission coefficient, $\mu_{\rm c}$ is the coefficient of absorption through collisions, and $\mu_{\rm nl}$ is the coeffi-

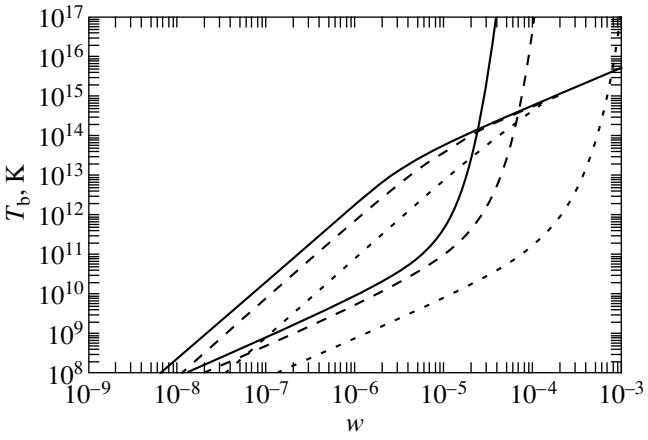

Fig. 1. Brightness temperature T_b versus plasma turbulence level w for the radio emission from AD Leo ($T = 10^7$ K, $T_1 = 3 \times 10^8$ K) in the case where the first harmonic of the electron plasma frequency is observed at $f = 1.415$ GHz. The solid, dashed, and dotted lines correspond to $L_N = 3 \times 10^9$, 10^9, and 10^8 cm, respectively.

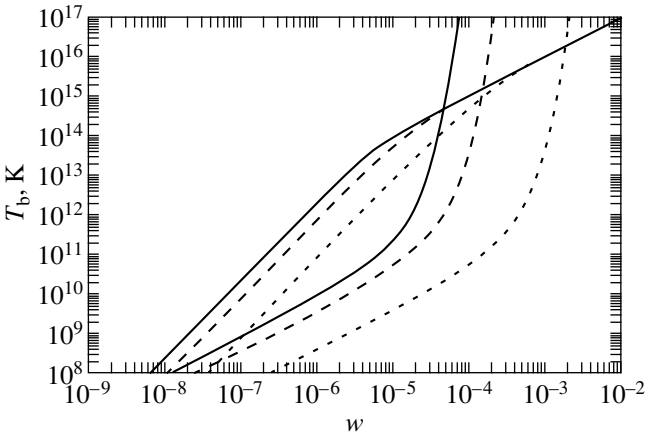

Fig. 2. Same as Fig. 1 in the case where the second harmonic of the electron plasma frequency is observed at $f = 1.415$ GHz.

cient of absorption through nonlinear interactions. The solution to the transfer equation (7) is

$$T_b = \frac{a}{\mu_c + \mu_{nl}}\left(1 - \exp\left(-\int_0^L (\mu_c + \mu_{nl})dl\right)\right), \quad (8)$$

where L is given by formula (5). The coefficients for the fundamental-tone radio emission are (Zaitsev and Stepanov 1983)

$$a_1 \approx \frac{\pi}{36}\frac{\omega_p}{v_g} m v^2 w, \quad (9)$$

$$\mu_{c1} = \frac{\omega_p^2 \nu_{ei}}{\omega_t^2 v_g} \approx \frac{\nu_{ei}}{v_g}, \quad (10)$$

$$\mu_{nl1} \approx -\frac{\pi}{108}\frac{m_e}{m_i}\frac{\omega_p}{v_g}\frac{v^2}{v_T^2} w, \quad (11)$$

where $v_g \approx \sqrt{3}\, v_T ck/\omega_p$ is the group velocity of the electromagnetic waves, $w = W/NT$ is the relative level of plasma turbulence, $W = \int W_k\, dk$ is the energy density of the plasma waves, and ν_{ei} is the frequency of electron–ion collisions

$$\nu_{ei} = \frac{5.5N}{T^{3/2}} \ln\left(10^4 \frac{T^{2/3}}{N^{1/3}}\right). \quad (12)$$

The equality of the absorption coefficients, $\mu_{c1} = |\mu_{nl1}|$, corresponds to $w = w_1$, where

$$w_1 = \frac{108}{\pi}\frac{m_i}{m_e}\frac{\nu_{ei}}{\omega_p}\frac{v_T^2}{v^2}. \quad (13)$$

Collisional and nonlinear processes mostly contribute to the emission at $w < w_1$ and $w > w_1$, respectively.

The Second-Harmonic Radio Emission

The radio emission at twice the plasma frequency is generated by Raman scattering of plasma waves. The energy and momentum conservation laws appear as follows:

$$\omega_1 + \omega_2 = \omega_t, \quad \mathbf{k}_1 + \mathbf{k}_2 = \mathbf{k}_t, \quad (14)$$

where ω_1 and $\mathbf{k}_1$, ω_2 and $\mathbf{k}_2$ are the frequencies and wave vectors of the interacting longitudinal plasma waves (the subscript l is omitted for simplicity).

In this case, the emission and absorption coefficients are (Zheleznyakov 1997)

$$a_2 \approx \frac{(2\pi)^5 \omega_p^4 NT}{15\sqrt{3}\, v c^3 \Delta^2} w^2, \quad (15)$$

$$\mu_{c2} \approx \frac{\nu_{ei}}{2\sqrt{3}c}, \quad (16)$$

$$\mu_{nl2} \approx \frac{(2\pi)^2}{15\sqrt{3}}\frac{\omega_p^4}{v c^3 \Delta} w, \quad (17)$$

where $\Delta = \frac{4\pi}{3}(k_{max}^3 - k_{min}^3)$ is the phase volume of the plasma waves.

RESULTS OF THE CALCULATIONS

In Figs. 1–6, brightness temperature T_b is plotted against plasma turbulence level w. Figures 1–4 show the plasma radio emission from the red dwarf AD Leo for typical observing frequencies: $f = 1.415$ GHz (Figs. 1 and 2) and $f = 4.856$ GHz (Figs. 3 and 4). Figures 1, 3 and 2, 4 refer to the cases where the observing fre-

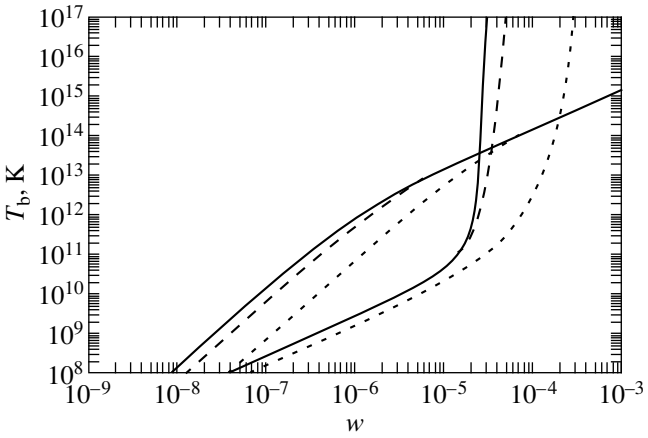

Fig. 3. Same as Fig. 1 in the case where the first harmonic of the electron plasma frequency is observed at $f = 4.856$ GHz.

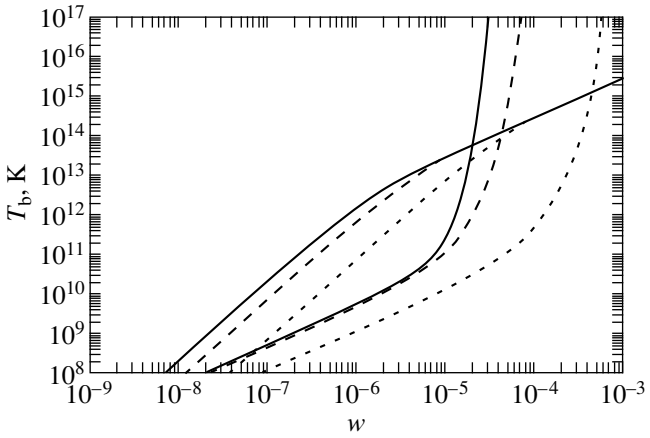

Fig. 4. Same as Fig. 1 in the case where the second harmonic of the electron plasma frequency is observed at $f = 4.856$ GHz.

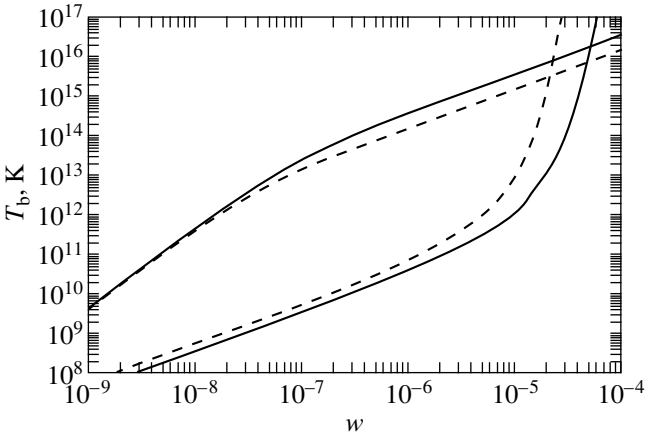

Fig. 5. Brightness temperature T_b versus plasma turbulence level w for the radio emission from a close binary. The following plasma parameters were used: $T = 3 \times 10^7$ K, $L_N = 3 \times 10^{10}$ cm, and $T_1 = 3 \times 10^8$ K. The solid and dashed lines correspond to the electron densities in the source $N = 10^9$ and 5×10^9 cm^{-3}, respectively.

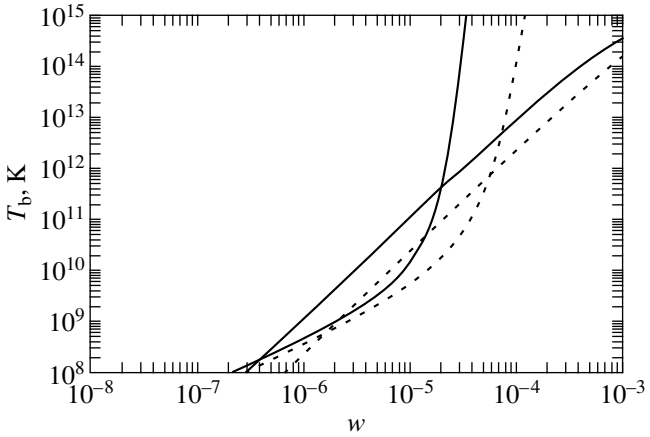

Fig. 6. Brightness temperature T_b versus plasma turbulence level w for the solar radio emission ($T = 10^6$ K, $T_1 = 3 \times 10^8$ K) at $f = 1$ GHz. The solid and dashed lines correspond to $L_N = 5 \times 10^8$ and 10^8 cm, respectively.

quency correspond to the fundamental tone and the second harmonic, respectively. In our calculations, we used the following plasma parameters: $T = 10^7$ K, $T_1 = 3 \times 10^8$ K (the fast-electron energy is 30 keV), $k_{max} = \omega_p/5v_T$, and $k_{min} = \omega_p/c$.

The filamentation of stellar coronal structures (a decrease in L_N) reduces the conversion efficiency at the fundamental tone and results in a relative dominance of the second-harmonic radio emission. The fundamental-tone radio emission dominates only at a comparatively high level of plasma waves (depending on plasma parameters, $w \approx 10^{-5}$–10^{-3}). At a plasma turbulence level $w < 10^{-5}$–10^{-3}, the second-harmonic radio emission dominates, reaching $T_b \approx 6 \times 10^{13}$–$7 \times 10^{15}$ K at $w \approx 10^{-5}$, whereas the brightness temperature of the fundamental-tone emission is $T_b \approx 4 \times 10^9$–$5 \times 10^{11}$ K. The values of w starting from which the fundamental-tone emission exponentially grows (maser effect) lies in the range $\omega \approx 3 \times 10^{-6}$–$2 \times 10^{-5}$, depending on the plasma parameters under consideration (Figs. 1–4).

Figure 5 shows the radio emission from close binaries. Van den Oord (1988) point out that a source of intense radio emission may exist between the binary components. Ipatov and Stepanov (1997) proposed a model of an interstellar flare based on the energy release in a prominence located between two stars. Prominence oscillations can cause periodic flares and the corresponding variations in radio emission. X-ray observations suggest the existence of a high-temperature ($T \sim 3 \times 10^7$ K) plasma with a relatively low density ($N \sim 3 \times 10^9$ cm^{-3}) confined in a trapping magnetic-field configuration (magnetic arches in the corona of one of the components or the fields connecting the binary components). Such a configuration is comparable in

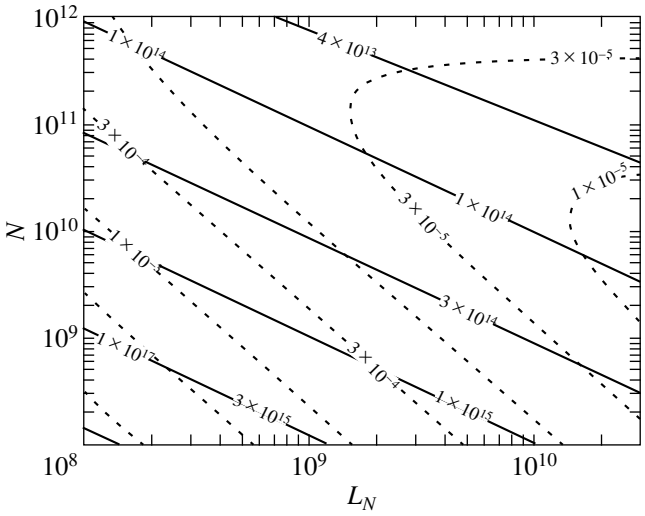

Fig. 7. Brightness temperature (solid lines) and plasma turbulence level w (dotted lines) at the points of intersection of the fundamental-tone and second-harmonic curves, $T_{b1}(w) = T_{b2}(w)$, for various L_N and N at $T = 10^7$ K and $T_1 = 3 \times 10^8$ K. The lines of constant w are shown at $10^{0.5}$ intervals.

size to the entire binary system (Walter *et al.* 1983; White *et al.* 1990). In our calculations, we assumed that $L_N = 3 \times 10^{10}$ cm, which corresponds to the sizes of characteristic structures in close binaries, and that $T_1 = 3 \times 10^8$ K. We see from Fig. 5 that an increase in the particle density causes a rise in the fundamental-tone radio emission and a reduction in the second-harmonic emission at a given w.

Figure 6 presents the case of the solar corona where the fundamental-tone radio emission corresponds to the frequency $f = 1$ GHz ($T = 10^6$ K, $T_1 = 3 \times 10^8$ K). Comparing Fig. 6 with Fig. 1, we see that the brightness temperatures of the second-harmonic radio emission for the Sun at a given w are much lower than those for red dwarfs. At $L_N = 10^8$ cm and $w \sim 10^{-5}$, the brightness temperatures of the fundamental-tone and second-harmonic radio emissions for AD Leo are $T_{b1} \approx 10^{10}$ K and $T_{b2} \approx 10^{13}$ K, whereas the corresponding values for the Sun are $T_{b1} \approx 5 \times 10^9$ K and $T_{b2} \approx 3 \times 10^{10}$ K. This is because the temperature of the solar corona is lower, which causes a decrease in the length of nonlinear interactions L and an increase in the width of the plasma-wave spectrum Δ [see formulas (5), (15), and (17)].

The brightness temperature and plasma turbulence level at the point of intersection of the fundamental-tone and second-harmonic curves are plotted against plasma parameters in Figs. 7–9. The $T_{b1}(w) = T_{b2}(w)$ lines are shown in Fig. 7 as a plot of nonuniformity scale length L_N versus particle density N, in Fig. 8 as a plot of L_N versus background plasma temperature T, and in Fig. 9 as a plot of L_N versus fast-particle energy T_1. We see from Fig. 7 that an increase in the plasma density causes the radio-emission brightness temperature at the point of intersection to decrease, in agreement with the results for close binaries (Fig. 5). It is evident from Fig. 8 that an increase in the plasma temperature causes the brightness temperature at the point of intersection where $T_{b1}(w) = T_{b2}(w)$ to increase. Figure 9 indicates that the brightness temperature at the point of intersection depends markedly on the energy of fast particles at $L_N < 3 \times 10^9$ cm. At $L_N > 3 \times 10^9$ cm, which correspond, for example, to the scale lengths of nonuniformities in close binaries, a change in the particle energy does not result in such considerable changes in the radio flux.

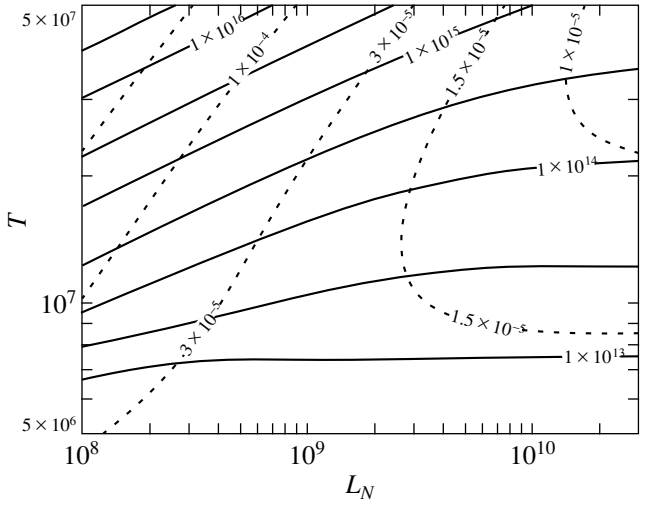

Fig. 8. Same as Fig. 7 for various L_N and T at $N = 3 \times 10^{11}$ cm^{-3} and $T_1 = 6 \times 10^8$ K. The maximum level is $w = 3 \times 10^{-4}$ K.

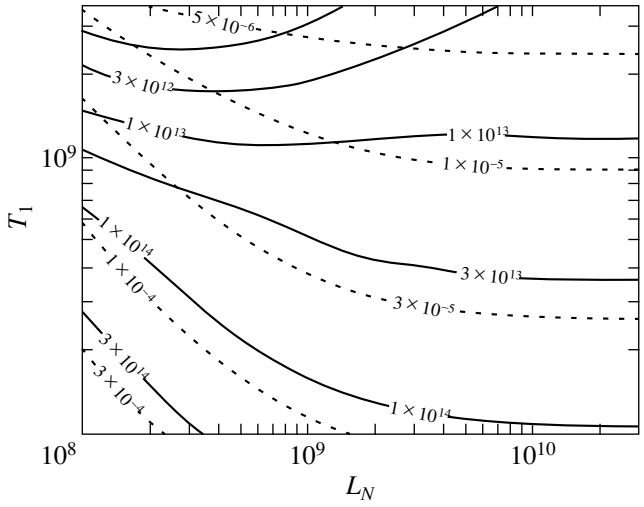

Fig. 9. Same as Fig. 7 for various L_N and T_1 at $N = 3 \times 10^{11}$ cm^{-3} and $T_1 = 10^7$ K. The lines of constant w and T_b are shown at $10^{0.5}$ intervals.

DISCUSSION AND CONCLUSIONS

The difference between the coronal parameters of late-type stars and the Sun necessitates a special consideration of the plasma mechanism of radio emission from stellar coronas. Their main distinctive feature is that the temperature of the stellar coronal plasma is higher than that of the solar one. Note that, since the emission at $T \le 10^7$ K cannot escape from the central part of an arch because of strong collisional absorption, only an outer arch layer of thickness L radiates effectively. As follows from formula (5), a rise in temperature causes an increase in the size of the region where plasma waves are transformed into electromagnetic waves and, consequently, a rise in the brightness temperature of the radio emission. This is the answer to the question (see Abada-Simon *et al.* 1994b) of why the plasma mechanism of radio emission is more efficient in stellar coronas than it is in the solar corona. Moreover, a high temperature of stellar coronas causes a reduction in the phase volume of plasma waves Δ and, consequently, a rise in the brightness temperature of the second-harmonic radio emission [Eqs. (15) and (17)].

The flux of weakly polarized radio emission is

$$F_f = \frac{2T_b f^2}{c^2}\frac{A}{d^2}, \qquad (18)$$

where A is the source area, and d is the distance to the star. Taking, according to Fig. 3, the brightness temperature to be $T_b \approx 10^{14}$ K near the point of intersection of the two curves at $L_N = \sqrt{A} = 3 \times 10^9$ cm, we find for AD Leo ($d = 4.85$ pc $\approx 1.55 \times 10^{19}$ cm) that $F_f \approx 3$ Jy at $f = 4.85$ GHz. Such fluxes are observed during intense flares on red dwarfs. For a close binary, for example, AR Lac ($T_b = 10^{14}$ K, $A = L_N^2 = 9 \times 10^{20}$ cm^2, $d = 50$ pc $= 1.5 \times 10^{20}$ cm, $f = 1$ GHz), from (18) we obtain $F_f \approx 120$ mJy, which also agrees with the observed radio fluxes from close binaries.

The filamentation of coronal arches is revealed by optical and X-ray observations of the Sun. We see from Figs. 1–7 that filamentation results in a reduction in the level of the fundamental-tone radio emission and in a relative dominance of the radio emission at the plasma-frequency second harmonic. At $w < 10^{-5}$–10^{-3} (depending on L_N), the second harmonic mainly contributes to the radio emission. For AD Leo at a turbulence level $w \sim 10^{-5}$, the brightness temperature of the second-harmonic radio emission is $T_b \sim 10^{14}$–10^{15} K (Figs. 1–4), whereas the corresponding value for the fundamental tone is $T_b \sim 10^9$–10^{11} K. Note that w is bounded above by the level of thermal fluctuations $w_{fl} = \frac{\omega_p^3}{6\pi^2 N v_T^3}$. In the range of plasma parameters in arches under study, $w_{fl} \approx 8 \times 10^{-10}$–$2 \times 10^{-9}$. At $w > 10^{-5}$–10^{-3}, the fundamental-tone radio emission is more intense than the second-harmonic emission due to the maser effect.

Intense ($T_b > 10^{10}$ K) and short-lived (<0.1 s) spike bursts are generally explained by instability of electromagnetic waves. Our calculations indicate that the two-step plasma mechanism of emission can also explain spike bursts because of its high efficiency at small source sizes.

Thus, hot stellar coronas create more favorable (than the solar corona) conditions for the generation of radio emission with frequencies 1–5 GHz by the plasma mechanism through an increase in the length of wave conversion and a reduction in collisional damping.

ACKNOWLEDGMENTS

This work was supported by the Russian Foundation for Basic Research (project nos. 00-02-16184 and 00-02-16 356) and State Science and Technology Program “Astronomy.”

REFERENCES

1. Abada-Simon, A. Lecacheux, M. Aubier, *et al.*, Astron. Astrophys. **288**, 219 (1994a).
2. Abada-Simon, A. Lecacheux, P. Lonarn, *et al.*, Astron. Soc. Pac. Conf. Ser. **64**, 339 (1994b).
3. I. Yu. Alekseev, Astron. Zh. **75**, 736 (1998) [Astron. Rep. **42**, 649 (1998)].
4. I. Yu. Alekseev and N. I. Bondar’, Astron. Zh. **75**, 742 (1998) [Astron. Rep. **42**, 655 (1998)].
5. Bastian, J. Bookbinder, G. Dulk, *et al.*, Astrophys. J. **353**, 265 (1990).
6. G. A. Dulk, Annu. Rev. Astron. Astrophys. **23**, 169 (1985).
7. G. D. Fleĭshman and V. F. Mel’nikov, Usp. Fiz. Nauk **168**, 1265 (1998) [Phys. Usp. **41**, 1157 (1998)].
8. A. V. Ipatov and A.V. Stepanov, Vistas Astron. **41**, 203 (1997).
9. M. M. Katsova, Doctoral Dissertation in Phys.–Math. (Sternberg Astronomical Inst., Moscow, 1999).
10. D. Melrose, Lect. Notes Phys. **291**, 83 (1987).
11. D. Melrose, Space Sci. Rev. **68**, 159 (1994).
12. D. O’Neal, S. H. Saar, and J. E. Neff, Astrophys. J. Lett. **501**, L73 (1998).
13. G. H. J. van den Oord, Astron. Astrophys. **205**, 167 (1988).
14. R. Ottmann, Astron. Astrophys. **273**, 546 (1993).
15. J.-I. Sakai and C. de Jager, Space Sci. Rev. **77**, 1 (1996).
16. V. V. Sharma and L. Vlahos, Astrophys. J. **280**, 405 (1984).
17. S. L. Skinner, Astrophys. J. **368**, 272 (1991).

18. A. V. Stepanov, E. Furst, A. Kruger, *et al.*, Astron. Astrophys. **299**, 739 (1995).
19. A. V. Stepanov, B. Kliem, A. Kruger, *et al.*, Astrophys. J. **524**, 961 (1999).
20. F. M. Walter, D. M. Gibson, and G. S. Basri, Astrophys. J. **267**, 665 (1983).
21. S. M. White, Astron. Soc. Pac. Conf. Ser. **109**, 21 (1996).
22. S. M. White and E. Franciosini, Astrophys. J. **444**, 342 (1995).
23. N. E. White, R.A. Shafer, K. Horne, *et al.*, Astrophys. J. **350**, 776 (1990).
24. V. V. Zaitsev and A. V. Stepanov, Sol. Phys. **88**, 297 (1983).
25. V. V. Zheleznyakov, *Radiation in Astrophysical Plasma* (Yanus-K, Moscow, 1997).

Translated by Yu. Safronov

Astronomy Letters, Vol. 26, No. 11, 2000, pp. 743–749. Translated from Pis'ma v Astronomicheskiĭ Zhurnal, Vol. 26, No. 11, 2000, pp. 862–869.

An Axisymmetric Magnetohydrodynamic Model for the Interaction of the Solar Wind with the Local Interstellar Medium

D. B. Aleksashov, V. B. Baranov*, E. V. Barsky, and A. V. Myasnikov

Institute for Problems of Mechanics, Russian Academy of Sciences, pr. Vernadskogo 101, Moscow, 117526 Russia

Received May 17, 2000

Abstract—We numerically analyze a magnetohydrodynamic, steady-state model for the interaction of a spherically symmetric solar wind with a three-component local interstellar medium (LISM), which is composed of plasma, hydrogen atoms, and a magnetic field. The magnetic field is assumed to be parallel to the velocity in the LISM. In this case, the model is axisymmetric. We study the effects of magnetic field on the plasma-flow geometry and on the distribution of hydrogen-atom parameters. In particular, we show that the presence of hydrogen atoms does not affect the qualitative change in the shape of the bow shock, the heliopause, and the solar-wind shock with increasing strength of the interstellar magnetic field. The presence of a magnetic field in the LISM can strongly affect the parameters of the energetic hydrogen atoms originated in the solar wind, although its effect on the "hydrogen wall" observed with the GHRS instrument onboard the HST spacecraft (Linsky and Wood 1996) is marginal. *© 2000 MAIK "Nauka/Interperiodica".*

Key words: *Solar system, heliosphere, heliopause, shock waves, interstellar medium, solar wind, interstellar magnetic field, hydrogen atoms*

1. INTRODUCTION

At present, the kinetic gas-dynamical model proposed by Baranov *et al.* (1991) and developed by Baranov and Malama (1993, 1995, 1996) is widely used in studying the interaction of the solar wind (SW) with the local interstellar medium (LISM). In this model, the interaction between the SW and LISM plasma components was considered on the basis of Euler's equations with the "source terms" describing the effect of hydrogen atoms in terms of their ionization via charge exchange with protons, photoionization, and electron impact ionization followed by the "capture" of newly formed protons by plasma. Since the mean free path of hydrogen atoms for these processes is comparable to the scale size of the problem, for example, to the size of the heliopause separating the LISM plasma from the SW plasma, it is improper to describe the motion of hydrogen atoms in terms of the equations of continuum mechanics. Therefore, to determine the "source terms," Baranov and Malama (1993) calculated the trajectories of hydrogen atoms by the Monte Carlo method with the trajectory "splitting" proposed by Malama (1991) and used the method of global iterations proposed by Baranov *et al.* (1991) to solve the self-consistent problem. A proper allowance for the LISM hydrogen atoms in the model is of particular importance, because one of the most efficient experimental methods for studying interstellar gas parameters is currently the method based on an analysis of scattered and absorbed radiation in the $L\alpha$ hydrogen line.

The model was further improved by taking into account the effects of new physical phenomena found experimentally. Thus, for example, Myasnikov *et al.* (2000a, 2000b) considered a self-consistent model of the SW–LISM interaction that allowed for Galactic cosmic rays. However, an adequate magnetohydrodynamic (MHD) model that allows for the interstellar and interplanetary magnetic fields has not yet been constructed, although numerous attempts have been made to construct such a model. For example, Linde *et al.* (1998) calculated a three-dimensional MHD model but took into account the resonant charge exchange by using an improper hydrodynamic model for hydrogen atoms proposed by Baranov *et al.* (1981) and severely criticized by Baranov and Malama (1993). Myasnikov and Barsky (1997) and Barsky (1999) considered the kinematic approximation, in which gas-dynamical model parameters are used to calculate the magnetic field, but MHD effects in the gas-dynamical flow are disregarded. There are also many papers devoted to axi-

* E-mail address for contacts: baranov@ipmnet.ru

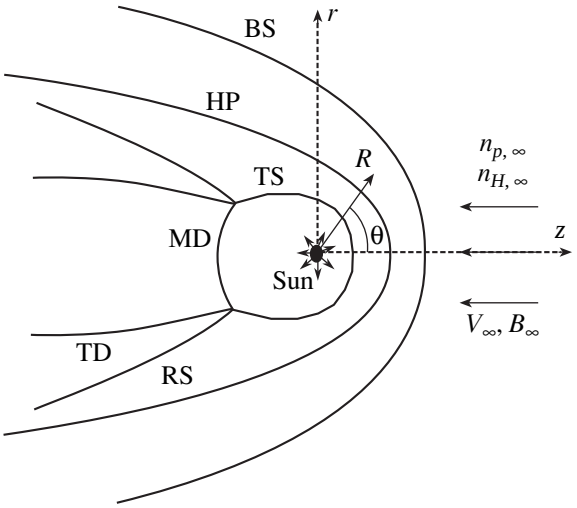

Fig. 1. The general pattern of flow produced by SW interaction with the LiSM. Here, *r* and *z* are the cylindrical coordinates; *R* is the heliocentric distance; θ is the polar angle; BS and TS are the bow and terminal shocks, respectively; HP is the heliophase; TD is the tangential discontinuity; RS is the reflected shock; and MD is the Mach disk.

symmetric (see, e.g., Fujimoto and Matsuda 1991; Baranov and Zaitsev 1995; Myasnikov 1997; Pogorelov and Semenov 1997) and three-dimensional (Pogorelov and Matsuda 1998) numerical MHD models ignoring the presence of hydrogen atoms in the LISM. Since the effect of LISM hydrogen atoms is significant, such papers are of purely theoretical interest and cannot form a basis for interpreting experimental results. Studying the effect of interstellar magnetic field on the penetration of hydrogen atoms from the LISM into the SW seems to be of crucial importance in interpreting measurements of hydrogen-atom parameters from spacecraft such as Ulysses, HST, SOHO, etc. (Izmodenov *et al.* 1999; Kirola *et al.* 1998; Lallement 1996; Gruntman 1993 and 1997). In particular, such an interpretation makes it possible to determine indirectly the plasma flow geometry, which seems of particular importance in view of the fact that its in-situ plasma measurements from the Voyager spacecraft are problematic in the near future, since, according to estimates, this spacecraft can leave the supersonic SW region only in several years.

The effect of interstellar magnetic field on the model is difficult to study theoretically primarily because its magnitude and direction in the LISM are virtually unknown. They can vary widely in models. Here, we present the first MHD model of the SW–LISM interaction, in which the interstellar magnetic field is taken into account within the framework of MHD equations with "source terms," and in which the trajectories of hydrogen atoms are calculated by the Monte Carlo method, as was done by Baranov *et al.* (1991) and Baranov and Malama (1993, 1995, 1996). For simplicity, we consider an axisymmetric model, in which the magnetic vector is assumed to be parallel to the interstellar-plasma velocity vector, and the SW is assumed to be spherically symmetric.

2. STATEMENT OF THE PROBLEM AND THE METHOD OF SOLUTION

Let us consider the interaction of a spherically symmetric solar wind with a uniform, translational flow of interstellar medium composed of plasma (electrons and protons), neutral hydrogen atoms, and magnetic field with the magnetic vector **B** parallel to the bulk velocity vector **v**. For a supersonic incoming flow, the emerging axisymmetric current is characterized by three surfaces of strong discontinuity (Fig. 1): a tangential discontinuity or heliopause (HP) separating the SW plasma from the LISM plasma, a bow shock (BS) through which the supersonic flow of interstellar plasma around the heliopause passes; and a terminal shock (TS) through which the SW decelerates. The plasma flow is assumed to be described in terms of steady-state MHD equations, which take the following form in cylindrical coordinates:

$$\frac{\partial \mathbf{D}}{\partial z} + \frac{\partial \mathbf{G}}{\partial r} = \mathbf{H} + \mathbf{Q}, \qquad (1)$$

where

$$\mathbf{D} = \begin{bmatrix} \rho v_z \\ p + \rho v_z^2 + \dfrac{B_r^2 - B_z^2}{8\pi} \\ \rho v_z v_r - \dfrac{B_r B_z}{4\pi} \\ v_z\left(E + p + \dfrac{B^2}{8\pi}\right) - \dfrac{B_z}{4\pi}\mathbf{v}\cdot\mathbf{B} \\ 0 \\ v_z B_r - v_r B_z \end{bmatrix},$$

$$\mathbf{G} = \begin{bmatrix} \rho v_r \\ \rho v_z v_r - \dfrac{B_r B_z}{4\pi} \\ p + \rho v_r^2 + \dfrac{B_z^2 - B_r^2}{8\pi} \\ v_r\left(E + p + \dfrac{B^2}{8\pi}\right) - \dfrac{B_r}{4\pi}\mathbf{v}\cdot\mathbf{B} \\ v_r B_z - v_z B_r \\ 0 \end{bmatrix},$$

$$\mathbf{H} = -\frac{1}{r}\begin{bmatrix} \rho v_r \\ \rho v_r v_z - \frac{B_r B_z}{4\pi} \\ \rho v_r^2 - \frac{B_r^2}{4\pi} \\ v_r\left(E + p + \frac{B^2}{8\pi}\right) - \frac{B_r}{4\pi}\mathbf{v}\cdot\mathbf{B} \\ v_r B_z - v_z B_r \\ 0 \end{bmatrix}, \quad \mathbf{Q} = \begin{bmatrix} Q_1 \\ Q_{2,z} \\ Q_{2,r} \\ Q_3 \\ 0 \\ 0 \end{bmatrix},$$

$$\mathbf{v} = (v_z, v_r), \quad \mathbf{B} = (B_z, B_r), \quad v = |\mathbf{v}|,$$

$$B = |\mathbf{B}| \text{ and } E = p/(\gamma - 1) + \rho v^2/2 + B^2/8\pi.$$

Here, ρ, $\mathbf{v}$, and p are the mass density, mean velocity, and pressure of the plasma, respectively; γ is the ratio of specific heat capacities; E is the internal energy; and $\mathbf{B}$ is the magnetic vector. The functions Q_1, $\mathbf{Q}_2$, and Q_3 on the right-hand sides of the equations of continuity, motion, and energy, respectively, represent the "source terms," which are related to the main process of resonant charge exchange between hydrogen atoms and protons (we also take into account the photoionization of hydrogen atoms and their electron impact ionization). Since these functions depend both on the plasma parameters and on the parameters of hydrogen atoms, it is necessary to add equations describing the motion of the neutral component. As was pointed out above, the neutral component cannot be described in terms of the continuum equations. Therefore, for the system of equations to be closed, the Boltzmann equation for the distribution function f_H of hydrogen atoms must be added [as was shown by Baranov *et al.* (1998), this function differs markedly from the local Maxwell function]:

$$\mathbf{w}_H \frac{\partial f_H(\mathbf{r}, \mathbf{w}_H)}{\partial \mathbf{r}} + \frac{\mathbf{F}}{m_H}\frac{\partial f_H(\mathbf{r}, \mathbf{w}_H)}{\partial \mathbf{w}_H}$$

$$= -f_H(\mathbf{r}, \mathbf{w}_H)\int |\mathbf{w}_H - \mathbf{w}_p|\sigma_{ex}^{HP} f_p(\mathbf{r}, \mathbf{w}_p)\mathbf{dw}_p + f_p(\mathbf{r}, \mathbf{w}_p)\int |\mathbf{w}_H^* - \mathbf{w}_p|\sigma_{ex}^{HP} \times f_H(\mathbf{r}, \mathbf{w}_H^*)\mathbf{dw}_H^* - \beta f_H(\mathbf{r}, \mathbf{w}_H), \quad (2)$$

where $\mathbf{w}_H$ and $\mathbf{w}_p$ are the hydrogen-atom and proton velocities, respectively; $\mathbf{r}$ is the particle radius vector; f_p is the proton distribution function (assumed to be the local Maxwell one); $\mathbf{F}$ is the sum of the forces of solar attraction and radiative repulsion; σ_{ex}^{HP} is the cross section for charge exchange between hydrogen atoms and protons; β is the sum of the rates of photoionization β_i and electron impact ionization β_{im}; and m_H is the hydrogen atomic mass.

The "source terms" can be written as

$$Q_1 = \beta n_H \quad (n_H = \int f_H d\mathbf{w}_H),$$

$$\mathbf{Q}_2 = n_H\int \beta \mathbf{w}_H f_H d\mathbf{w}_H + n_H\int\int \sigma_{ex}^{HP}|\mathbf{w}_H - \mathbf{w}_p| f_H f_p d\mathbf{w}_H d\mathbf{w}_p, \quad (3)$$

$$Q_3 = n_H\int \beta \frac{w_H^2}{2} f_H d\mathbf{w}_H + n_H\int\int \sigma_{ex}^{HP}\frac{w_H^2 - w_p^2}{2} f_H f_p \mathbf{dw}_H \mathbf{dw}_p.$$

In order to solve the system of equations (1)–(3), it is necessary to specify boundary conditions for the plasma velocity V, its temperature (or the Mach number M), and proton (electron) number density n_p in the Earth's orbit and in the incoming undisturbed LISM flow. As the boundary conditions for f_H in the undisturbed LISM, we take the Maxwell distribution with a given density $n_{H,\infty}$ and with the temperature and velocity equal to the plasma ones.

In solving the formulated gas-kinetic problem, we used the method of global iterations proposed by Baranov *et al.* (1991) and implemented by Baranov and Malama (1993, 1995, 1996). In the first iteration, the distributions of MHD parameters in the interaction region are calculated by the relaxation method by solving unsteady-state analogs of Eqs. (1) with zero source terms (3). Since the applied numerical technique (Myasnikov 1997) makes it possible to roughly distinguish the main MHD discontinuities obtained during the first iteration, the flow parameters can be directly used to solve Eq. (2) by the Monte Carlo method with trajectory splitting (Malama 1991). The calculated source terms (3) are used to solve Eqs. (1) in the next iteration. The iteration process terminates when the distributions of the plasma, hydrogen-atom, and magnetic-field parameters cease to depend markedly on the iteration number.

3. RESULTS OF CALCULATIONS AND THEIR ANALYSIS

In order to solve the stated problem, we fix the density of interstellar hydrogen atoms, 0.2 cm^{-3} (Gloekler *et al.* 1997), and take the parameters of the undisturbed SW and LISM plasma to be

$$V_E = 450 \text{ km/s}, \quad n_{p,E} = \rho_E/m_H = 7 \text{ cm}^{-3},$$

$$M_E = V_E/\sqrt{2kT_E/m_H} = 10,$$

$$V_\infty = 25 \text{ km/s}, \quad n_{p,\infty} = \rho_\infty/m_H = 0.07 \text{ cm}^{-3},$$

$$M_\infty = V_\infty/\sqrt{2kT_\infty/m_H} = 2.$$

Here, the subscripts E and ∞ refer to the Earth's orbit and the undisturbed LISM, respectively; T is the temperature, and k is the Boltzmann constant. We also fixed the adiabatic index $\gamma = 5/3$ and the ratio of the forces of radiation pressure and solar gravitation $\mu = 0.75$. The effect of the interstellar magnetic field was taken into account by varying the Alfvén Mach number $M_{A,\infty} = V_\infty\sqrt{4\pi\rho_\infty}/B_\infty$ over the range $\infty \le M_{A,\infty} \le 0.9$.

3.1. Effects of Magnetic Field on the Flow Geometry

Figure 2 shows the positions of the shocks (BS and TS) and the tangential discontinuity (HP) at various Alfvén Mach numbers in the undisturbed LISM. It is easy to see that the bow shock straightens out with decreasing Alfvén Mach number (increasing magnetic-field strength in the LISM). It approaches the Sun near the symmetry axis, but recedes from it on the flanks. By contrast, the nose of the heliopause recedes from the Sun due to the tension of magnetic field lines, while the heliopause in its wings approaches the Sun under magnetic pressure [the effect of heliopause stretching was obtained by Baranov and Krasnobaev (1971) in the Newtonian approximation of a thin layer]. The pattern of change in the bow shock and in the heliopause causes the region of the most effective "filtration" of interstellar hydrogen atoms (the region between BS and HP), where the primary hydrogen atoms are lost most intensely due to their charge exchange with interstellar protons, to decrease along the symmetry axis approximately by 50 AU, i.e., by almost 30% (see Fig. 2), as the magnetic field increases from zero to $B_\infty = 3.5 \times 10^{-6}$ G ($M_{A,\infty} = 0.9$).

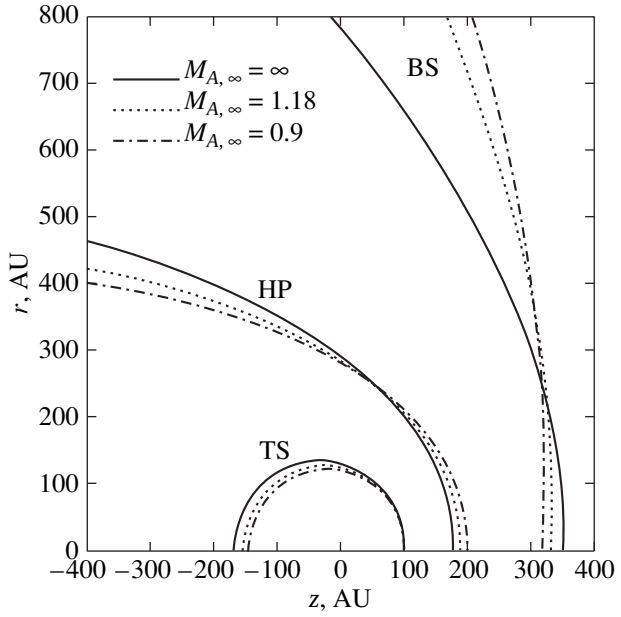

Fig. 2. Positions of the bow shock, the heliopause, and the terminal shock for various Alfvén–Mach numbers.

The fact that the heliopause approaches the Sun on the flanks, in turn, results in a decrease in the detachment of the terminal shock at $\theta = \pi$. Since the detachment of the terminal shock at $\theta = 0$ is independent of the magnetic-field strength (in the absence of hydrogen atoms, this fact can be easily obtained analytically by using the Bernoulli integral and relationships at the shocks), the terminal shock tends to become spherical in shape with increasing magnetic field. Thus, the pattern of change in the flow geometry with increasing magnetic field at $n_{H,\infty} \neq 0$ qualitatively agrees with the results of Baranov and Zaitsev (1995) and Myasnikov (1997).

Studies of the effects of magnetic field on the structure of the region of interaction between the SW and the LISM indicate that, in the absence of physical effects related to hydrogen atoms, an increase in the magnetic field results in the destruction of the complex flow structure in the tail region associated with the formation of a Mach disk (MD) and a triple point or a point of intersection of the Mach disk, the tangential discontinuity (TD), and the reflected shock (RS) (see Fig. 1). Resonant charge exchange produces the same effect, as was shown by Baranov and Malama (1993). Thus, the effects of both neutral hydrogen atoms and the interstellar magnetic field lead to the flow in the region between the terminal shock and the heliopause being subsonic in all calculations.

The reduction in the influence of magnetic field on the structure of the region of interaction between the SW and the LISM plasma with increasing $n_{H,\infty}$ is an important but predictable effect (Myasnikov and Barsky 1997). In particular, at $n_{H,\infty} = 0.2$ cm^{-3} and $M_{A,\infty} = 0.9$, there is a bow shock in the flow whose detachment on the symmetry axis differs only slightly from the case with $n_{H,\infty} = 0.2$ cm^{-3} and $M_{A,\infty} = \infty$ (Fig. 2). At the same time, the calculations performed at $n_{H,\infty} = 0$ and $M_{A,\infty} = 0.9$ (Myasnikov 1997) indicate that the solution falls within the ellipticity region of Eqs. (1), which results in the disappearance of the bow shock. Baranov and Zaitsev (1995) predicted the possibility of such an effect.

3.2. Effects of Magnetic Field on the Characteristics of Hydrogen Atoms

Resonant charge exchange of interstellar hydrogen atoms gives rise several kinds of hydrogen atoms with different characteristics, depending on the region of their production. The high-energy hydrogen atoms produced by charge exchange of SW protons before and after their passage through the terminal shock belong to kinds 1 and 2, respectively. Clearly, kind-1 hydrogen atoms must have a high mean radial velocity comparable to the supersonic SW velocity, while kind-2 hydrogen atoms must have a high thermal velocity deter-

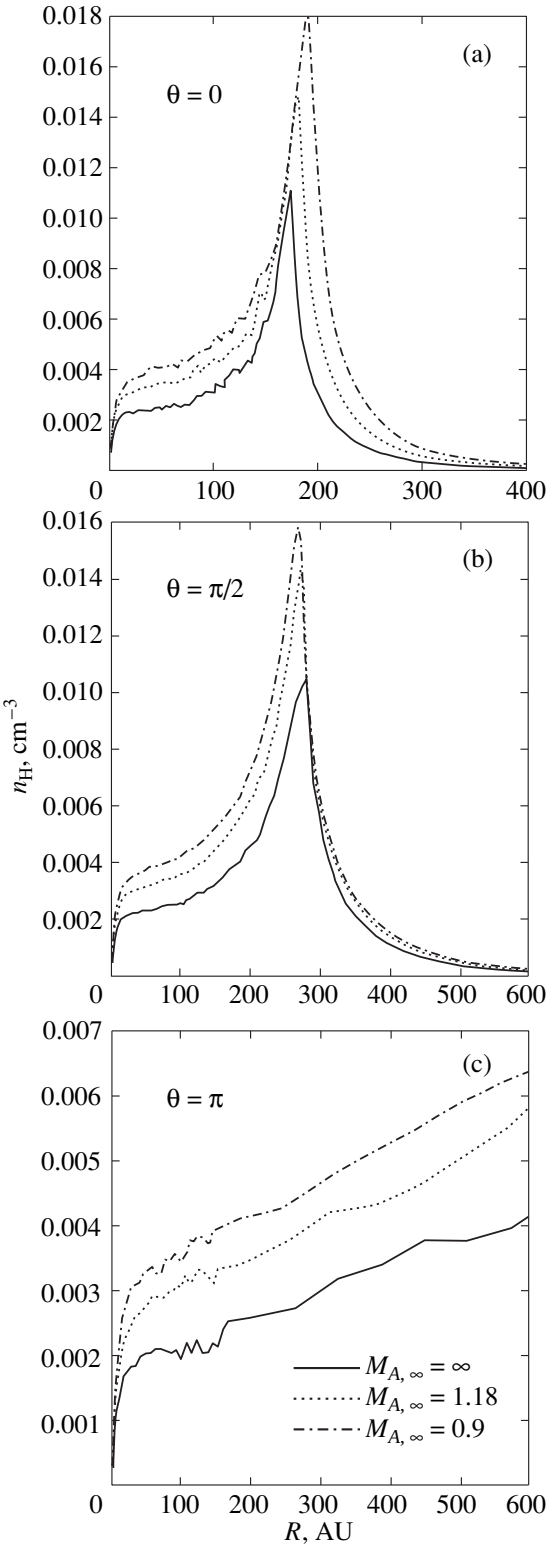

Fig. 3. The density distribution of energetic hydrogen atoms produced behind the terminal shock (kind 2) for θ = 0, π/2, and π (a, b, c, respectively).

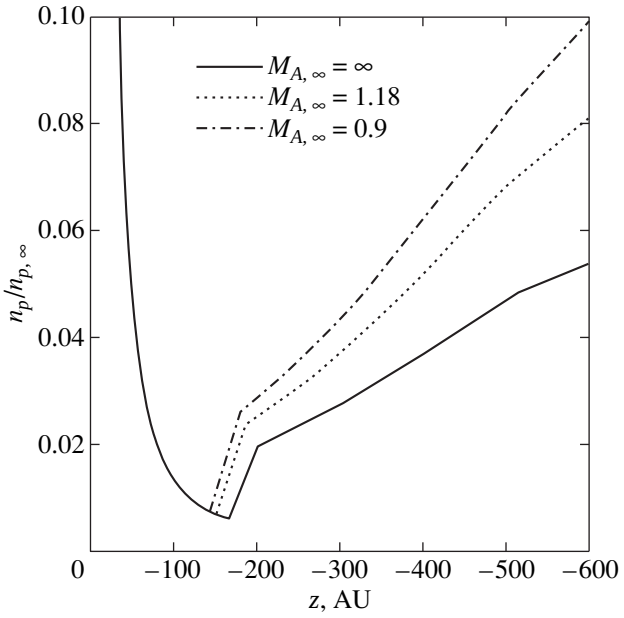

Fig. 4. The proton density distribution for θ = π at various Alfvén–Mach numbers.

mined by the SW proton temperature behind the terminal shock. The secondary hydrogen atoms produced by charge exchange of LISM atoms with inherent protons belong to kind 3, while the primary LISM atoms that underwent no charge exchange belong to kind-4. Kind-3 and 4 atoms have the LISM particle energy and are detected at a wavelength of 1216 Å in absorption lines from the nearest stars (Linsky and Wood 1996) and by analyzing scattered solar radiation (Bertaux and Blamont 1971; Thomas and Krassa 1971; Kirola *et al.* 1998; Lallement 1996). As for the hydrogen atoms with the SW particle energy (kinds 1 and 2), their flows can be measured from a distance of 1 AU by direct methods based on the technique proposed by Gruntman (1993, 1997).

Our calculations indicate that the density distribution of kind-1 hydrogen atoms is virtually unchanged at all polar angles $0 \le \theta \le \pi$ and over the entire assumed range of $M_{A,\infty}$. In particular, for $M_{A,\infty} = \infty$, these results closely agree with those obtained by Baranov *et al.* (1998). The magnetic field has the strongest effect on the density distribution of kind-2 hydrogen atoms presented in Fig. 3 for θ = 0 (in the "leeward" direction), θ = π/2 (perpendicular to the leeward direction), and θ = π (in the tail region). The physical causes of an almost a factor of 1.5 rise in the density of kind-2 hydrogen atoms as the interstellar magnetic field increases from zero to 3.5×10^{-6} G differ in different regions. In the leeward direction, the rise can be caused by an increase in the thickness of the region between HP and TS responsible for the production of kind-2 hydrogen atoms. In the tail region, the increase in the number of kind-2 hydrogen atoms is facilitated by an increase in the number of thermalized SW protons behind the terminal shock with growing magnetic field as it approaches the Sun (see Figs. 2 and 4).

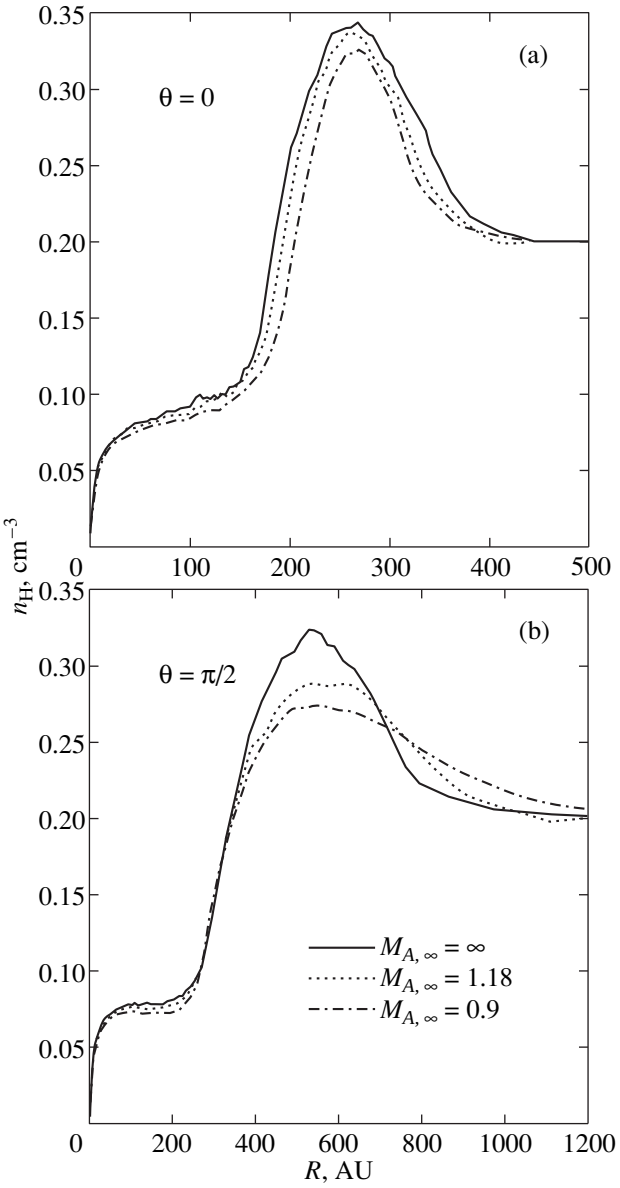

Fig. 5. The density distribution of hydrogen atoms produced in the LiSM (kind 3) at $\theta = 0$ (a) and $\theta = \pi/2$ (b) for various Alfvén–Mach numbers.

The effect of an increase in the number of kind-2 hydrogen atoms with growing interstellar magnetic field can be useful in their direct detection, because the efficiency of the method proposed by Gruntman (1993, 1997) is determined by the sensitivity of the instruments measuring the fluxes of these particles.

The nonmonotic behavior of the density of kind-3 hydrogen atoms was first theoretically predicted by Baranov *et al.* (1991). In the literature, this effect was called a *hydrogen wall*. The formation of a hydrogen wall is physically related to the production of secondary hydrogen atoms (kind 3) via charge exchange of primary (kind 4) atoms with almost stagnated protons near the heliopause (that is why the maximum of the hydrogen wall is located in the immediate vicinity of the heliopause). Interpretation of the experimental data on the absorption of $L\alpha$ emission from αCen obtained with the GHRS instrument onboard the HST spacecraft led Linsky and Wood (1996) to conclude that the theoretically predicted hydrogen wall was discovered experimentally. This conclusion was based on the fact that the absorption spectra obtained could be explained only by introducing a hydrogen wall. Therefore, it seems to be important to study the dependence of the position and height of the hydrogen wall on various physical factors, in particular, on the interstellar magnetic field.

We see from Fig. 5 that the interstellar magnetic field parallel to the LISM velocity vector changes the hydrogen-wall parameters only slightly. In particular, the hydrogen-wall height decreases approximately by 10% as the magnetic field changes from zero to 3.5×10^{-6} G; this wall recedes from the Sun together with the heliopause. The decrease in the height of the hydrogen wall is slightly larger in the direction perpendicular to the symmetry axis, as we see from Fig. 5b. The decrease in the hydrogen-wall height near the symmetry axis with increasing magnetic field is clearly attributable to a decrease in the filter thickness in this region. The same effect in the perpendicular direction can be explained by a decrease in the density of LISM protons in the bow-shock wings (oblique shock) compared to the direct shock near the symmetry axis. In both cases, the number of secondary hydrogen atoms responsible for the nonmonotic behavior of the density of hydrogen atoms decreases. In our view, a marginal effect of the magnetic field on the position and height of the hydrogen wall cannot change its interpretation on the basis of analysis of absorption spectra in the $L\alpha$ line (Linsky and Wood 1996). An interpretation of the observed HST absorption spectrum in this line along a line of sight passing through the heliospheric tail (toward Sirius) shows (Izmodenov *et al.* 1999) that the spectrum can be explained by taking into account absorption by kind-2 hydrogen atoms, because there is no hydrogen wall in the tail region.

4. CONCLUSION

(1) We have numerically constructed a steady-state MHD model for the SW interaction with a partially ionized, magnetized LISM for the first time. In this model, we use the kinetic gas-dynamical approach proposed by Baranov and Malama (1993), in which the plasma is described by MHD equations, while the hydrogen-atom parameters are determined by the Monte Carlo method with trajectory splitting proposed by Malama (1991). The magnetic vector is assumed to be parallel to the plasma velocity vector, which makes it possible to consider the problem in terms of axial symmetry.

(2) We have shown that the pattern of change in the flow geometry (the shape of the shocks and tangential discontinuity) with increasing interstellar magnetic

field qualitatively agrees with that calculated by Baranov and Zaitsev (1995) in the absence of neutral atoms and in the range of polar angles $0 \le \theta \le \pi/2$. Our calculation of the flow at $0 \le \theta \le \pi$ by the numerical method proposed by Myasnikov (1997) indicates that the magnetic field, as well as neutral atoms (Baranov and Malama 1993), destroys the complex flow pattern to form a triple point and a Mach disk. The terminal shock becomes oval, approaching a sphere with increasing magnetic field, while the flow between the heliopause and the terminal shock becomes subsonic.

(3) The magnetic field has a fairly strong effect on the energetic hydrogen atoms produced by charge exchange of LISM hydrogen atoms with thermalized SW protons behind the terminal shock (kind-2). An almost a factor of 1.5 increase in the density of these atoms with increasing magnetic field can relax the requirement on the sensitivity of instruments for their detection (Gruntman 1993, 1997).

(4) A marginal (about 10%) change in the parameters of the hydrogen wall theoretically discovered by Baranov *et al.* (1991) near the heliopause cannot affect the conclusions reached by Linsky and Wood (1996) that this wall was experimentally discovered with the GHRS instrument onboard the HST spacecraft.

ACKNOWLEDGMENTS

This study was supported by the Russian Foundation for Basic Research (project nos. 98-01-00 955, 99-02-04 025, and 98-02-16 759) and the INTAS–CNES Foundation (grant no. 97-512).

REFERENCES

1. V. B. Baranov and K. V. Krasnobaev, Kosm. Issled. **9**, 620 (1971).
2. V. B. Baranov and Yu. G. Malama, J. Geophys. Res. **98**, 15 157 (1993).
3. V. B. Baranov and Yu. G. Malama, J. Geophys. Res. **100**, 14 755 (1995).
4. V. B. Baranov and Yu. G. Malama, Space Sci. Rev. **78**, 305 (1996).
5. V. B. Baranov and N. A. Zaitsev, Astron. Astrophys. **304**, 631 (1995).
6. V. B. Baranov, M. K. Ermakov, and M. G. Lebedev, Pis'ma Astron. Zh. **7**, 372 (1981) [Sov. Astron. Lett. **7**, 206 (1981)].
7. V. B. Baranov, M. G. Lebedev, and Yu. G. Malama, Astrophys. J. **375**, 347 (1991).
8. V. B. Baranov, V. V. Izmodenov, and Yu. G. Malama, J. Geophys. Res. **103**, 9575 (1998).
9. E. V. Barsky, Pis'ma Astron. Zh. **25**, 942 (1999) [Astron. Lett. **25**, 825 (1999)].
10. J.-L. Bertaux and J. Blamont, Astron. Astrophys. **11**, 200 (1971).
11. Y. Fujimoto and T. Matsuda, Preprint No. KUGD91-2 (Kobe Univ., Japan, 1991).
12. G. L. Gloekler, L. A. Fisk, and J. Geiss, Nature **386**, 374 (1997).
13. M. A. Gruntman, Planet. Space Sci. **41**, 307 (1993).
14. M. A. Gruntman, Rev. Sci. Instrum. **68**, 3617 (1997).
15. V. V. Izmodenov, R. Lallement, and Yu. G. Malama, Astron. Astrophys. **342**, L13 (1999).
16. E. Kirola, T. Summanen, W. Schmidt, *et al.*, J. Geophys. Res. **103**, 14 523 (1998).
17. R. Lallement, Space Sci. Rev. **78**, 361 (1996).
18. T. Linde, T. I. Gombosi, P. L. Roe, *et al.*, J. Geophys. Res. **103**, 1889 (1998).
19. J. L. Linsky and B. E. Wood, Astrophys. J. **463**, 254 (1996).
20. Yu. G. Malama, Astrophys. Space Sci. **176**, 21 (1991).
21. A. V. Myasnikov, Preprint No. 585, IPM RAN (Institute for Problems of Mechanics, Russian Academy of Sciences, 1997).
22. A. V. Myasnikov and E. V. Barsky, Preprint No. 584, IPM RAN (Institute for Problems of Mechanics, Russian Academy of Sciences, 1997).
23. A. V. Myasnikov, D. B. Aleksashov, V. V. Izmodenov, and S. V. Chalov, J. Geophys. Res. **105**, 5179 (2000a).
24. A. V. Myasnikov, D. B. Aleksashov, V. V. Izmodenov, and S. V. Chalov, J. Geophys. Res. **105**, 5167 (2000b).
25. N. V. Pogorelov and A. Yu. Semenov, Astron. Astrophys. **321**, 330 (1997).
26. N. V. Pogorelov and T. Matsuda, J. Geophys. Res. **103**, 237 (1998).
27. G. Thomas and R. Krassa, Astron. Astrophys. **11**, 218 (1971).

Translated by Yu. Safronov

Astronomy Letters, Vol. 26, No. 11, 2000, pp. 750–755. Translated from Pis'ma v Astronomicheskiĭ Zhurnal, Vol. 26, No. 11, 2000, pp. 870–875.

A Simple Analytic Model of Reconnection in a High-Temperature Turbulent Sheet

A. V. Oreshina* and B. V. Somov

Sternberg Astronomical Institute, Universitetskiĭ pr. 13, Moscow, 119899 Russia

Received March 30, 2000

Abstract—We present a simple model of high-temperature ($T \geq 10^8$ K) turbulent current sheets forming in magnetic-reconnection regions on the Sun. The model is based on an empirical formula by de Kluiver *et al.* (1991) for turbulent plasma conductivity and is apparently valid over a wide range of physical conditions. A comparison of the new results with known test calculations suggests agreement between the theoretical and empirical approaches to calculating the anomalous conductivity in turbulent plasma. The energy release in current sheets is powerful enough for flares, coronal transients, and coronal mass ejections to be interpreted. *© 2000 MAIK "Nauka/Interperiodica".*

Key words: *Sun*

INTRODUCTION

Models of reconnection in the solar atmosphere can be separated into two groups: global and local ones (Kosugi and Somov 1998). The global models, stationary or nonstationary, two- or three-dimensional, describe active regions or even complexes of activity on the Sun in a particular approximation (Gorbachev and Somov 1990; Demoulin *et al.* 1993; Bagala *et al.* 1995; Longcope and Silva 1998; Pevtsov and Longcope 1998; Podgorny and Podgorny 1998; Moon *et al.* 1999; Somov *et al.* 1999). The main advantage of the global models is a direct comparison between the results of computations and the observed large-scale pattern of the phenomenon. For example, the so-called "topological model" of a solar flare (Gorbachev and Somov 1989, 1990; Somov 1992) (i) shows that the flare energy is released during reconnection on the separator which has a definite location in the corona relative to sunspots, and (ii) allows us to determine the shape of X-ray coronal loops and the shape of flare ribbons in the chromosphere where these ribbons are best seen in the Hα line.

Despite this indisputable advantage, the global models generally have purely illustrative value. Low space resolution of the computational grid does not allow one to compute the reconnection region: a thin current sheet (Sweet 1958; Parker 1963; Syrovatskiĭ 1962, 1966) or Petschek's system of shock waves (Petschek 1964). The true plasma transport coefficients are inevitably replaced by some effective (to be more precise, fictitious) conductivity, heat conduction, and viscosity. Thus, the global models are not internally self-consistent.

By contrast, the local models are intended to study the actual physics of magnetic reconnection with minimal allowance for external factors. The models directly describing a current sheet (Sweet 1958; Parker 1963; Syrovatskiĭ 1966; Imshennik and Syrovatskii, 1967) belong to this group. The simplest local models consider the reconnection region as a whole without allowance for its internal structure. The obvious advantage in simplicity and clarity allows more attention to be given to a detailed description of the physical processes in the reconnection region.

The model we propose belongs to this group. In general, it is similar to the "single-temperature model" of a high-temperature turbulent current sheet (HTCS) [see subsection 3.1 in Somov *et al.* (1987); see subsection 3.3.1 in the book by Somov (1992) for more details]. Two fundamental peculiarities constitute an exception.

First, the anomalous plasma conductivity σ in the new model is determined by an empirical low with a wide range of applicability (de Kluiver *et al.* 1991):

$$\frac{\sigma}{\sigma_{\rm cl}} \approx 0.1\frac{E_{\rm cr}}{E}. \qquad (1)$$

Here, $\sigma_{\rm cl} = \sigma_0 T^{3/2}$ is the classical plasma conductivity, $\sigma_0 = 1.44 \times 10^8/\ln\Lambda$, $\ln\Lambda = \ln[9.44 \times 10^6 T/n^{1/2}]$ is the Coulomb logarithm, and Dreicer's critical field is

$$E_{\rm cr} = 2.13 \times 10^{-12}\frac{n}{T}\ln\Lambda \ \text{(CGSE units)}. \qquad (2)$$

Relation (1) is valid in the range of electric fields $10^{-2} \leq E/E_{\rm cr} \leq 10^5$; the conductivity ratio $\sigma/\sigma_{\rm cl}$ varies from 10 to 10^{-6}.

* E-mail address for contacts: avo@sai.msu.ru

1063-7737/00/2611-0750$20.00 © 2000 MAIK "Nauka/Interperiodica"

Equations (1) and (2) yield

$$\sigma = 2.98 \times 10^{-5} \frac{T^{1/2} n}{E} \ (\mathrm{s}^{-1}). \quad (3)$$

Thus, instead of complex theoretical calculations of the anomalous conductivity in various plasma-turbulence regimes, as was done in the test model (Somov 1992), we take the empirical simple formula (3).

Second, in the new model, we pose the question as to the heat flux from the HTCS more accurately.

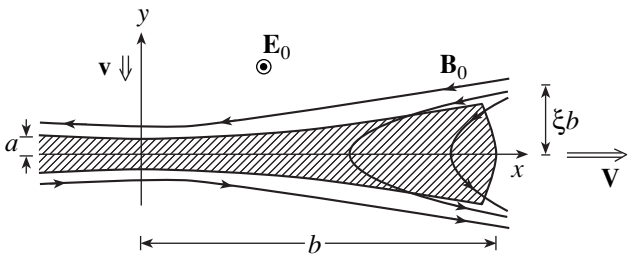

A schematic representation of the reconnecting current sheet.

1. THE PROBLEM OF CURRENT-SHEET PARAMETERS

In a reconnecting current sheet (see the figure), magnetic field lines flow in together with plasma at a low velocity v along the y direction, reconnect, and subsequently outflow at a high velocity V along the x direction. Let a and b be the half-thickness and half-width of the sheet, n and T be the plasma number density and temperature inside it. The plasma number density n_0 and temperature T_0 outside the sheet, the magnetic-field gradient h_0 in the vicinity of the zero line, the electric-field strength E_0, and the relative transverse component $\xi \equiv B_y/B_0$, where B_0 is the magnetic field outside the sheet, are assumed to be known. A more self-consistent formulation of the problem of a thin reconnecting sheet is possible, but it is more complex from a mathematical point of view [see subsection 3.4.3 in the book by Somov (1992)].

Consider a thin ($a \ll b$), nonneutral ($a/b \ll \xi$) current sheet with a low transverse magnetic field ($\xi \ll 1$) in the strong-field approximation [see Somov (1994); see more general formulations of the reconnection problem ibidem]. We assume the electron temperature to exceed significantly the ion one in the HTCS:

$$T_\mathrm{e} \gg T_\mathrm{i}, \quad T \equiv T_\mathrm{e}. \quad (4)$$

As in the test model, we rewrite the laws of mass and momentum conservation, Ohm's law, and the law of energy conservation as order-of-magnitude relations containing only the main terms:

$$n_0 v b = n V \xi b, \quad (5)$$

$$\frac{B_0^2}{8\pi} = n k_\mathrm{B} T, \quad (6)$$

$$n k_\mathrm{B} T = \frac{1}{2} M n V^2, \quad (7)$$

$$\frac{c B_0}{4\pi a} = \sigma E_0, \quad (8)$$

$$\mathscr{E}_\mathrm{mag}^\mathrm{in} = \mathscr{E}_\mathrm{th}^\mathrm{out} + K^\mathrm{out} + C_\parallel, \quad (9)$$

where c is the speed of light, k_B is the Boltzmann constant, and M is the ion mass. In Eq. (5), $v = cE_0/B_0$ is the plasma drift velocity into the sheet; the effective scale size of plasma outflow from the sheet is determined by ξb. As follows from Eqs. (6) and (7), the outflow velocity is

$$V = \frac{B_0}{\sqrt{4\pi M n}}. \quad (10)$$

The field near the sheet can be estimated as follows (Syrovatskiĭ 1974):

$$B_0 = h_0 b. \quad (11)$$

The energy equation (9) includes the magnetic enthalpy flux into the sheet

$$\mathscr{E}_\mathrm{mag}^\mathrm{in} = \frac{B_0^2}{4\pi} v b, \quad (12)$$

which matches the Joule heating of the current sheet $(j^2/\sigma)ab$ under conditions of the anomalous conductivity (3).

The thermal enthalpy flux from the sheet along magnetic field lines is

$$\mathscr{E}_\mathrm{th}^\mathrm{out} = \left(\frac{5}{2} n_\mathrm{e} k_\mathrm{B} T_\mathrm{e} + \frac{5}{2} n_\mathrm{i} k_\mathrm{B} T_\mathrm{i}\right) V \xi b \approx \frac{5}{2} n k_\mathrm{B} T V \xi b, \quad (13)$$

where we took into account the fact that $n_\mathrm{i} = n_\mathrm{e} \equiv n$ and $T_\mathrm{i} \ll T_\mathrm{e} \equiv T$.

The kinetic energy flux of the plasma outflowing from the sheet is

$$K^\mathrm{out} = \left(\frac{1}{2} M n V^2 + \frac{1}{2} m n V^2\right) V \xi b \approx \frac{1}{2} M n V^2 V \xi b, \quad (14)$$

because the ion mass M exceeds significantly the electron mass m.

The heat flux along magnetic field lines can be represented as (Somov 1994; Somov *et al.* 1987)

$$C_\parallel = f(\theta) \frac{n (k_\mathrm{B} T)^{3/2}}{M^{1/2}} \xi b, \quad (15)$$

where $\theta = T_\mathrm{e}/T_\mathrm{i}$, and

$$f(\theta) = \begin{cases} \frac{1}{4}\left(\frac{M}{m}\right)^{1/2}, \text{ if } 1 \le \theta \le 8.1 \\ \left(1+\frac{3}{\theta}\right)^{1/2} + \left(\frac{M}{m}\right)^{1/2} \theta^{3/2}\left[\left(1+\frac{3}{\theta}\right)^{1/2} - \frac{1}{\theta^{1/2}}\right] \\ \times \exp\left[-\frac{2(\theta+3)}{5}\right], \text{ if } \theta < 1 \text{ or } \theta > 8.1. \end{cases} \quad (16)$$

The upper and lower expressions in Eq. (16) describe the saturated and anomalous heat fluxes, respectively.

Equation (9) does not include the thermal enthalpy flux into the sheet

$$\mathscr{E}_{\text{th}}^{\text{in}} = (5n_0 k_B T_0) v b \ll \mathscr{E}_{\text{th}}^{\text{out}}, \quad (17)$$

because $T_0 \ll T$, and the kinetic energy flux of the plasma inflowing into the sheet

$$K^{\text{in}} = \left(\frac{1}{2} M n_0 v^2 + \frac{1}{2} m n_0 v^2\right) v b \ll K^{\text{out}}, \quad (18)$$

because $v^2 \ll V^2$ in the strong-field approximation. The magnetic enthalpy flux from the sheet

$$\mathscr{E}_{\text{mag}}^{\text{out}} = \frac{B_y^2}{4\pi} V \xi b \ll \mathscr{E}_{\text{mag}}^{\text{in}}, \quad (19)$$

is also negligible, because $B_y^2 \ll B_0^2$. Moreover, as was shown in the test model, the following factors do not contribute to the energy balance of the HTCS under the solar-corona conditions: the energy exchange between electrons and ions through Coulomb collisions, the heat flux across the magnetic field, and the energy losses by radiation.

Recall that the heat flux in the test model was considered as the saturated one, which takes place at $1 \le \theta \le 8.1$; this satisfies inequality (4) only approximately. We will leave the same flux in Section 2

$$C_{\parallel} = \frac{n(k_B T)^{3/2}}{4m^{1/2}} \xi b, \quad (20)$$

in order to clearly demonstrate the effect of the new formula (3) for calculating the turbulent conductivity

$$\sigma = \sigma_1 \frac{T^{1/2} n}{E_0} \ (\text{c}^{-1}), \text{ where } \sigma_1 = 2.98 \times 10^{-5}. \quad (21)$$

In section (3), we take the anomalous heat flux corresponding to $\theta \gg 1$. Thus, closer agreement will be reached between the initial assumptions and the specified functions; in addition, the question as to the sensitivity of the HTCS model to the heat flux will be solved.

2. HTCS WITH TURBULENT CONDUCTIVITY

First, let us determine the unknown quantities a, b, n, and V from Eqs. (5)–(8) by considering the sheet temperature T as an unknown parameter. We obtain the following algebraic formulas:

$$a = 2^{1/6} \pi^{-1/3} k_B^{5/6} M^{-1/6} c^{2/3} \sigma_1^{-1} [n_0^{-1/3} E_0^{-1/3} \xi^{1/3}] T^{1/3}, \quad (22)$$

$$b = 2^{5/6} \pi^{1/3} k_B^{1/6} M^{1/6} c^{1/3} [n_0^{1/3} E_0^{1/3} h_0^{-1} \xi^{-1/3}] T^{1/6}, \quad (23)$$

$$n = 2^{-4/3} \pi^{-1/3} k_B^{-2/3} M^{1/3} c^{2/3} [n_0^{2/3} E_0^{2/3} \xi^{-2/3}] T^{-2/3}, \quad (24)$$

$$V = 2^{1/2} k_B^{1/2} M^{-1/2} T^{1/2}. \quad (25)$$

We now derive the sheet temperature as a function of n_0, h_0, E_0, and ξ from Eq. (9). For this purpose, we rewrite Eq. (9) as

$$\frac{B_0^2}{4\pi} v b = \frac{1}{2}(MnV^2 + 5nk_B T) V \xi b + \frac{n(k_B T)^{3/2}}{4m^{1/2}} \xi b. \quad (26)$$

Transform the terms on the right-hand side:

$$\frac{1}{2}(MnV^2 + 5nk_B T) V \xi b = \frac{7}{4} \frac{n_0}{n} \frac{B_0^2}{4\pi} v b, \quad (27)$$

$$\frac{n(k_B T)^{3/2}}{4m^{1/2}} \xi b = \frac{1}{8}\left(\frac{M}{2m}\right)^{1/2} \frac{n_0}{n} \frac{B_0^2}{4\pi} v b. \quad (28)$$

Substituting (27) and (28) in Eq. (26) yields

$$\frac{n}{n_0} = \frac{7}{4} + \frac{1}{8}\left(\frac{M}{2m}\right)^{1/2} \approx 5.54. \quad (29)$$

Hence, using Eq. (24), we obtain the temperature

$$T = \frac{2}{[7 + \sqrt{M/(8m)}]^{3/2}} \pi^{-1/2} k_B^{-1} M^{1/2} c [n_0^{-1/2} E_0 \xi^{-1}]. \quad (30)$$

Thus, formulas (29), (30), (22), (23), and (25) determine the current-sheet characteristics n, T, a, b, and V via the external parameters n_0, E_0, h_0, and the dimensionless parameter ξ. Apart from the above HTCS parameters, we also calculated the power released in the current sheet per unit sheet length (perpendicular to the figure plane):

$$\frac{P}{l} = \frac{B_0^2}{4\pi} v 4b = \frac{1}{\pi} c E_0 h_0 b^2. \quad (31)$$

For comparison, Tables 1 and 2 give estimates of the HTCS parameters, respectively, in the well-studied test model and in the new model, i.e., with the new empirical formula for the anomalous turbulent-plasma conductivity inside the sheet. The input data in Table 2 are, of course, the same as those in Table 1.

As we see from the tables, the previous and new results differ marginally. There are discrepancies only

Table 1. Test model for a HTCS

	1	2	3	4
Input parameters:				
n_0, cm^{-3}	10^{10}	10^{10}	10^{10}	10^{10}
E_0, CGSE units	3.3×10^{-4}	1.3×10^{-3}	2.3×10^{-3}	2.3×10^{-2}
h_0, G/cm	1.8×10^{-6}	1.2×10^{-7}	4.8×10^{-7}	1.5×10^{-7}
ξ	10^{-3}	10^{-2}	10^{-3}	10^{-2}
Computed quantities:				
T, K	1.0×10^{7}	4.0×10^{6}	7.0×10^{7}	7.0×10^{7}
n, cm^{-3}	5.5×10^{10}	5.5×10^{10}	5.5×10^{10}	5.5×10^{10}
a, cm	98	39	60	20
b, cm	2.4×10^{7}	2.3×10^{8}	2.4×10^{8}	7.7×10^{8}
V, cm/s	4.1×10^{7}	2.5×10^{7}	1.1×10^{8}	1.1×10^{8}
σ, s^{-1}	3.2×10^{12}	1.3×10^{12}	2.0×10^{12}	6.3×10^{11}
E_0/E_{cr}	1.4×10^{3}	2.3×10^{3}	6.3×10^{4}	6.3×10^{5}
$C_\parallel$, erg/(cm s)	5.8×10^{14}	1.3×10^{16}	1.0×10^{17}	3.1×10^{18}
P/l, erg/(cm s)	3.4×10^{15}	7.9×10^{16}	6.1×10^{17}	2.0×10^{19}

in the estimates of the conductivity and, as a consequence, of the sheet thickness; they do not exceed a factor of 5. This suggests agreement between the two different approaches to calculating the anomalous plasma conductivity: the theoretical one used in test models (Somov 1992) and the empirical one described by de Kluiver *et al.* (1991).

Note that, in the fourth case, E_0/E_{cr} proves to be outside the interval on which relation (1) is defined. Nevertheless, good agreement between the test and new results apparently points to the possibility of extending the validity range of this formula.

3. HTCS WITH ANOMALOUS HEAT CONDUCTION

Now, let the plasma conductivity be given by formula (21) and the heat flux by

$$C_\parallel = \frac{n(k_BT)^{3/2}}{M^{1/2}}\xi b; \tag{32}$$

i.e., we took into account the fact that $f(\theta) = 1$ at $\theta \gg 1$ [see Eqs. (15) and (16)]. In this case, Eq. (9) takes the form

$$\frac{B_0^2}{4\pi}vb = \frac{1}{2}(MnV^2 + 5nk_BT)V\xi b + \frac{n(k_BT)^{3/2}}{M^{1/2}}\xi b. \tag{33}$$

The system of equations (5)–(8) and (33) is solved in the same way as previously. First, a, b, n, and V are determined from Eqs. (5)–(8), with the temperature T being considered as a parameter. Then, T is expressed in terms of n_0, E_0, h_0, and ξ using Eq. (33). To this end, we rewrite the terms on the right-hand side of this equation as

$$\frac{1}{2}(MnV^2 + 5nk_BT)V\xi b = \frac{7}{4}\frac{n_0}{n}\frac{B_0^2}{4\pi}vb \tag{34}$$

and

$$\frac{n(k_BT)^{3/2}}{M^{1/2}}\xi b = 2^{-3/2}\frac{n_0}{n}\frac{B_0^2}{4\pi}vb. \tag{35}$$

From Eq. (33), we now obtain the ratio

$$\frac{n}{n_0} = \frac{7}{4} + 2^{-3/2} \approx 2.1. \tag{36}$$

Hence, using Eq. (24), we determine the current-sheet temperature

$$T = \frac{1}{4[(7/4) + 2^{-3/2}]^{3/2}}\pi^{-1/2}k_B^{-1}M^{1/2}c[n_0^{-1/2}E_0\xi^{-1}]. \tag{37}$$

Thus, in the new HTCS model with anomalous heat flux, the quantities describing the current sheet (n, T, a, b, and V) are given by formulas (36), (37), (22), (23), and (25). Their estimates obtained for the same input data as those in Table 1 are listed in Table 3.

A comparison of Tables 2 and 3 shows that replacing the saturated heat flux by the anomalous one causes $C_\parallel$ to decrease by a factor of 2 or 3, which changes the result only slightly. The sheet becomes hotter and more rarefied, and its thickness and width slightly increase. The factor of changes does not exceed 4. Consequently, the choice of heat flux (saturated or anomalous) is not

Table 2. New model for a HTCS with saturated heat flux

Set of input parameters (see Table 1)	1	2	3	4
Computed quantities:				
T, K	1.0×10^7	4.0×10^6	7.0×10^7	7.0×10^7
n, cm^{-3}	5.5×10^{10}	5.5×10^{10}	5.5×10^{10}	5.5×10^{10}
a, cm	20	20	20	20
b, cm	2.4×10^7	2.3×10^8	2.4×10^8	7.7×10^8
V, cm/s	4.1×10^7	2.5×10^7	1.1×10^8	1.1×10^8
σ, s^{-1}	1.6×10^{13}	2.5×10^{12}	6.0×10^{12}	6.0×10^{11}
E_0/E_{cr}	1.4×10^3	2.3×10^3	6.3×10^4	6.3×10^5
$C_{\parallel}$, erg/(cm s)	5.8×10^{14}	1.3×10^{16}	1.0×10^{17}	3.1×10^{18}
P/l, erg/(cm s)	3.4×10^{15}	7.9×10^{16}	6.1×10^{17}	2.0×10^{19}

Table 3. New model for a HTCS with anomalous heat conduction

Set of input parameters (see Table 1)	1	2	3	4
Computed quantities:				
T, K	4.3×10^7	1.7×10^7	3.0×10^8	3.0×10^8
n, cm^{-3}	2.1×10^{10}	2.1×10^{10}	2.1×10^{10}	2.1×10^{10}
a, cm	32	32	32	32
b, cm	3.1×10^7	2.9×10^8	3.1×10^8	9.8×10^8
V, cm/s	8.4×10^7	5.3×10^7	2.2×10^8	2.2×10^8
σ, s^{-1}	1.2×10^{13}	2.0×10^{12}	4.7×10^{12}	4.7×10^{11}
E_0/E_{cr}	1.5×10^4	2.4×10^4	6.5×10^5	6.5×10^6
$C_{\parallel}$, erg/(cm s)	2.3×10^{14}	5.4×10^{15}	4.2×10^{16}	1.3×10^{18}
P/l, erg/(cm s)	5.5×10^{15}	1.3×10^{17}	1.0×10^{18}	3.2×10^{19}

critical in a rough comparison of the local models for a reconnecting current sheet. However, the choice of heat transport regime in a "superhot" (T > 30–40 MK) plasma may prove to be of importance in interpreting the hard X-ray flux from solar flares (see, e.g., Somov and Kosugi, 1997; Somov *et al.* 1998).

In conclusion, note that the power of energy release per unit length in the current sheet, depending on conditions, varies over a wide range: from ~10^{15} to ~10^{19} erg cm^{-1} s^{-1}; i.e., we obtain the power up to 10^{29} erg s^{-1} for a HTCS with a characteristic length of ~10^{10} cm, which is enough to account for flares, coronal transients, and coronal mass ejections (Somov 1992).

REFERENCES

1. L. G. Bagala, C. H. Mandrini, M. G. Rovira, *et al.*, Sol. Phys. **161**, 103 (1995).
2. H. de Kluiver, N. F. Perepelkin, and A. Hirose, Phys. Rep. **199** (6), 281 (1991).
3. P. Demoulin, L. van Driel-Gestelyi, B. Schmieder, *et al.*, Astron. Astrophys. **271**, 292 (1993).
4. V. S. Gorbachev and B. V. Somov, Astron. Zh. **66**, 105 (1989) [Sov. Astron. **33**, 57 (1989)].
5. V. S. Gorbachev and B. V. Somov, Adv. Space Res. **10** (9), 105 (1990).
6. V. S. Imshennik and S. I. Syrovatskiĭ, Zh. Éksp. Teor. Fiz. **52**, 990 (1967) [Sov. Phys. JETP **25**, 656 (1967)].
7. T. Kosugi and B. V. Somov, in *Observational Plasma Astrophysics: Five Years of Yohkoh and Beyond*, Ed. by T. Watanabe, T. Kosugi, and A. Sterling (Kluwer, Dordrecht, 1998), p. 297.
8. D. W. Longcope and A. V. R. Silva, Sol. Phys. **179**, 349 (1998).
9. Y.-J. Moon, H. S. Yun, S. W. Lee, *et al.*, Sol. Phys. **184**, 323 (1999).
10. E. N. Parker, Astrophys. J., Suppl. Ser. **8**, 177 (1963).
11. H. E. Petschek, in *Proceedings of the AAS-NASA Symposium on the Physics of Solar Flares*, Ed. by W. N. Hess (Washington, 1964), NASA SP-50, p. 425.
12. A. A. Pevtsov and D. W. Longcope, Astrophys. J. **508**, 908 (1998).
13. A. I. Podgorny and I. M. Podgorny, Sol. Phys. **182**, 159 (1998).
14. B. V. Somov, *Physical Processes in Solar Flares* (Kluwer, Dordrecht, 1992).

15. B. V. Somov, *Fundamentals of Cosmic Electrodynamics* (Kluwer, Dordrecht, 1994).

16. B. V. Somov and T. Kosugi, Astrophys. J. **485**, 859 (1997).

17. B. V. Somov, V. S. Titov, and A. I. Verneta, Itogi Nauki Tekh., Ser. Astron. **34**, 136 (1987).

18. B. V. Somov, T. Kosugi, and T. Sakao, Astrophys. J. **497**, 943 (1998).

19. B. V. Somov, E. Yu. Merenkova, T. Kosugi, *et al.*, in *Proceedings of the 9th European Meeting on Solar Physics on Magnetic Fields and Solar Processes* (ESA, Nordwijk, 1999), ESA SP-448, Vol. 2, p. 883.

20. P. A. Sweet, Nuovo Cimento Suppl. **8** (X), 188 (1958).

21. S. I. Syrovatskiĭ, Astron. Zh. **39**, 987 (1962) [Sov. Astron. **6**, 768 (1962)].

22. S. I. Syrovatskiĭ, Astron. Zh. **43**, 340 (1966) [Sov. Astron. **10**, 270 (1966)].

23. S. I. Syrovatskiĭ, Tr. Fiz. Inst. Akad. Nauk SSSR **74**, 3 (1974).

Translated by A. Oreshina